Hybrid simulation for large-scale MMC-MTDC embedded power systems

Final Project Report

S-83G

Power Systems Engineering Research Center
Empowering Minds to Engineer
the Future Electric Energy System

Hybrid simulation for large-scale MMC-MTDC embedded power systems

Final Project Report

Project Team
Jiangchao Qin, Project Leader
Arizona State University

Graduate Students
Denise Athaide
Lei Zhang
Yuntao Zou
Arizona State University

PSERC Publication 21-01
January 2021

For information about this project, contact:

Jiangchao Qin
Arizona State University
School of Electrical, Computer, and Energy Engineering
PO Box 875706
Temp, AZ 85287-5706
Fax: 480-727-2052
Email: jqin@asu.edu

Power Systems Engineering Research Center

The Power Systems Engineering Research Center (PSERC) is a multi-university Center conducting research on challenges facing the electric power industry and educating the next generation of power engineers. More information about PSERC can be found at the Center's website: http://www.pserc.org.

For additional information, contact:

Power Systems Engineering Research Center
Arizona State University
527 Engineering Research Center
Tempe, Arizona 85287-5706
Phone: 480-965-1643
Fax: 480-727-2052

Notice Concerning Copyright Material

Acknowledgements

This is the final report for the Power Systems Engineering Research Center (PSERC) research project titled "Hybrid simulation for large-scale MMC-MTDC embedded power systems" (project S-83G). We express our appreciation for the support provided by PSERC's industry members. In particular, this work was support by GEIRINA and we wish to thank the industry advisors for this project: Zhiwei Wang, Di Shi, and Xi Chen.

Executive Summary

Modular multilevel converter (MMC) has become the most attractive converter topology for voltage-sourced converter high-voltage direct current (VSC-HVDC) transmission systems due to its salient features, e.g., modularity, scalability, inherent redundancy, and high efficiency. MMC based multi-terminal high voltage dc (MTDC) system is a promising technology in grid integration of various renewable energy resources, interconnection of asynchronous ac grids, long-distance power transmission, and enhancement of ac networks. To analyze and understand the dynamics of large-scale MMC-MTDC hybrid ac and dc systems, simulation-based study is commonly used. However, high-efficient simulation for such complex systems is difficult to be achieved due to large amount of mixed power electronic switches, electromagnetics devices, and electromechanical components. In this report, the primary goal is to investigate techniques for highly efficient modeling and simulation of MMC-MTDC systems. The report is presented in three parts.

Part I: A general equivalent circuit model for MMCs and simulation performance analysis

Modelling and simulation of a high voltage-level modular multilevel converter (MMC) is challenging due to large amount of semiconductor switches, various submodule (SM) circuits, and different operating conditions. Several equivalent models have been proposed for modelling and simulation in system level, which did not consider an industrial or digital controller. To accelerate MMC simulation, a highly efficient model is needed with considering control parameters/strategies and accurate dynamics of voltage/current. In Part I, a general equivalent circuit model (ECM) is developed for large-scale system simulation and MMC station design. The proposed ECM considers the MMCs based on various SM circuits under different operating conditions. It can generate bipolar arm voltage and simulate static compensator under dc fault condition. Based on the proposed ECM, the influences of simulation time step on simulation accuracy/efficiency are investigated by considering the sample period and voltage balancing strategies. This research is conducted based on an MMC-HVDC system in the PSCAD/ EMTDC software platform. The study results demonstrate the effectiveness of the proposed ECM and show the relationship between simulation accuracy/efficiency and control/simulation parameters for determining simulation time step. Based on study results, it is found that the computational efficiency of proposed model is not significantly affected by the complexity of SM circuit.

Part II: Modeling of MMC-MTDC Systems

With the increasing demand on renewable energy integration and bulk power transmission, the MMC-MTDC system with droop control and intricate dc network develops into a complicated nonlinear system. Modeling of such complex system is challenging due to multiple coupled controllers and complicated dc networks. In particular, modeling of dc network in the previous research is insufficient, which only considers the simple topology of dc network, e.g., common-bus, three-, or four-terminal systems. In Part II, a systematic method for modeling the MMC-MTDC system will be developed with considering the general topology of dc network, the model of transmission lines or cables, dq control, and droop control. The edge-node incidence matrix is introduced for modeling the dc network with arbitrary topology. The transmission lines or cables

are modeled as two-port networks without knowing their inner structures. In addition, a uniform matrix structure is developed for easily scaling the model of the MMC-MTDC system when the number of converter stations and controllers changes. To verify the developed model, two study systems, i.e., a 4-terminal and 14-terminal MMC-MTDC systems, are employed. A comparison of dynamic responses between the calculations of the developed nonlinear state-space models in MATLAB and the EMT simulations in PSCAD/EMTDC is conducted, which demonstrates the accuracy and correctness of the developed model.

Part III: MATLAB/Simulink-Based Electromagnetic Transient-Transient Stability Hybrid Simulation

The dynamics of power electronic converters are best represented accurately by electromagnetic transient (EMT) simulation tools. However, in these programs, the simulation time step size is usually very small and the presence of frequencies other than the fundamental frequency, such as harmonics and switching frequencies, necessitate the use of instantaneous, three phase quantities. Therefore, they require large computation times. On the other hand, transient stability (TS) simulation programs generally use comparatively large integration time steps. It can be assumed that the fundamental power frequency is maintained throughout the system under most conditions and phasors of the electrical quantities are therefore sufficient to model these systems. They have a much smaller computation time, but are not adequate to represent the dynamic response under many conditions. Therefore, to study power electronics based power systems, hybrid simulation methods and tools have been proposed and developed which combine two different software platforms to run the EMT and TS simulations separately. However, there are complexities, inconsistencies and inaccuracies involved when interfacing two different simulation platforms. Matlab/Simulink has the capacity to run EMT as well as phasor domain simulations. Thus, it serves as a suitable platform to integrate both simulation domains to build a hybrid simulation. In Part III, a hybrid EMT-TS simulation method is developed in the MTALBA/Simulink environment for modeling and simulation of power electronics based power systems. The purpose of selecting MATLAB/Simulink over individual software for EMT and TS simulation is to deliver a more general simulation environment, to test the hybrid simulation algorithm and procedure, particularly the interface between the EMT and TS simulations. It also ensures improved and less complex interfacing, communication and compatibility between the EMT and TS simulation models.

Project Publications:

[1] L. Zhang, J. Qin, D. Shi, and Z. Wang, "Improved equivalent circuit model of MMC and influence analysis of simulation time step, " *IET Power Electronics*, vol. 13, no. 11, pp. 2212-2221, 2020.

[2] D. Athaide, J. Qin and Y. Zou, "MATLAB/Simulink-Based Electromagnetic Transient-Transient Stability Hybrid Simulation for Electric Power Systems with Converter Interfaced Generation," 2019 *IEEE Texas Power and Energy Conference* (TPEC), College Station, TX, USA, 2019, pp. 1-6.

Student Theses:

[1] Lei Zhang. *Modeling, Control, and Design of Modular Multilevel Converters for High Power Applications*. PhD thesis, Arizona State University, December 2020.

[2] Yuntao Zou. *Modeling, Control and Stability Analysis of MMC-based MTDC System*. PhD thesis, Arizona State University, expected in May 2021.

[3] Denise Athaide. *Electromagnetic Transient - Transient Stability Hybrid Simulation for Electric Power Systems with Converter Interfaced Generation.* Master's thesis, Arizona State University, November 2018.

Part I

A general equivalent circuit model for MMCs and simulation performance analysis

Jiangchao Qin
Lei Zhang, Graduate Student

Arizona State University

For information about this project, contact:

Jiangchao Qin
Arizona State University
School of Electrical, Computer, and Energy Engineering
PO Box 875706
Temp, AZ 85287-5706
Fax: 480-727-2052
Email: jqin@asu.edu

Power Systems Engineering Research Center

The Power Systems Engineering Research Center (PSERC) is a multi-university Center conducting research on challenges facing the electric power industry and educating the next generation of power engineers. More information about PSERC can be found at the Center's website: http://www.pserc.org.

For additional information, contact:

Power Systems Engineering Research Center
Arizona State University
527 Engineering Research Center
Tempe, Arizona 85287-5706
Phone: 480-965-1643
Fax: 480-727-2052

Notice Concerning Copyright Material

Table of Contents

List of Figures

List of Tables

1. Introduction

1.1 Background

Due to modularity and scalability, modular multilevel converter (MMC) has become the most attractive converter topology for medium/high-voltage applications, especially for voltage-sourced converter high-voltage direct current transmission systems (VSC-HVDC) [1]. For large-scale MMC-embedded power systems, it is required to investigate dynamic performance, fault, protection, and stability [2–4]. Modelling of the MMC is one of the main challenges associated with the study of the large-scale MMC-based power systems. On the other hand, for the purpose of design of a practical MMC station and its controller, highly efficient model is also needed with considering control parameters/strategies and accurate dynamics of arm voltage/current, dc current, and capacitor voltage.

1.2 Overview of the Problem

The detailed switching model (DSM) of the MMC for electromagnetic transient (EMT) simulation is time consuming due to large number of semiconductor switches. To address this challenge, several MMC models have been developed to accelerate the EMT simulation, including average-value models and equivalent circuit models (ECMs) [3, 5–19]. These models are briefly summarized as follows:

- SM configuration: In [5, 6, 8, 10, 15, 16, 19], the ECMs only considered the half-bridge SM, which are not capable of blocking fault current under dc-fault conditions. In [12], the ECM is developed based on hardware-in-loop platform, which considers the full-bridge (FB) SM without verifying fault-blocking operations. In [9, 13], the real-time ECMs are implemented by digital controllers, which only considers the operating behaviors of the HB-MMC. In [14, 18], although the ECMs consider the fault-blocking SMs, the arm circuits are not optimal.
- Operating mode: In [3, 7], although the ECMs consider the operating behavior of the FB SM, they do not consider fault-STATCOM (static compensator) operating conditions of the MMCs based on fault-blocking SMs.

Therefore, there is still lack of comprehensive considerations of various SM circuits and different operating conditions. On the other hand, in [11, 20, 21], the simulation time step is assumed to be equal to the sampling time step, which does not consider practical issues of an industrial or digital controller, i.e., DSP and/or FPGA. In the practical MMC-based systems, the practical sampling period (or control period) of an industrial controller depends on system requirements and limitations. When using the practical sampling period in modelling and simulation, the simulation time step may not be equal to the sampling period. When fixing the sampling period, the increased simulation time step will lead to additional error. To accurately simulate these MMC-based systems with considering the industrial controllers, the simulation time step must be properly selected based on required simulation accuracy and computational efficiency. Moreover, the impacts of the simulation time step on voltage balancing strategies (e.g. sorting algorithms) have never been investigated before.

In this paper, an improved equivalent arm circuit of the MMC is proposed for modelling and simulation of the MMCs based on various configurations and different operations. The developed MMC models are scalable for system and device level studies with integrating practical control algorithms. Moreover, the simulation time step is comprehensively investigated by considering the sampling period of the industrial controller, capacitor voltage balancing strategies, errors of current and voltage level, and computational efficiency. The impacts and determination of the simulation time step on simulation accuracy and efficiency with considering sampling period and balancing period will be analyzed and discussed. The study results are applicable to the other existing ECMs.

1.3 Report Organization

This report is structured as follows:

- Chapter 2 analyzes the basic operations of the MMCs based on various SM circuits and proposes the improved ECM.
- In Chapter 3, the fault-STATCOM operating mode is analyzed.
- Chapter 4 investigates the influence of simulation parameters on simulation accuracy and efficiency.
- Chapter 5 shows the study results.
- Chapter 6 concludes this report.

2. Configurations and Operational Principles of the Proposed ECM

The proposed arm circuit and various SM circuit topologies are shown in Figure 2.1 and Figure 2.2, respectively. The operational principles of various SM circuits have been presented in [22]. Among the fault- blocking SM circuits, the unipolar full-bridge (UFB), clamp-double (CD), and three-level cross-connected (3LCC or 3LX) SMs provide unipolar SM voltage; while the FB and five-level cross-connected (5LCC or 5LX) SMs can generate bipolar SM voltages. The MMC's operating conditions mainly include precharging/startup process, normal operating condition, and fault condition. Under dc fault condition, the MMC based on the HB SMs (HB-MMC) cannot block the fault currents fed from the ac grid. The fault-blocking SMs can block the fault currents. In addition, the MMC based on the fault-blocking SMs can work as a STATCOM under dc fault conditions [23, 24].

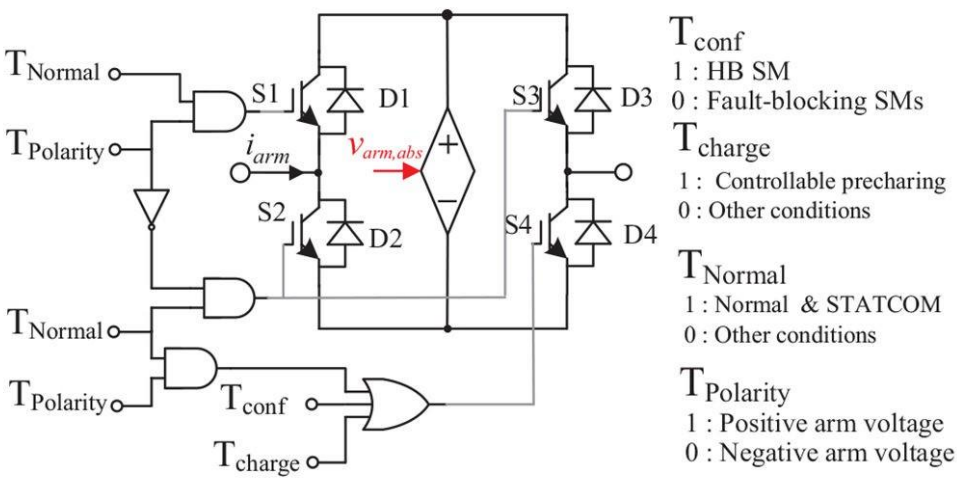

Figure 2.1 Proposed equivalent circuit of an arm.

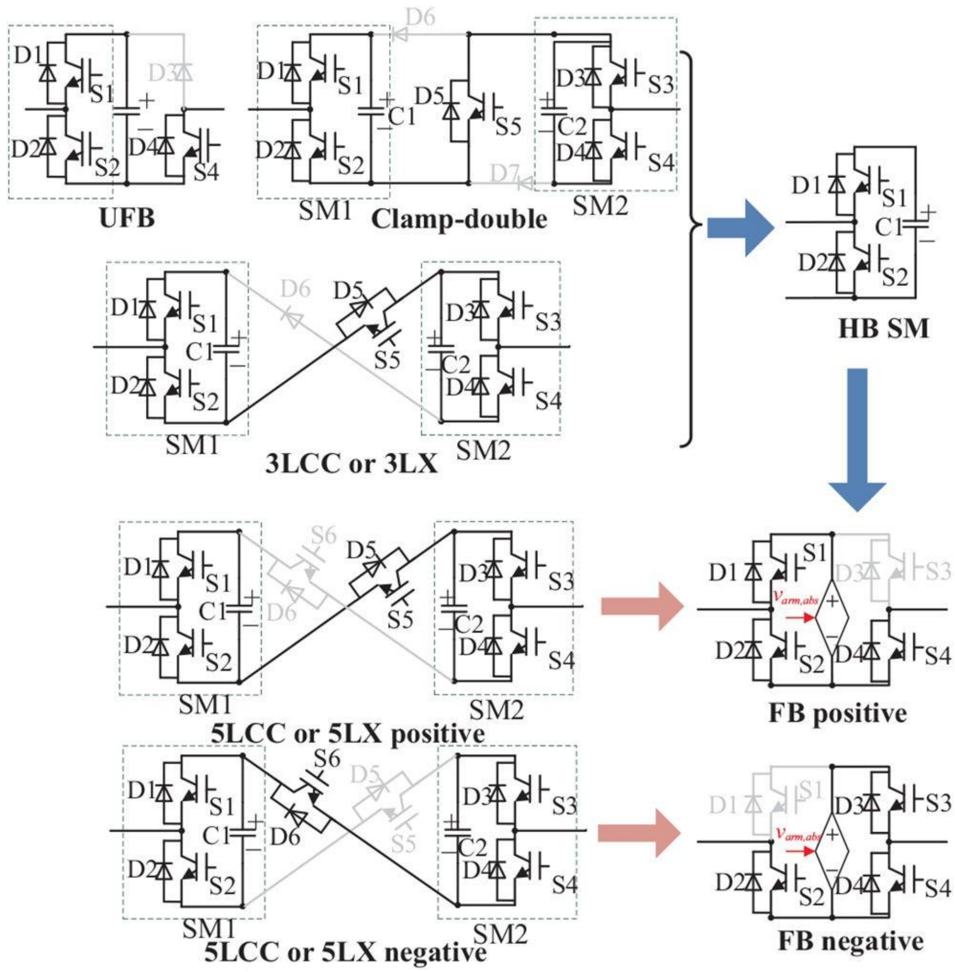

Figure 2.2 Various SM circuit topologies with fault-blocking capability.

2.1 Operational Principles of the Proposed Equivalent Arm Circuit

2.1.1 Proposed Improved Equivalent Arm Circuit

Under normal operating condition, the SM configurations of Fig. 2.2 can be equivalent to a single HB SM or combination of two individual HB SMs. The UFB SM has the same behavior as the HB SM, while the CD SM and 3LX SM consist of two series-connected HB SMs. The FB SM and 5LX SM have similar behaviors, which can generate bipolar voltages. Under blocked condition, the fault-blocking SMs have the same behavior as the FB SM. Consequently, the FB circuit can be assumed as a general equivalent circuit, as shown in Fig. 2.1.

2.1.2 Switching States of the Proposed Equivalent Arm Circuit

The switching states of the proposed arm circuit of Fig. 1 depend on SM configurations and operating conditions, as listed in Table 2.1Table 2.1.

Table 2.1 Switching States of the Proposed Equivalent Arm

SM configuration	Operating conditions		Arm voltage polarity	S1	S2	S3	S4
HB T_{conf}=1	Precharging & DC fault			0	0	0	1
	Normal T_{normal}=1		positive	1	0	0	1
Trans-former	Precharging T_{normal}=0	Uncontrollable		0	0	0	0
		Controllable		0	0	0	1
	Normal & Fault-STATCOM T_{normal}=1		positive	1	0	0	1
			negative	0	1	1	0
	Fault-blocking T_{normal}=0			0	0	0	0

The operating conditions include precharging, normal, fault-blocking, and fault-STATCOM conditions. For the HB-MMC, under normal operating condition, the S1 and S4 of Fig. 1 are turned on, i.e., T_{conf} = 1, T_{charge} = 0, T_{normal} = 1, and $T_{polarity}$ = 1. Under other conditions, only S4 is turned on, i.e., T_{conf} = 1, T_{normal} = 0, and $T_{polarity}$ = 1. For the MMCs based on the fault-blocking SMs, the details are described as follows:

• Precharging condition: In [25, 26], the startup process can be divided into uncontrollable precharging stage and controllable precharging stage. Under uncontrollable precharging condition, T_{normal} = 0. Under controllable precharging stage, the MMCs based on various SM circuits operate as the HB-MMC. Thus, the S4 should be turned on, and T_{charge} = 1.
• Normal and fault-STATCOM conditions: T_{normal} = 1 and T_{charge} = 0. The switching states of Fig. 1 are then determined by the arm voltage polarity, as listed in Table 2.1.
• Blocked conditions: The blocked conditions include the uncontrollable precharging condition and dc fault-blocking condition. Under these conditions, T_{normal} and T_{charge} are set to be 0.

After determining T_{conf}, T_{normal}, and T_{charge}, the switching states of Fig. 1 can be determined by the arm voltage polarity. For the MMCs based on the fault-blocking SMs, under normal and fault-STATCOM conditions, the arm voltage can be positive and negative. To generate the positive voltage, the S1 and S4 are turned on, and $T_{polarity}$ = 1. For the negative voltage, the S2 and S3 are turned on, and $T_{polarity}$ = 0.

2.2 Developed Detailed ECM

2.2.1 Overview of the Developed Detailed ECM

Based on the proposed equivalent arm circuit, the detailed MMC model can be developed with considering an industrial controller, as shown in Fig. 2.3. When modelling the MMCs based on the proposed ECM, the simulation time step is set for the whole system. The control system can be divided into two parts: (i) the control strategy and modulation are executed every sampling (or control) period; (ii) the capacitor voltage balancing algorithm (e.g. sorting) is executed every sorting period. The detailed steps for simulation setup are shown as follows:

• Step 1: Determination of simulation parameters: Firstly, the simulation parameters and MMC configurations should be determined. Based on these parameters, the switching states of Fig. 2.1 can be determined according to Section 2.1.

• Step 2: Execution of control algorithms: In the detailed ECM, the controller performs the converter-level control algorithms, including capacitor voltage balancing, active and reactive power control, and circulating current control. Then, it generates the gating signals to switch on/off the associated SMs.

• Step 3: Capacitor current calculation: The gating signals are used to derive the capacitor currents based on the arm current.

• Step 4: Capacitor voltage calculation: The capacitor voltages are derived based on the capacitor current and the differential equations.

• Step 5: Arm voltage calculation: The arm voltage (v_{arm}) is derived based on the gating signals and the capacitor voltages. The absolute value of arm voltage ($|v_{arm}|$) is the input of the controlled voltage source, as shown in Fig. 2.3.

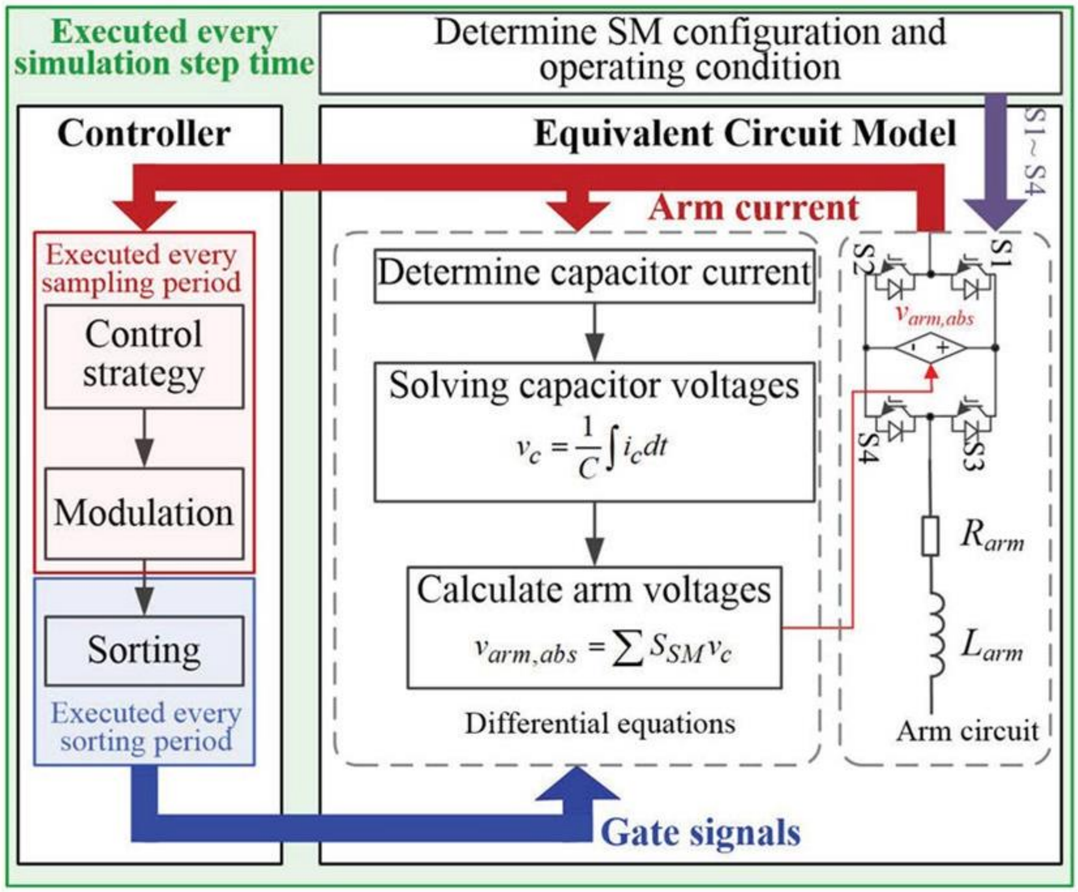

Figure 2.3 MMC model with its controller based on the proposed equivalent.

2.2.2 Capacitor Current and Voltage

The dynamics of each capacitor voltage is described by

$$i_c = C\frac{\mathrm{d}v_c}{\mathrm{d}t}, \tag{2.1}$$

where v_c represents the capacitor voltage and i_c refers to the capacitor current.
The capacitor voltage at time t_k can be derived from (2.1), which is given by

$$v_c(t_k) = v_c(t_{k-1}) + \frac{1}{C}\int_{t_{k-1}}^{t_k} i_c(\tau)d\tau, \tag{2.2}$$

The capacitor voltage can be solved by numerical methods. In this paper, the Simpson quadrature method is employed. To solve for the capacitor voltage, the capacitor current is required, which depends on the SM circuit, SM switching state (inserted or bypassed), and arm current.

For the HB SM, the capacitor current can be derived as follows:

- Blocked condition: When all switches of the HB SM are turned off, the capacitor current is determined by the direction of the arm current and given by

$$i_c = \begin{cases} i_{\mathrm{arm}}, & i_{\mathrm{arm}} > 0, \\ 0, & i_{\mathrm{arm}} < 0, \end{cases} \tag{2.3}$$

- Normal condition: i_c depends on insertion and bypass of the SM, and can be expressed as

$$i_c = S_{HB} i_{arm}, \tag{2.4}$$

where S_{SM} is the switching function of the HB SM and defined by

$$S_{HB} = \begin{cases} 1, & \text{inserted}, \\ 0, & \text{bypassed}, \end{cases} \tag{2.5}$$

For the fault-blocking SMs, under normal operating conditions, they behave like the HB SM and i_c can be determined by (2.4), in which S_{HB} is their corresponding switching state. Under fault operating conditions, for the UFB, FB, 3LX, and 5LX SMs, when all switches are turned off, either positive or negative arm currents flow through the anti-parallel diodes to charge the capacitors, and $i_c = |i_{\mathrm{arm}}|$.

For the CD SM, under fault conditions, when the arm current is positive, two HB SMs in the CD SM are connected in series. When the arm current is negative, two HB SMs are connected in parallel. Therefore, when the CD SM is blocked, the capacitor currents can be calculated by

$$i_{c,1} = i_{c,2} = \begin{cases} |i_{\text{arm}}|, & i_{\text{arm}} > 0, \\ 0.5|i_{\text{arm}}|, & i_{\text{arm}} < 0, \end{cases} \tag{2.6}$$

where $i_{c,1}$ and $i_{c,2}$ are the currents of two capacitors in the CD SM, respectively.

2.2.3 Arm Voltage

The voltage of the controllable voltage source varm, abs of Fig. 1 can be calculated based on the number of the inserted SM capacitors. The number of the inserted SM capacitors is determined by SM circuits and switching states, arm current direction, and operating conditions.

- Normal operating condition: The UFB, 3LX, and 5LX SMs are equivalent to a single HB SM or two series-connected HB SMs. Then, the arm voltage is generally expressed as (2.7). The FB SM can be assumed as two parallel-connected HB SMs. The arm voltage is expressed as (2.8). $v_{\text{arm,abs}}$ is the input to the controllable voltage source, as shown in Fig. 2.4.

$$v_{arm} = \sum S_{HBi} v_{ci}, \tag{2.7}$$

$$v_{arm} = \sum \left(S_{HBi1} - S_{HBi2}\right) v_{ci}, \tag{2.8}$$

Where S_{HBi1} regulates the HB SM consisting of S1 and S2, while S_{HBi2} regulates the HB SM consisting of S3 and S4.

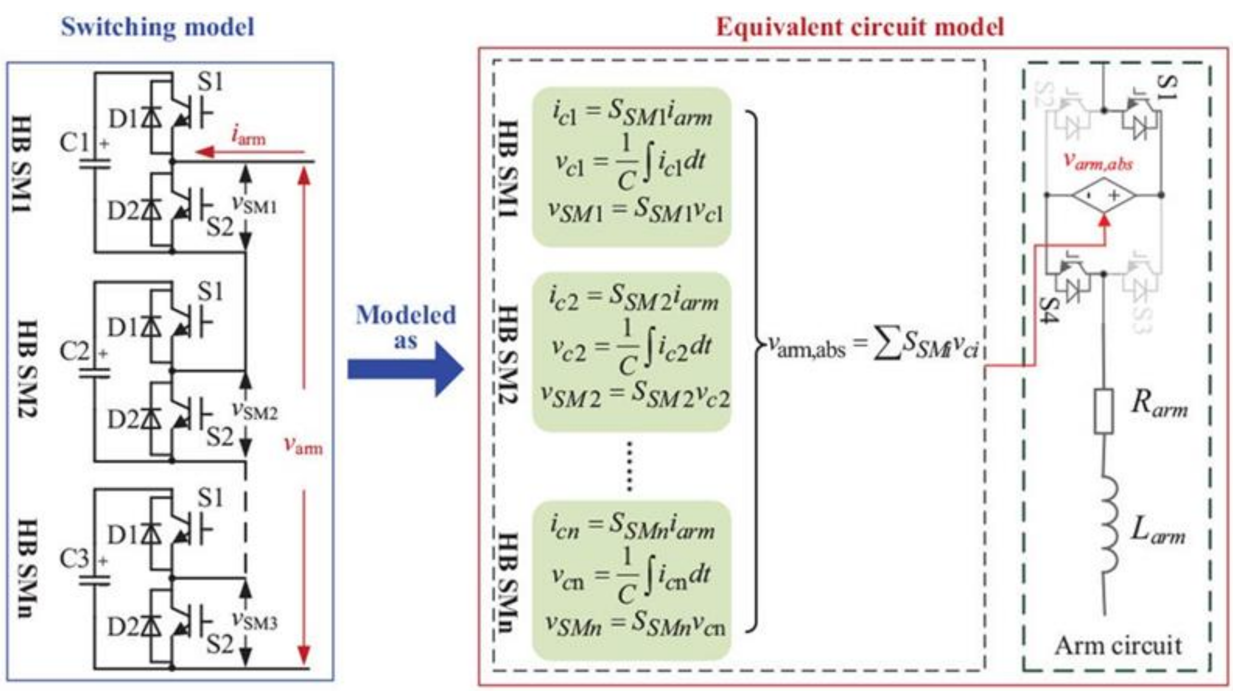

(a)

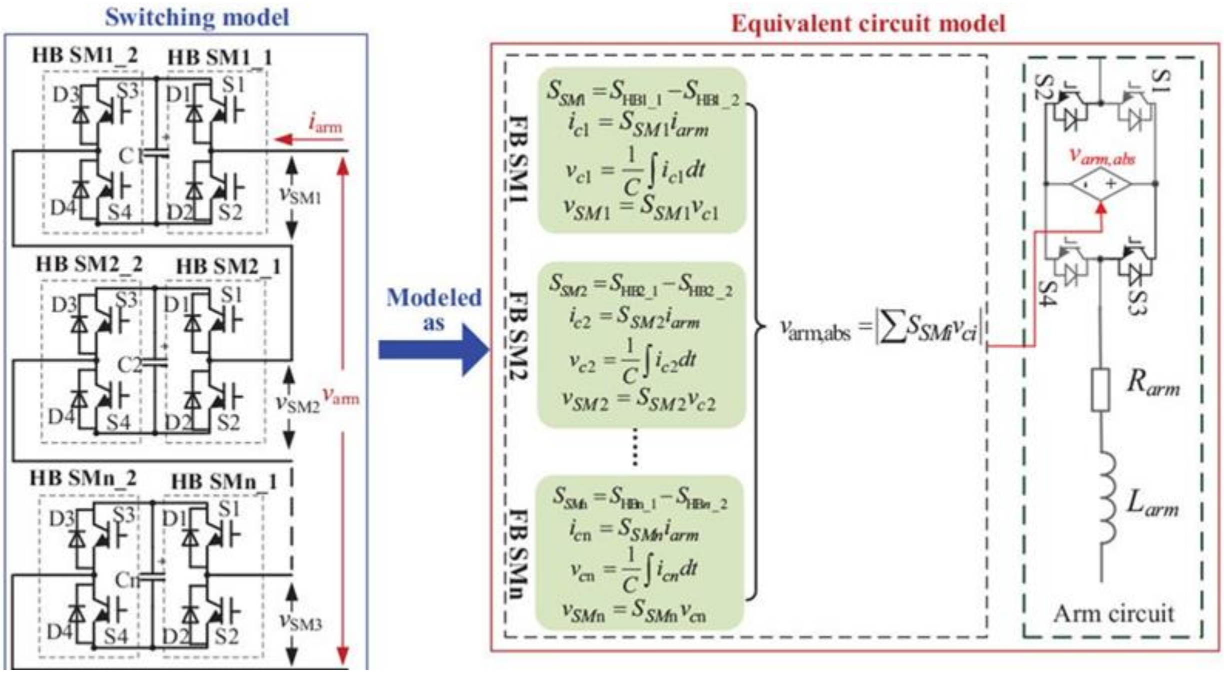

(b)

Figure 2.4 Schematic of (a) HB-MMC, and (b) FB-MMC under normal condition.

- Blocked conditions: For the HB-MMC, when the arm is positive, $v_{arm} = N_{inserted} v_c$, where $N_{inserted}$ is the number of capacitors in the blocked-state SMs per arm. Otherwise, the arm voltage is zero. For the fault-blocking MMCs, v_{arm} is the sum of the capacitor voltages in the blocked SMs regardless of the direction of the arm current, as shown in Fig. 2.5.

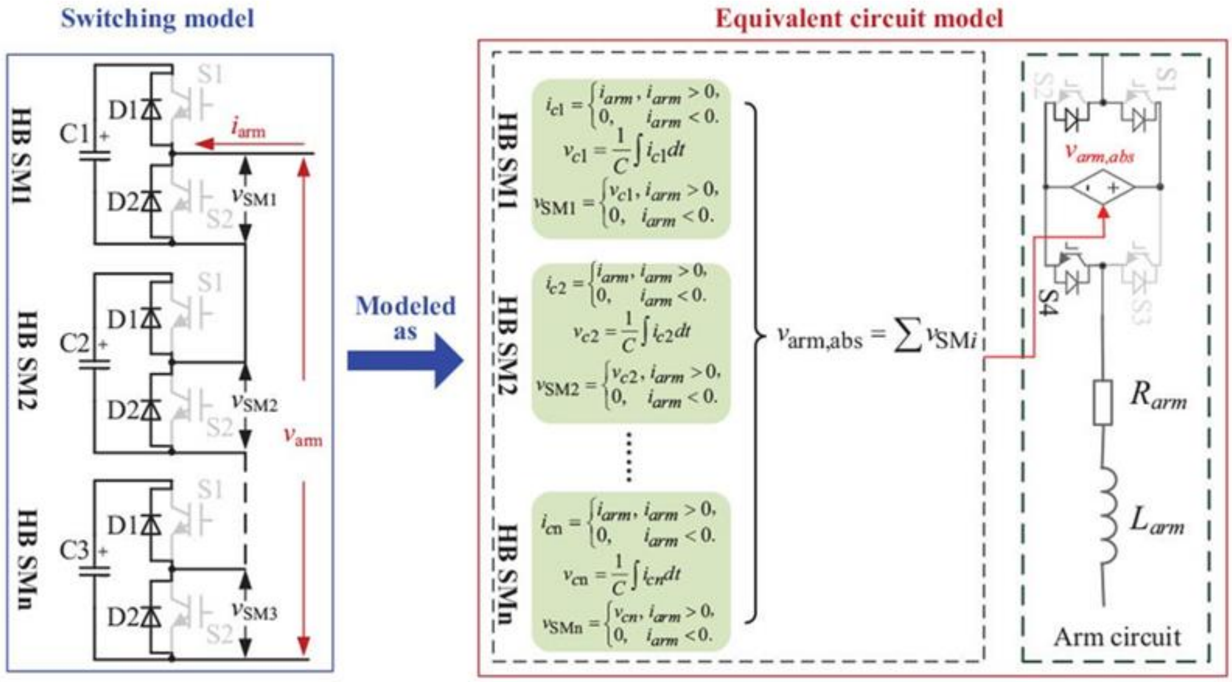

(a)

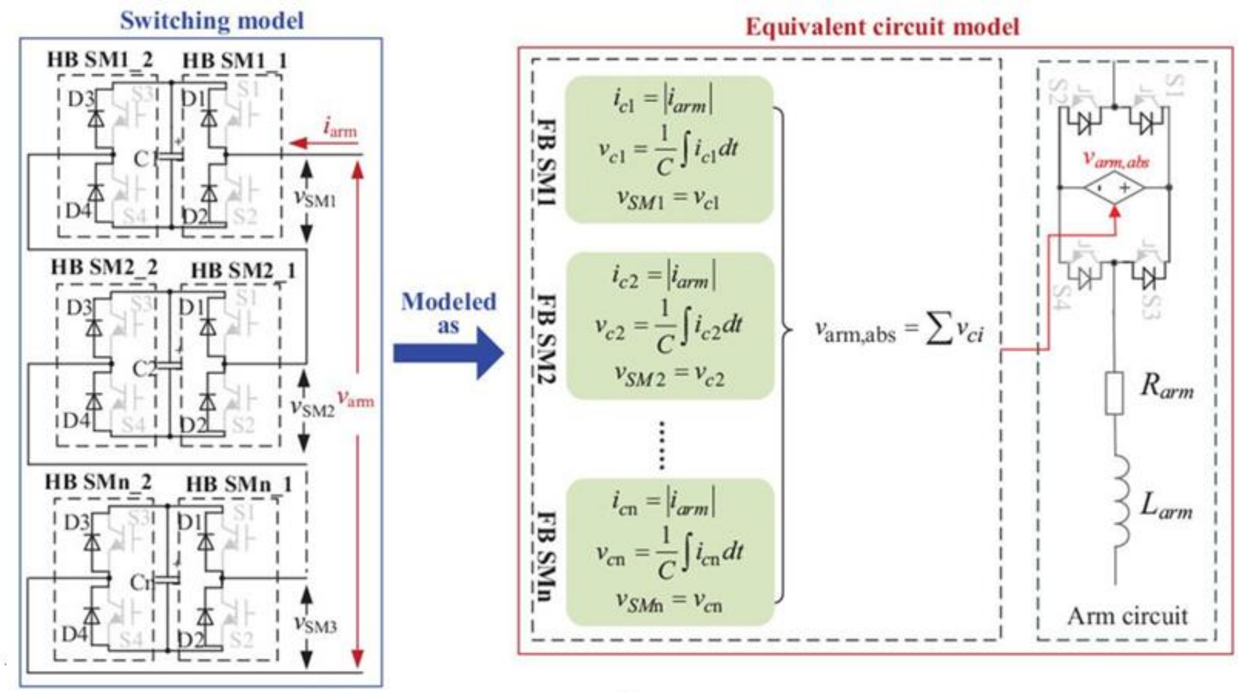

(b)

Figure 2.5 Schematic of (a) HB-MMC, and (b) FB-MMC under blocked condition.

2.3 Simplified ECM

To further improve the computational efficiency of the proposed ECM, the number of state variables (i.e. capacitor voltages) can be reduced. This simplified ECM assumes that all capacitor voltages are well balanced and only the average capacitor voltage of each arm is considered to calculate the arm voltage.

Under normal operating condition, as analyzed in [15], the average capacitor current is derived as

$$i_{c,avg} = \frac{1+d_{arm}}{2} i_{arm}, \tag{2.9}$$

where d_{arm} is the modulation reference, which is derived from grid current controller and circulating current controller. The average capacitor voltage of an arm can be derived by (2.2) and (2.9). The arm voltage is determined by the number of the inserted SM capacitors, which is given by

$$v_{arm} = N_{\text{insert}} v_{c,avg}, \tag{2.10}$$

where N_{insert} is the number of the inserted capacitors, and $v_{\text{c,avg}}$ is the average SM capacitor voltage of an arm.

Under uncontrollable precharging and dc fault conditions, the capacitor currents of various SMs are still governed by (2.3) and (2.6). The arm voltage is determined by the SM circuit and number of capacitors. Under controllable precharging condition, the average capacitor voltage is determined by the equivalent capacitance per arm, which depends on the SM circuits and the number of the inserted capacitors and has been analyzed in [25].

3. Fault-STATCOM Operating Mode

Under pole-to-pole dc fault condition, the MMC can provide reactive power to the ac grid when operating in the STATCOM mode. Based on fault-blocking SMs, the MMCs can produce bipolar arm voltages. Thus, the upper arms, the lower arms, or both lower and upper arms can perform STATCOM function similar to the cascaded H-bridge converter. The fault-STATCOM control strategy has been summarized in [23, 24]. Under fault-STATCOM condition, the equivalent circuit of the fault-blocking MMCs is shown in Fig. 3.1. The fundamental-frequency arm voltage is controlled to regulate the reactive power transfer. The reference of dc circulating current is set to be zero. The ac grid needs to compensate the power loss of MMC to maintain the capacitor voltages. The overall control is shown in Fig. 3.2. In this report, the proposed ECM is able to model and simulate the fault-STATCOM operations of the fault-blocking MMCs.

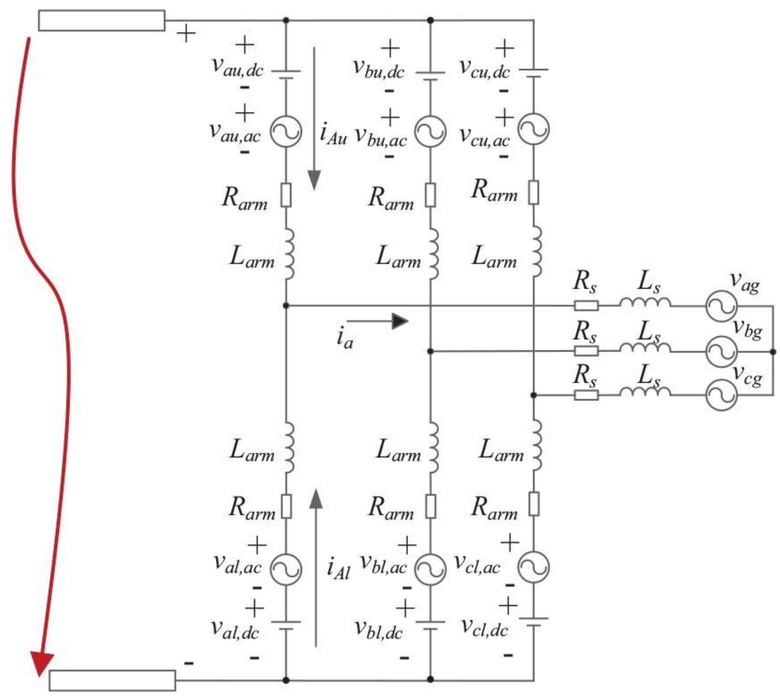

Figure 3.1 Equivalent circuit of fault-blocking MMC under fault-STATCOM condition.

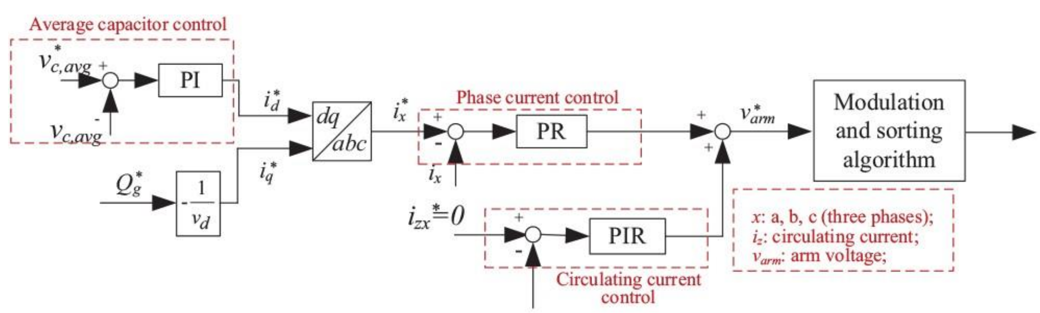

Figure 3.2 Block diagram of the control strategy for the fault-blocking MMCs under fault-STATCOM condition.

4. Influence Analysis of Simulation Parameters

The proposed ECM can be used to evaluate the dynamic performance of the MMC with considering its industrial controller. However, the improperly selected simulation time step may lead to additional errors and low computational efficiency during simulation. Thus, the simulation time step t_{step} should be properly determined based on the sampling period or control period t_{sample}, capacitor voltage balancing period t_{sort}, and simulation accuracy and efficiency.
A point-to-point FB-MMC-HVDC system is selected as the study system and the system parameters are listed in Table 4.1. Based on the DSM and proposed ECM technologies, the models of the MMC-HVDC system are built and compared in the PSCAD/ EMTDC program environment. The simulation time step and sampling period of the DSM are set as 10 μs.

Table 4.1 System Parameters of the MMC-HVDC System

Parameters	Nominal value
Rated power	100 MW
DC link voltage	110 kV
AC grid line-to-line voltage	60 kV RMS
Number of SMs per arm, N_{SM}	20
Arm inductance	5 mH
Capacitance per SM	1000 μF
Rated capacitor voltage per SM	5 kV
DC line inductance	1 mH
DC line resistance	1 Ω
DC line capacitance	100 μF

4.1 Influence of the Sampling Period

As shown in Fig. 4.1, the increased sampling period t_{sample} causes the increased time delay, loss of voltage level, and distortion in arm voltage, and, consequently, leads to increased harmonics in arm current and dc current. The maximum sampling period has been investigated in [11, 20, 21], which is determined by the modulation index and the total number of SMs per arm, as expressed in the following equation

$$t_{\text{sample}} = \frac{1}{\pi m f_0 N_{SM}}, \tag{4.1}$$

where m is the modulation index, f_0 is the fundamental frequency, and N_{SM} is the number of SMs per arm. When fixing the simulation time step at 10 μs, the modulated waveform is shown in Fig. 4.2. The increased sampling period leads to increased distortion.

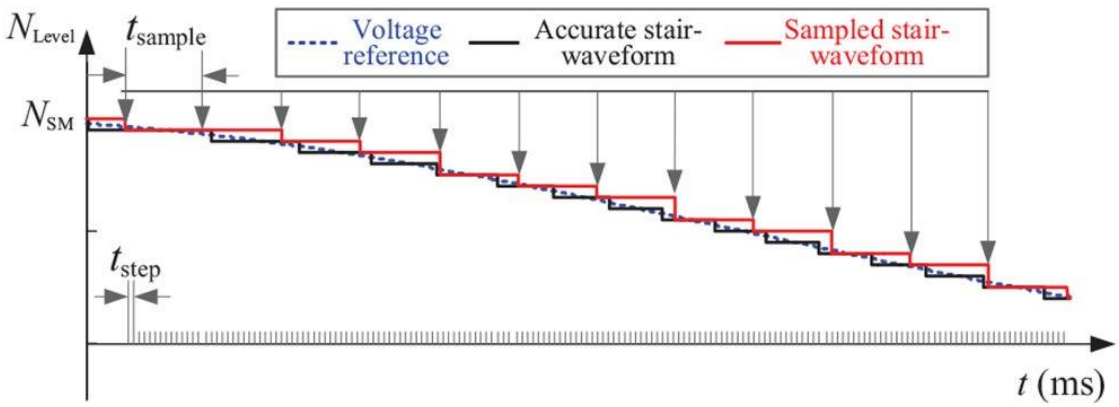

Figure 4.1 Voltage levels of the MMC with t_{sample} = 200 μs.

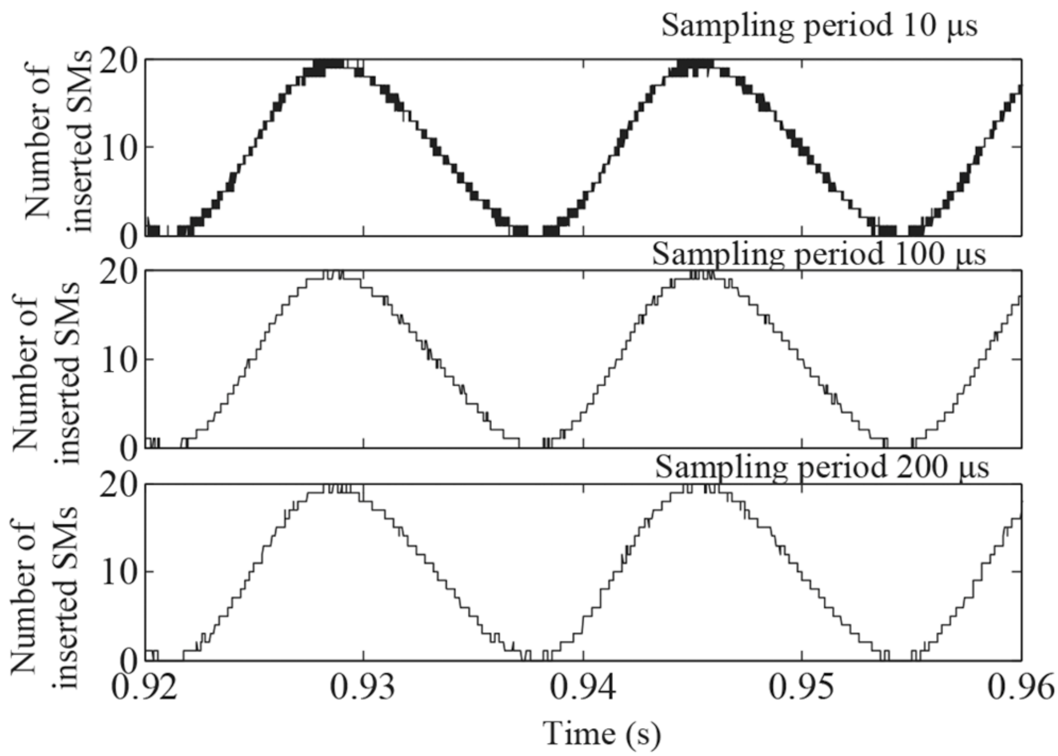

Figure 4.2 Modulated waveform when fixing the simulation time step at 10 μs.

4.2 Influence Analysis of the Simulation Time Step

In [11, 20, 21], the sampling period equals to the simulation time step, which may not be proper when considering an industrial controller. The sampling period or controller period depends on the practical system specifications and limitations. When using the sampling period of the industrial controller for modelling and simulation, the simulation time step is flexible to choose. When fixing the sampling period, the increased simulation time step will lead to additional distortion. To ensure the system operating properly, the influence of the simulation time step should be investigated. When fixing the sampling period, the simulation time step should be equal to or less than the sampling period, i.e.,

$$t_{\text{step}} \leq t_{\text{sample}}. \tag{4.2}$$

In this section, to investigate the influence of the simulation time step, t_{sample} is fixed at 100 μs.

4.2.1 Influence of t_{step} on Capacitor Voltage Balancing

The capacitor voltage balancing period t_{sort} will significantly affect the switching frequency of semiconductor devices and their power losses [27, 28]. To reduce power losses of the MMCs, the reduced switching-frequency balancing methods are preferred. Thus, the sorting period should be equal to or greater than the sampling period, i.e., [27–31]

$$t_{\text{sort}} \geq t_{\text{sample}}. \tag{4.3}$$

For the given sampling period, if properly increasing the simulation time step, the performance of capacitor voltage balancing is not significantly affected, as shown in Fig. 4.3.

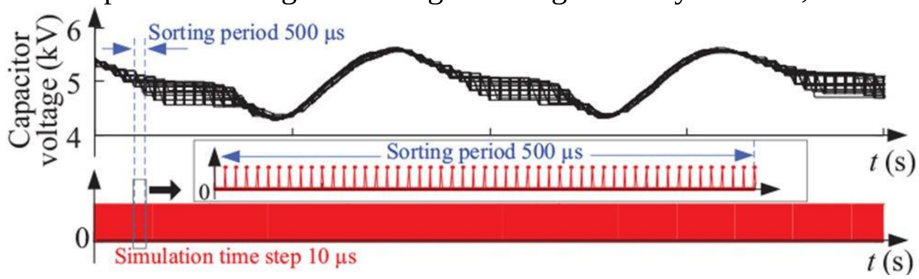

(a)

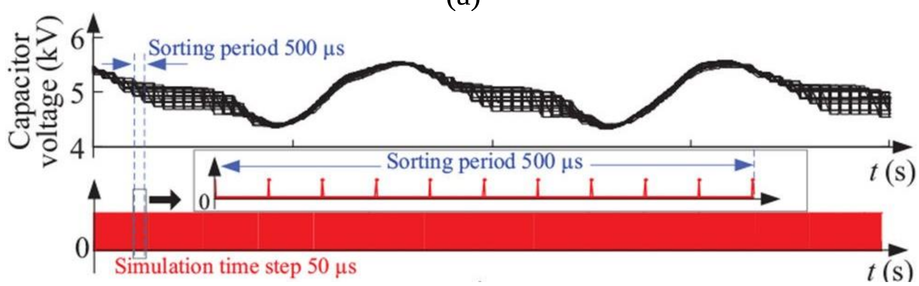

(b)

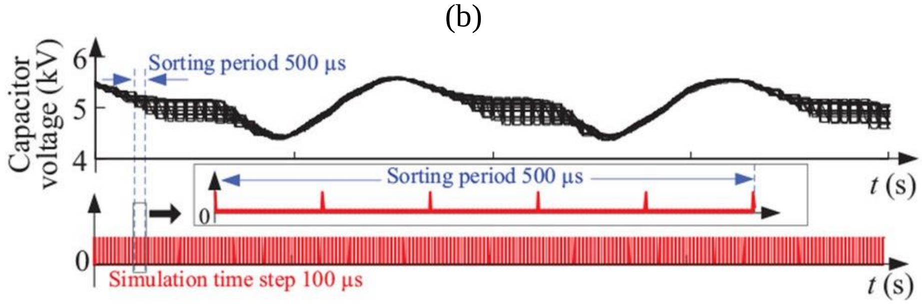

(c)

Figure 4.3 Capacitor voltages with t_{sort} = 500 μs based on various simulation time steps (a) t_{step} = 10 μs, (b) t_{step} = 50 μs, and (c) t_{step} = 100 μs.

4.2.2 Influence of t_{step} on Modulated Arm Voltage

As shown in Fig. 4.4, when fixing the sampling period at 100 μs, the increased simulation time step also leads to additional distortion. To evaluate simulation performance, the errors are calculated for arm and dc currents with various simulation time steps. The average error is calculated from n-point differences between the voltages and currents of the DSM and proposed ECMs, which is given by

$$e_{ave} = \frac{\sum_{i=1}^{n} \left| f_{\mathrm{ECM}}(i) - f_{\mathrm{DSM}}(i) \right|}{n \cdot \max\left(f_{\mathrm{DSM}} \right)} \times 100, \tag{4.4}$$

where n is the number of the selected points, f_{DSM} and f_{ECM} denote the measured values of the DSM and ECMs, respectively. When the simulation time step is much smaller than the sampling period, i.e., t_{step} = 10 μs, the voltage levels can be precisely represented. However, when t_{step} increases, the lost voltage levels may lead to the increased errors in voltage level calculation, as shown in Fig. 4.5.

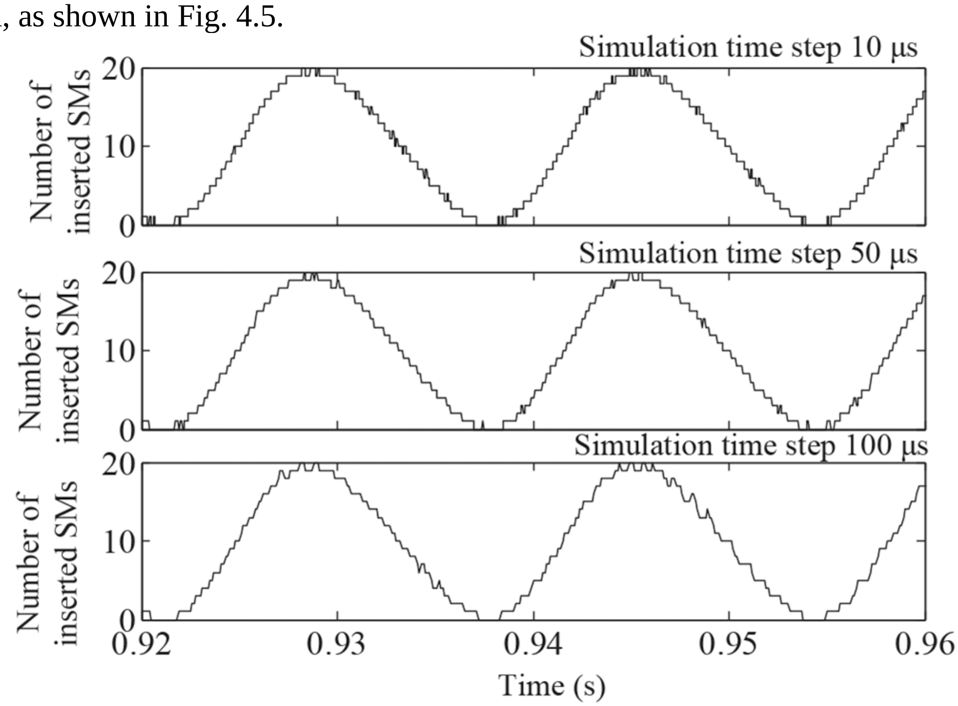

Figure 4.4 Modulated waveform when fixing the sampling period at 100 μs.

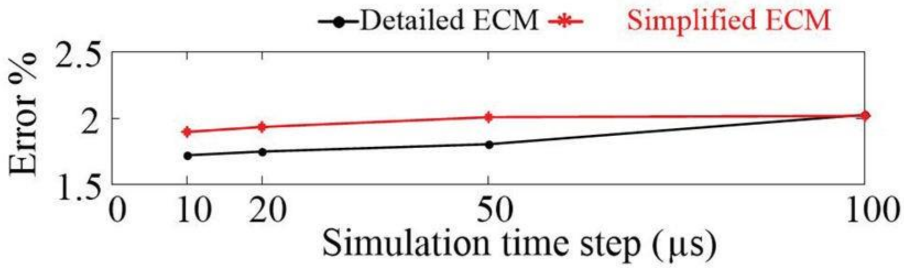

Figure 4.5 Errors of voltage level calculation for various simulation time steps.

4.2.3 Influence of t_{step} on Arm Current and DC Current

When increasing the simulation time step, the lost voltage levels lead to increased pulse width of the arm inductor voltage, as shown in Fig. 4.6. Due to the increased simulation time step, the voltage of arm inductor has less switching actions than that of the DSM. Consequently, the increased simulation time step causes wider pulse of the inductor voltage, leading to the increased arm current ripple. In Fig. 4.6, V_{Lm} denotes the magnitude of the inductor voltage.
The fast Fourier transform (FFT) spectrum of arm and dc voltages and currents are shown in Fig. 4.7 for various simulation time steps. The increased simulation time step introduces more low-order harmonics in arm and dc currents. This means that the equivalent switching frequency is reduced, and the distortion of arm voltage is increased. Based on Fig. 4.8, the increased simulation time step leads to the increased errors in arm current, while the dc current is slightly influenced.

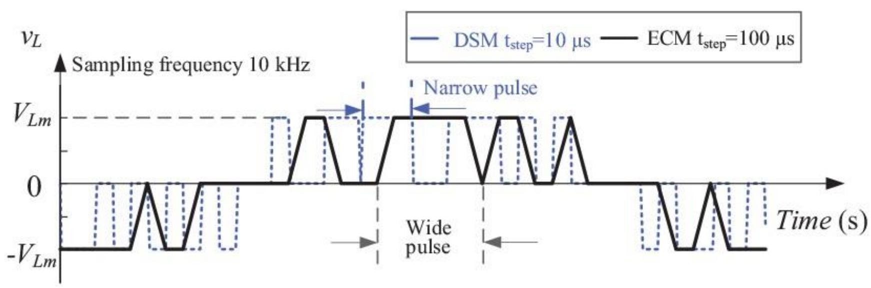

Figure 4.6 Arm inductor voltage.

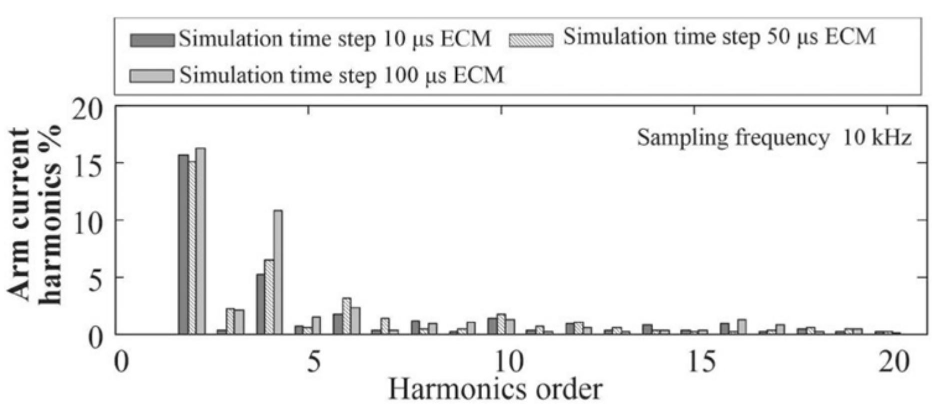

(a)

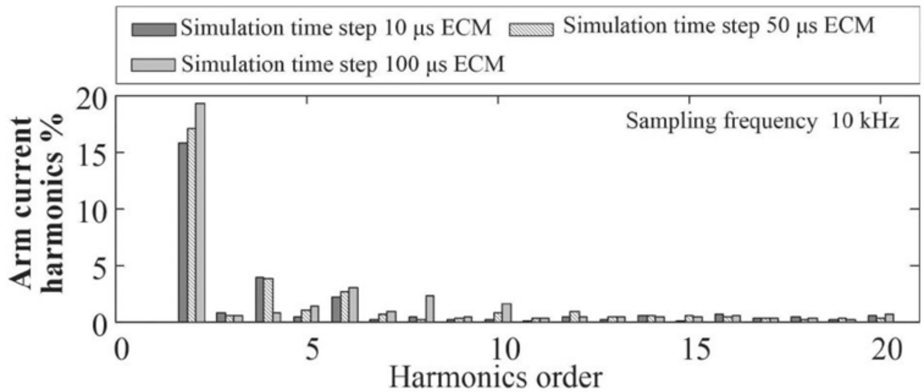

(b)

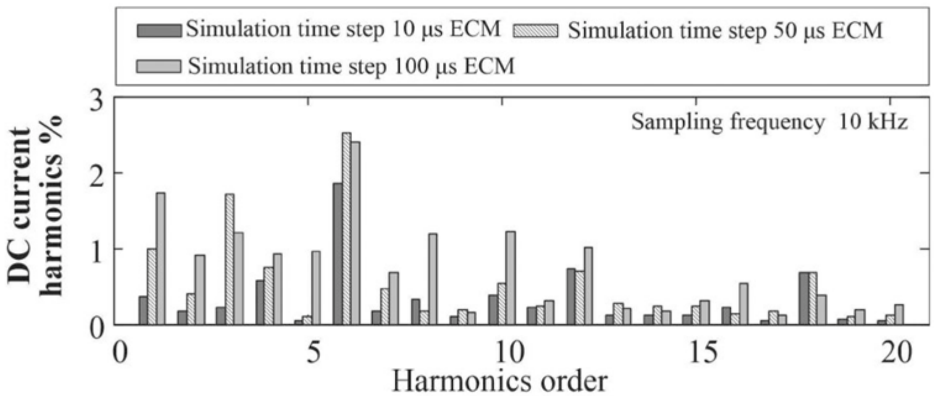

(c)

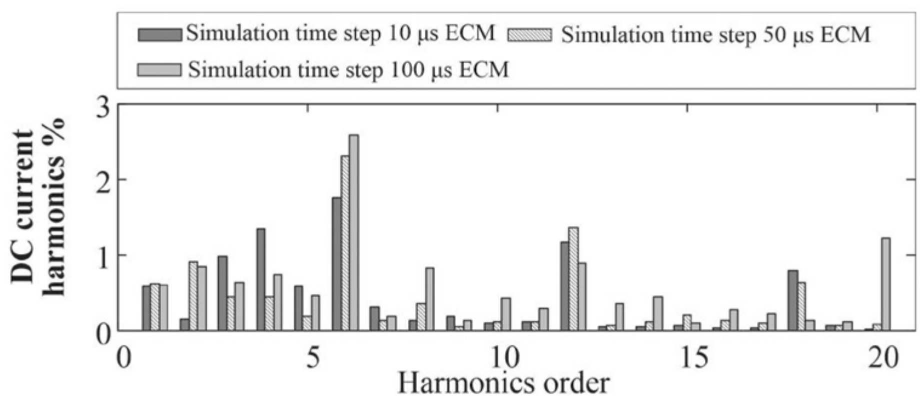

(d)

Figure 4.7 FFT spectrum of (a) Arm current of the detailed ECM, (b) Arm current of the simplified ECM, (c) dc current of the detailed ECM, and (d) dc current of the simplified ECM.

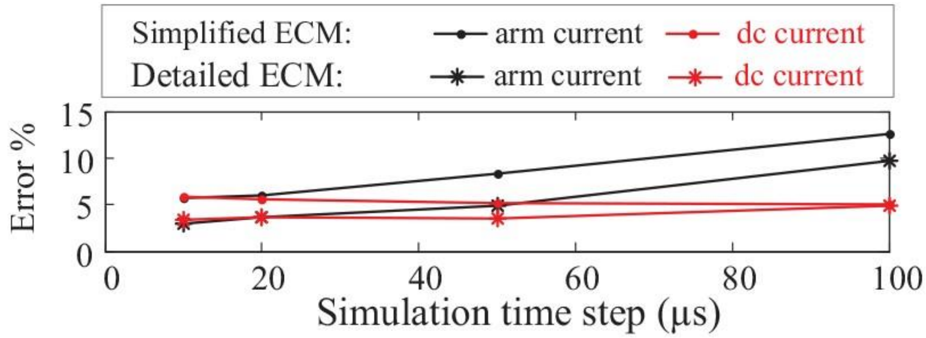

Figure 4.8 Average errors of arm current and dc current based on various simulation time steps.

In addition, based on the results shown in Fig. 4.7, more low-order harmonics are introduced by sorting algorithm. For the detailed ECM, the gating signals are ultimately generated by the sorting algorithm, which increases arm current and voltage distortions. For the simplified ECM, the capacitor voltages are assumed to be well balanced, and the simulation results show lower distortions.

4.2.4 Influence of t_{step} on Simulation Efficiency

The system listed in Table 4.1 is used to evaluate the computational efficiency based on various simulation time steps. The sampling period and sorting period are fixed at 100 μs and the operating time is fixed at 1 s. Figure 4.9 shows the total CPU runtime of the detailed ECM and simplified ECM for various simulation time steps.

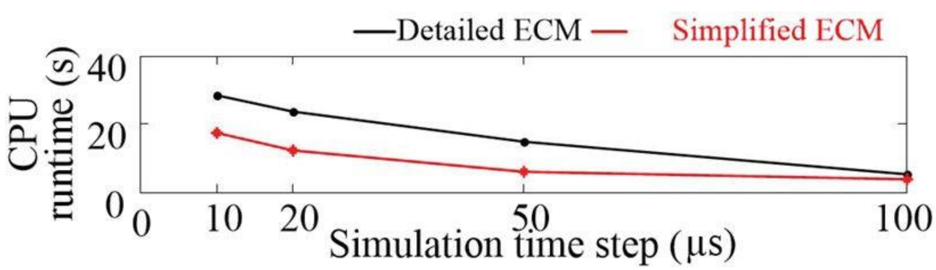

Figure 4.9 Total CPU runtime of the detailed ECM and simplified ECM based on various simulation time steps.

Based on the above analysis, the increased simulation time step leads to higher computational efficiency and lower accuracy. The selection of the simulation time step is a tradeoff between accuracy and computational efficiency. For the study system in this report, the maximum simulation time step of the proposed ECM could be equal to the sampling period.

5. Performance Evaluation and Verification of the Proposed ECM

To verify and validate the proposed ECM, a point-to-point MMC-HVDC system is selected as the study system and built in the PSCAD/EMTDC program environment. The parameters are listed in Table 4.1. The simulation results of the proposed ECM are compared with those of the DSM for various SM configurations and operating conditions.

5.1 The Proposed Detailed ECM

An HB-MMC-HVDC system is modelled and simulated based on the DSM and the proposed detailed ECM, respectively. A dc fault occurs at 0.6 s and the HB-MMC cannot block the fault current fed from the ac grid. The waveforms of the phase-a arm currents, dc currents, and capacitor voltages are compared, which coincide and demonstrate the accuracy of the proposed ECM, as shown in Fig. 5.1. The relative errors are obtained from currents and capacitor voltages of the DSM and detailed ECM, which are shown in Fig. 5.2.

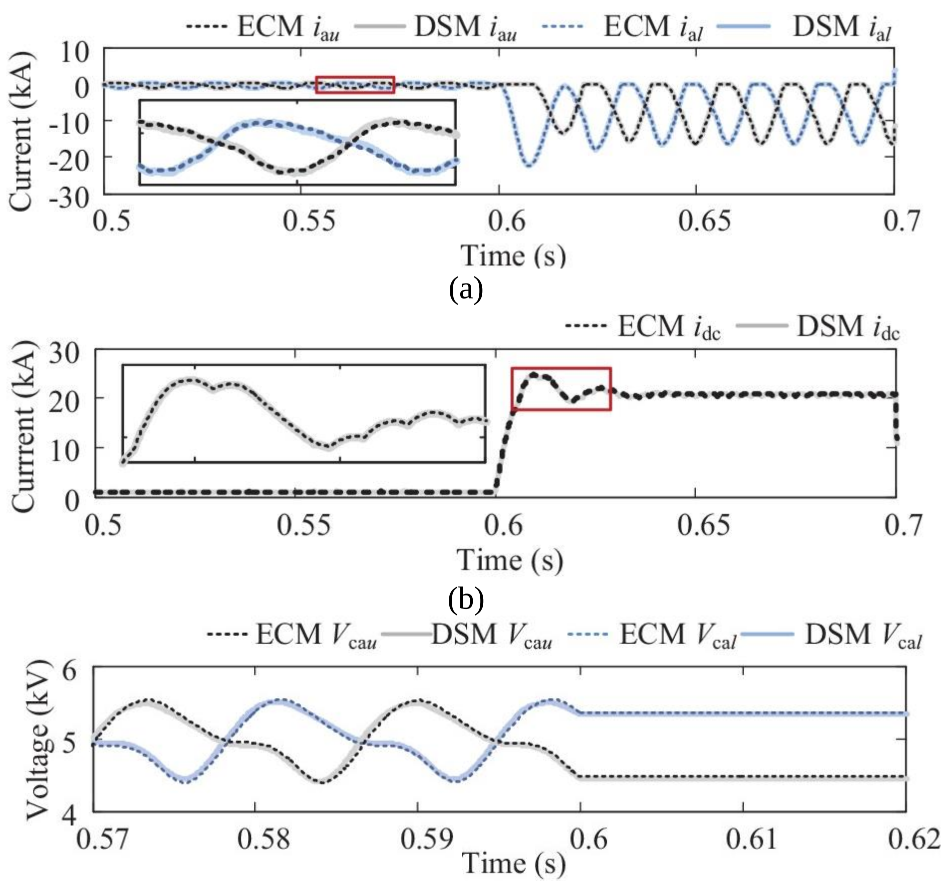

Figure 5.1 Simulation results of the HB-MMC-HVDC based on the DSM and the proposed detailed ECM with t_{step} = 10 μs (a) arm currents, (b) dc currents, and (c) capacitor voltages.

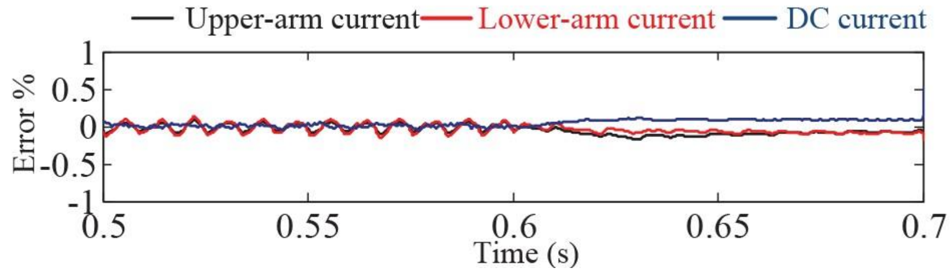

(a)

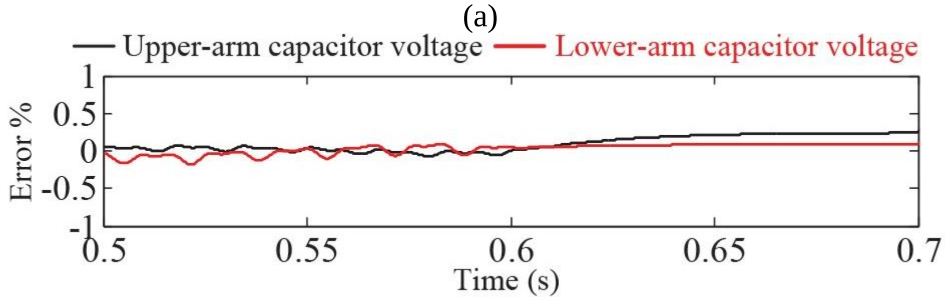

(b)

Figure 5.2 Errors of the HB-MMC-HVDC based on the DSM and the proposed detailed ECM with t_{step} = 10 μs (a) arm currents and dc currents, and (b) capacitor voltages.

The MMCs based on the fault-blocking SMs, such as the FB, UFB, CD, 3LX, and 5LX SMs, have the similar behaviors under normal and fault operating conditions. Figure 5.3 shows the phase-a arm currents, dc currents, and capacitor voltages of the FB-MMC- HVDC system modelled by the DSM and the proposed detailed ECM with t_{step} = 10 μs under various operating conditions. The simulation results demonstrate the effectiveness of the proposed ECM for various operating conditions. Figure 5.4 shows the relative errors of currents and capacitor voltages. Figure 5.5 shows the dc current and capacitor voltages with t_{step} = 100 μs. Based on Figs. 5.3b and 5.5a, the larger simulation time step leads to the increased dc current ripple. In addition, the capacitor voltages of the hybrid MMC based on the proposed detailed ECM are shown in Fig. 5.6. Under normal and dc fault operating conditions, it has similar behavior as the HB MMC. Under precharging condition, during uncontrollable precharging stage, the capacitors in the FB SMs are charged more than those in the HB SMs.

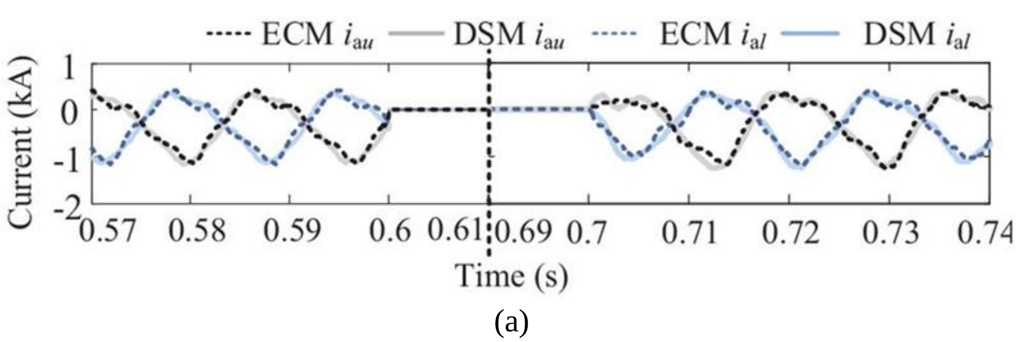

(a)

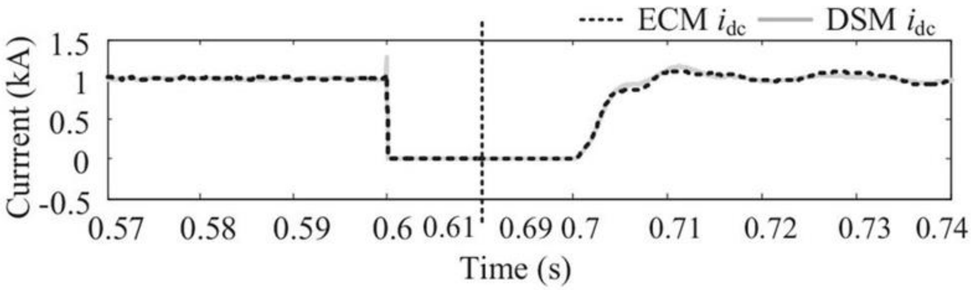

(b)

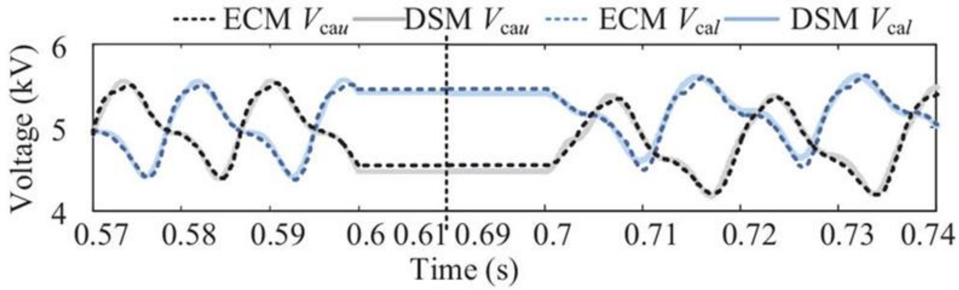

(c)

Figure 5.3 Simulation results of the FB-MMC-HVDC based on the DSM and the proposed detailed ECM with tstep = 10 μs (a) arm currents, (b) dc currents, and (c) capacitor voltages.

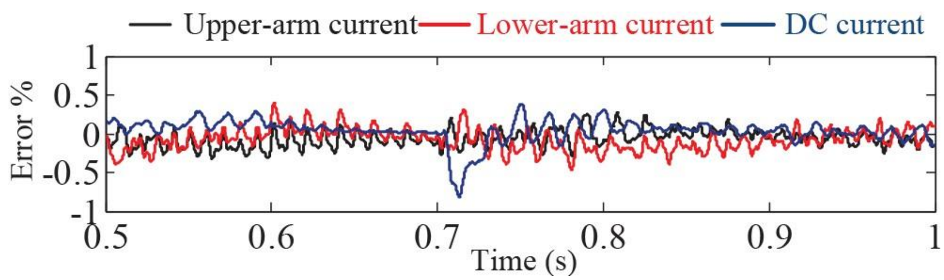

(a)

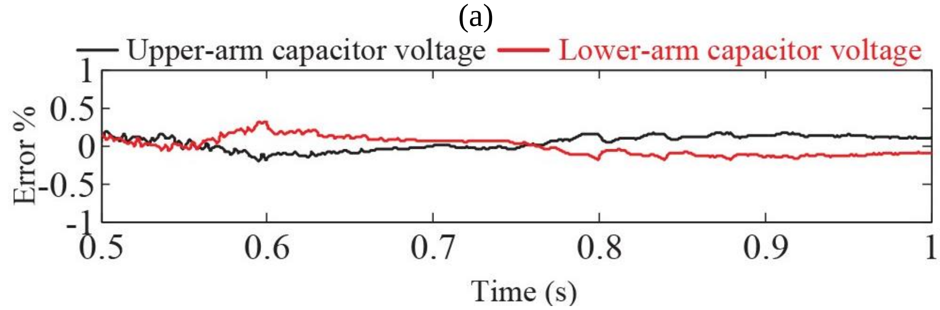

(b)

Figure 5.4 Errors of the FB-MMC-HVDC based on the DSM and the proposed detailed ECM with t_{step} = 10 μs (a) arm currents and dc currents, and (b) capacitor voltages.

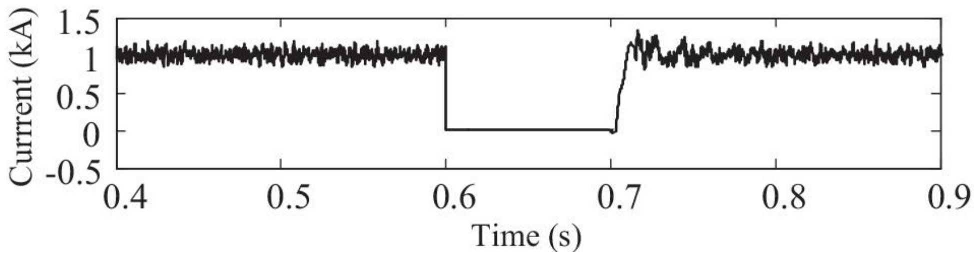

(a)

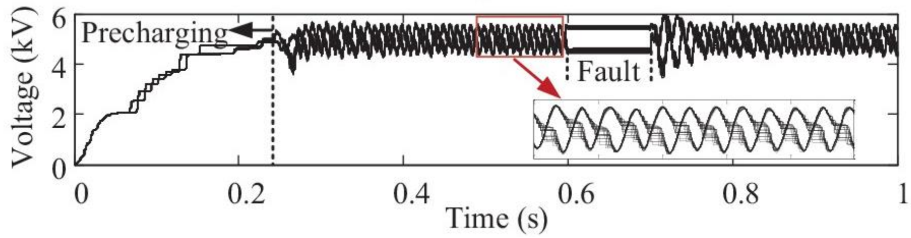

(b)

Figure 5.5 Simulation results of the FB-MMC based on the detailed ECM with t_{step} = 100 μs (a) dc current, and (b) capacitor voltages.

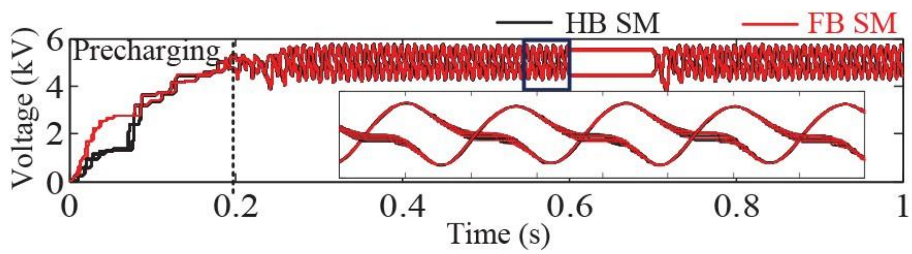

Figure 5.6 Capacitor voltages of the hybrid MMC based on the detailed ECM with t_{step} = 10 μs.

Under dc-fault condition, the MMCs based on the fault- blocking SMs can operate in the STATCOM mode to produce reactive power. The simulation results of the FB-MMC operating in the STATCOM mode are shown in Fig. 5.7. The relative errors are shown in Fig. 5.8.

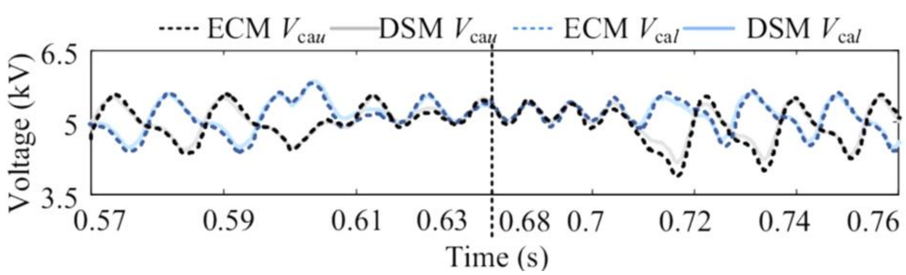

(a)

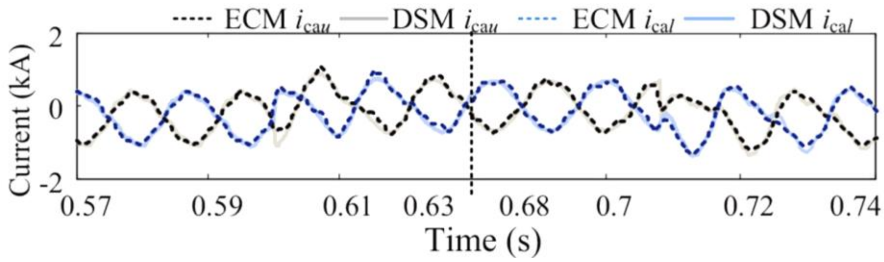

(b)

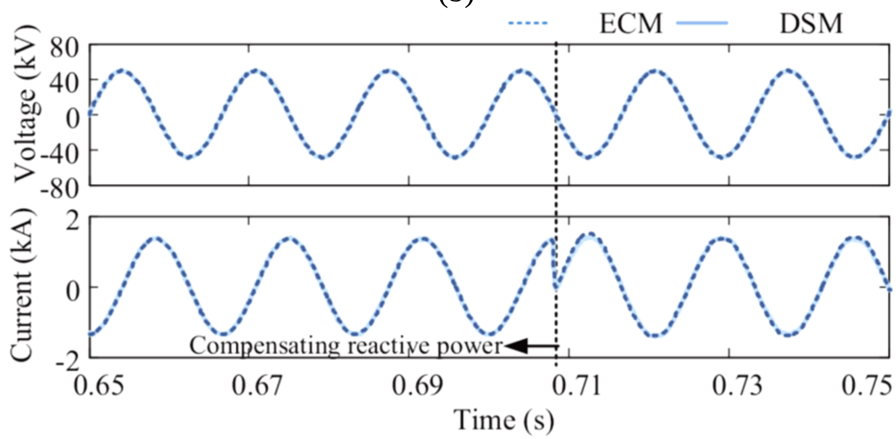

(c)

Figure 5.7 Simulation results of the FB-MMC in the STATCOM mode with tstep = 10 μs (a) capacitor voltages, (b) phase-a arm currents, and (c) ac-side phase current and voltage.

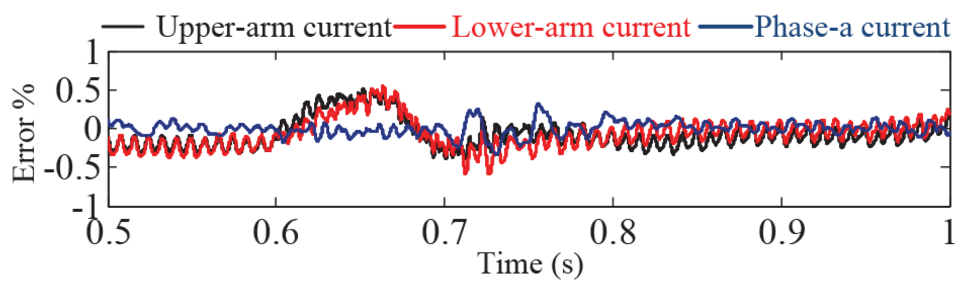

(a)

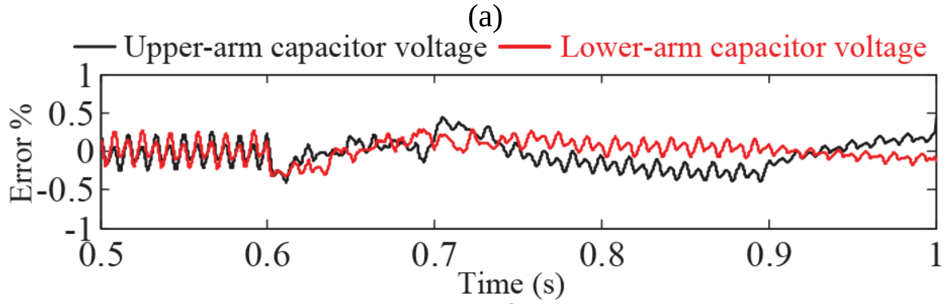

(b)

Figure 5.8 Errors of the FB-MMC in STATCOM mode based on the DSM and the proposed detailed ECM with t_{step} = 10 μs (a) arm currents and dc currents, and (b) capacitor voltages.

5.2 Proposed Simplified ECM

The simplified ECM has better efficiency by considering the average capacitor voltage and neglecting the dynamics of each capacitor voltage.

The phase-a arm currents and capacitor voltages of the HB-MMC-HVDC system based on the simplified ECM and DSM are compared and shown in Fig. 5.9. The relative errors of currents and capacitor voltages are obtained from the DSM and the proposed simplified ECM, which are shown in Fig. 5.10. The simplified ECM leads to larger error than that of the detailed ECM. For the FB-MMC-HVDC, the arm currents and capacitor voltages under various operating conditions are shown in Fig. 5.11. Figure 5.12 shows the relative errors of currents and capacitor voltages obtained from the DSM and the proposed simplified ECM. Figure 5.13 shows the STATCOM operation of the FB-MMC during a dc fault. The relative errors are shown in Fig. 5.14. Figure 5.15 shows the dc current and capacitor voltages with t_{step} = 100 μs. Figure 5.16 demonstrates the behaviors of hybrid MMC based on the proposed simplified ECM. Based on the simulation results, the voltage and current waveforms coincide and the proposed simplified ECM is applicable to various MMC configurations and different operating conditions.

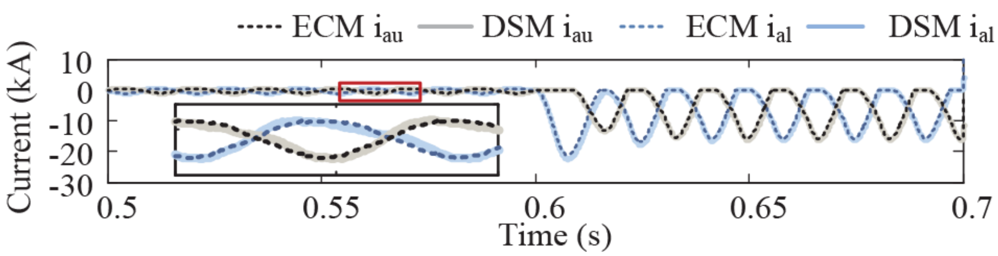

(a)

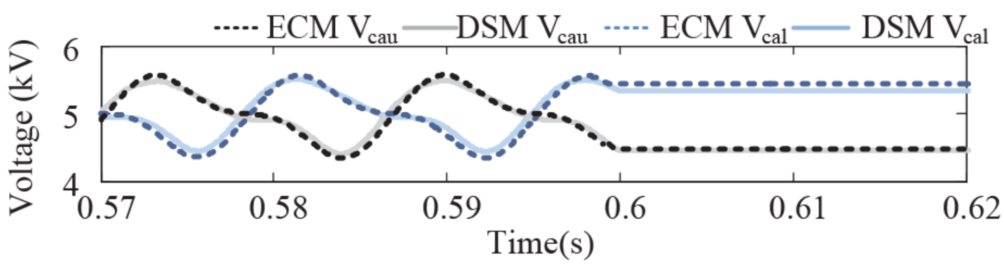

(b)

Figure 5.9 Simulation results of MMC1 of the HB-MMC-HVDC based on the DSM and proposed simplified ECM with t_{step} = 10 μs (a) arm currents, and (b) capacitor voltages.

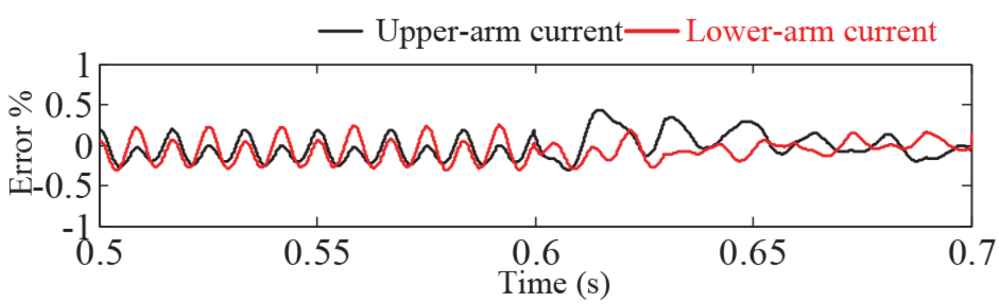

(a)

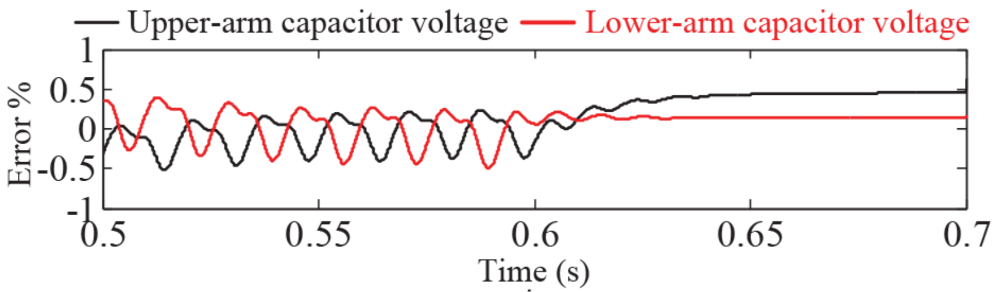

(b)

Figure 5.10 Errors of the HB-MMC-HVDC based on the DSM and the proposed simplified ECM with t_{step} = 10 μs (a) arm currents, and (b) capacitor voltages.

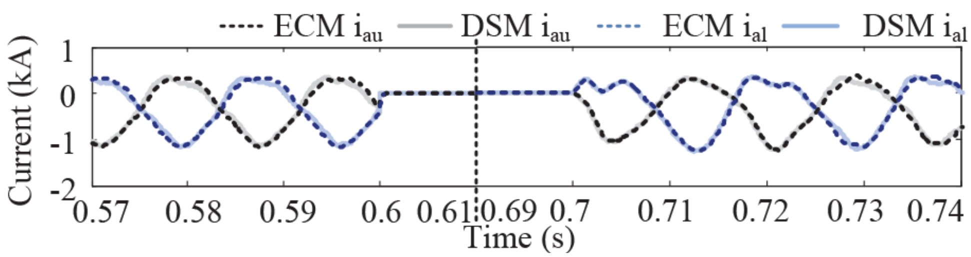

(a)

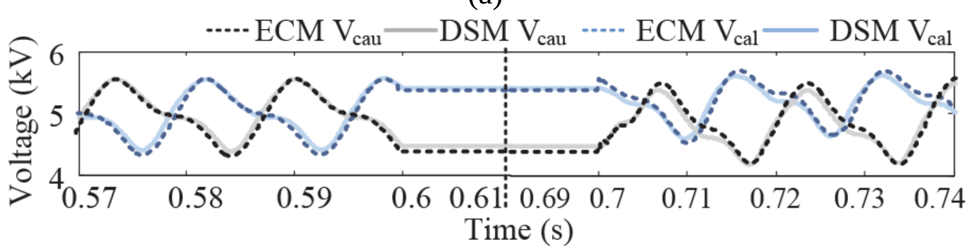

(b)

Figure 5.11 Simulation results of MMC1 of the FB-MMC-HVDC based on the DSM and proposed simplified ECM with t_{step} = 10 μs (a) arm currents, and (b) capacitor voltages.

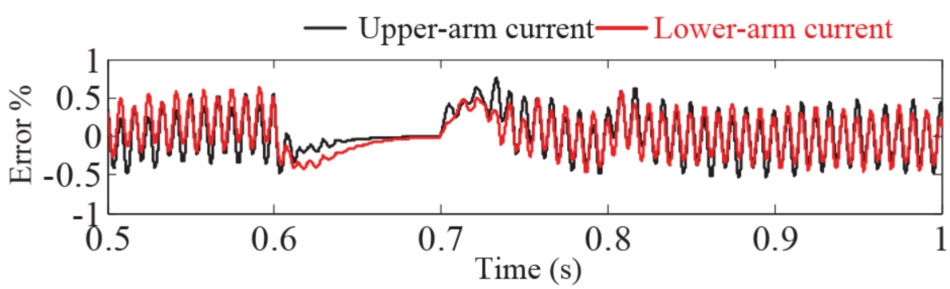

(a)

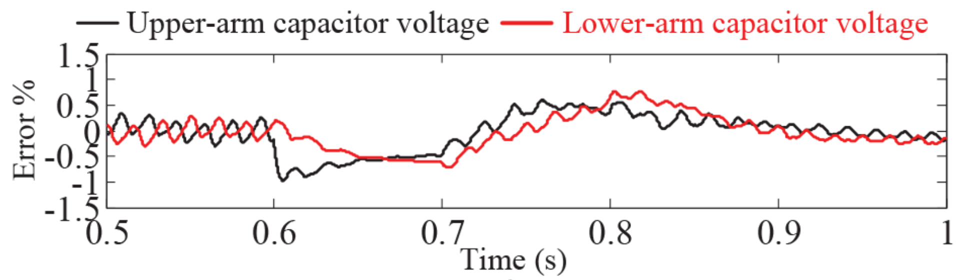

(b)

Figure 5.12 Errors of the FB-MMC-HVDC based on the DSM and the proposed simplified ECM with t_{step} = 10 μs (a) arm currents and dc currrent, and (b) capacitor voltages.

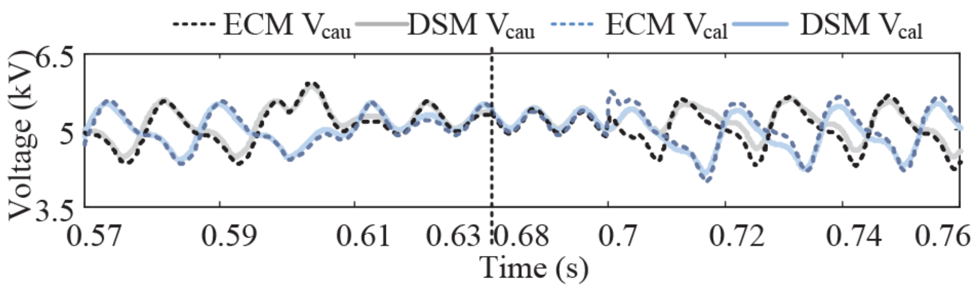

(a)

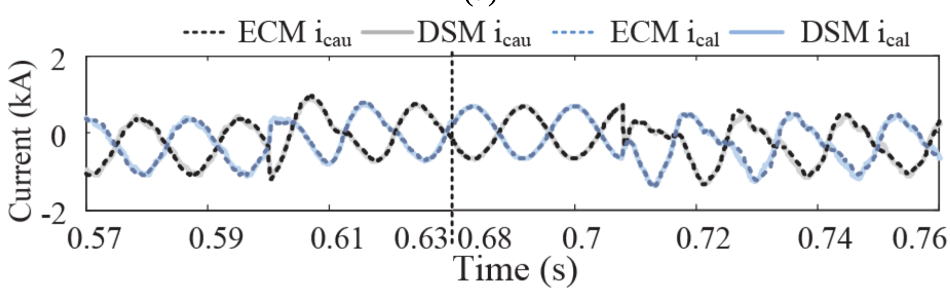

(b)

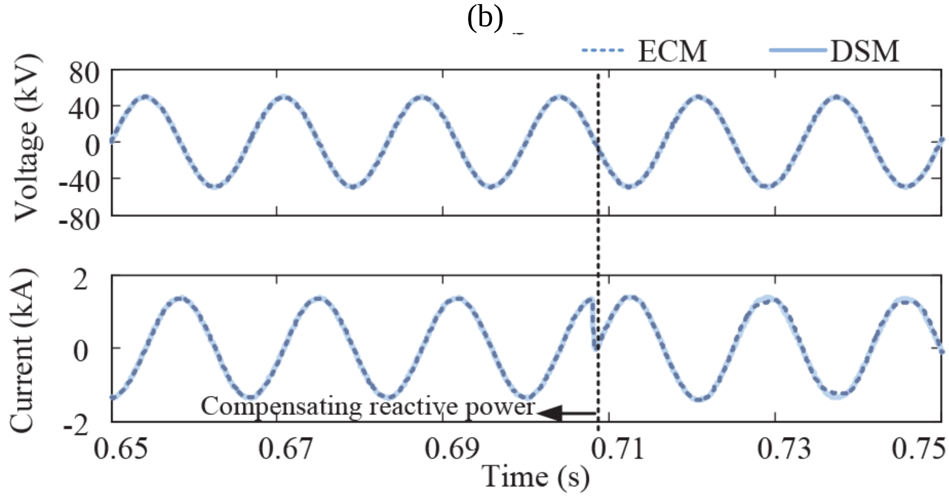

(c)

Figure 5.13 Simulation results of the FB-MMC in the STATCOM mode based on the simplified ECM with t_{step} = 10 μs (a) capacitor voltages, (b) phase-a arm currents, and (c) ac-side phase current and voltage.

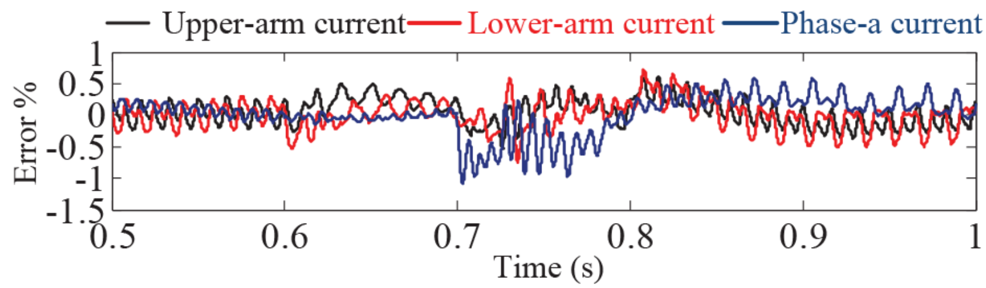

(a)

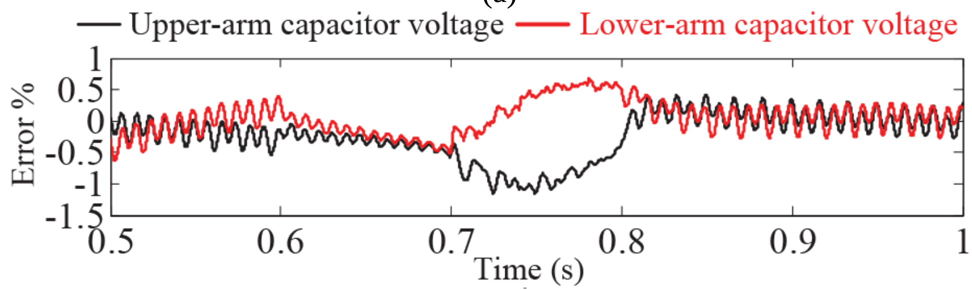

(b)

Figure 5.14 Errors of the FB-MMC in STATCOM based on the DSM and the proposed simplified ECM with t_{step} = 10 μs (a) arm currents and dc currents, and (b) capacitor voltages.

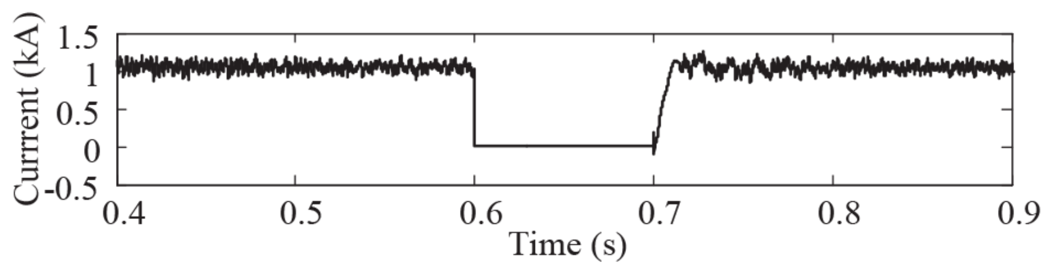

(a)

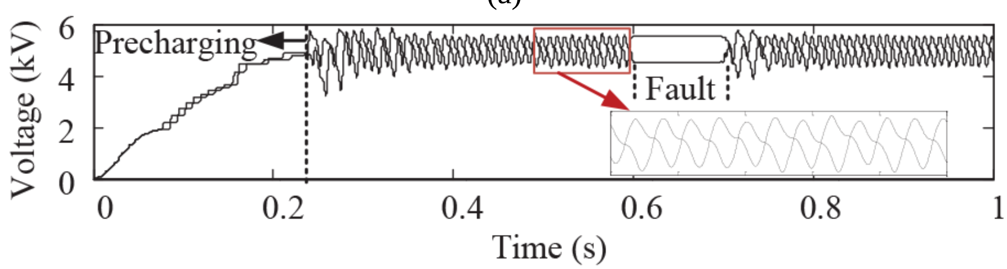

(b)

Figure 5.15 Simulation results of the FB-MMC based on the simplified ECM with t_{step} = 100 μs (a) dc current, and (b) capacitor voltages.

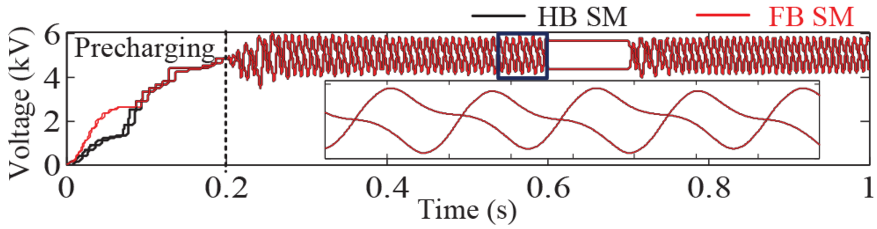

Figure 5.16 Capacitor voltages of hybrid MMC based on ECM with t_{step} = 10 μs.

5.3 Computational Efficiency

5.3.1 MMC-HVDC Systems Based on Various SM Circuits

To evaluate the simulation efficiency of the proposed ECM, the simulation runtime for various MMC-HVDC systems based on the DSM, detailed ECM, and simplified ECM is listed in Table 5.1. The system operating time is 1 s and the simulation time step is 10 μs. The simulation is conducted on the operating system of Microsoft Windows 10 with a 2.60 GHz Intel Core i7-6700HQ CPU and 8 GB of RAM.

As shown in Table 5.1, the proposed ECM can significantly improve the computational efficiency as compared with the conventional DSM while keeping high accuracy. The increasing complexity of SM circuit topologies will severely reduce the simulation efficiency of the conventional DSM. Moreover, the simulation efficiency of the proposed ECM is almost not affected by the complexity of SM circuit topologies.

Table 5.1 Comparison of Simulation Runtimes for Various MMC-HVDC Systems Based on the DSM and the Proposed ECM

MMC configuration	**DSM runtime (s)**	**ECM runtime (s)**	
		Detailed	**Simplified**
HB	1656.21	30.67	11.52
FB	8512.72	31.34	11.73
CD	21,877.39	30.31	12.38
3LX	29,097.14	30.84	12.21
Hybrid (HB and FB)	3179.83	30.56	11.94

5.3.2 High-level MMC-HVDC Systems

Table 5.2 shows the simulation runtime for the MMC-HVDC systems with various voltage levels. As the increasing of the number of SMs, although the simulation runtime of the proposed ECM increases, it is still much smaller than that of the conventional DSM.

Table 5.2 Comparison of Simulation Runtime of the MMC-HVDC Systems with Various Voltage Levels

Number of SMs per arm	**ECM runtime (s)**	
	Detailed	**Simplified**
20	31.34	11.73
40	37.11	12.03
60	43.89	12.45
80	47.80	12.71
100	54.62	13.12
200	96.56	16.29

6. Conclusion

A general ECM is proposed for modelling and simulating the MMCs based on various SM circuits under different operating conditions. The proposed detailed ECM considers internal state variables and can be used to evaluate the dynamic performance of an MMC with considering a practical industrial controller. To further improve simulation efficiency, the simplified ECM is derived by neglecting the dynamics of individual capacitor voltage. The study results show that the selection of the simulation time step influences simulation efficiency and accuracy. For the given study system, the maximum simulation time step could be equal to the sampling period (or control period) of the practical controller for highest simulation efficiency while keeping good accuracy. The study results also show that the complexity of SM circuit topologies significantly affects the simulation efficiency of the conventional DSM. However, the proposed ECM can keep the same high-efficiency simulation for various SM circuits regardless of the complexity of SM circuit topologies.

References

[1] Debnath, S., Qin, J., Bahrani, B., et al.: "Operation, control, and applications of the modular multilevel converter: A review", IEEE Trans. Power Electron., vol. 30, no. 1, March 2015, pp. 37–53.

[2] Li, R., Xu, L., Yao, L., et al.: "Active control of DC fault currents in DC solid-state transformers during ride-through operation of multi-terminal HVDC systems", IEEE Trans. Energy Convers., vol. 31, no. 4, June 2016, pp. 1336–1346.

[3] Adam, G.P., Williams, B.W.: "Half- and full-bridge modular multilevel converter models for simulations of full-scale HVDC links and multiterminal DC grids", IEEE J. Emerg. Sel. Top. Power Electron., vol. 2, no. 4, April 2014, pp. 1089–1108.

[4] Wu, D., Peng, L.: "Analysis and suppressing method for the output voltage harmonics of modular multilevel converter", IEEE Trans. Power Electron., vol. 31, no. 7, July 2016, pp. 4755–4765.

[5] Gnanarathna, U.N., Gole, A.M., Jayasinghe, R.P.: "Efficient modeling of modular multilevel HVDC converters (MMC) on electromagnetic transient simulation programs", IEEE Trans. Power Del., vol. 26, no. 1, Jan. 2011, pp. 316–324.

[6] Peralta, J., Saad, H., Dennetière, S., et al.: "Detailed and averaged models for a 401-level MMC-HVDC system", IEEE Trans. Power Del., vol. 27, no. 3, July 2012, pp. 1501–1508.

[7] Xu, J., Zhao, C., Liu, W., et al.: "Accelerated model of modular multilevel converters in pscad/emtdc", IEEE Trans. Power Del., vol. 28, no. 1, Jan.2013, pp. 129–136.

[8] Saad, H., Peralta, J., Dennetiere, S., et al.: "Dynamic averaged and simplified models for MMC-based HVDC transmission systems", IEEE Trans. Power Del., vol. 28, no. 3, July 2013, pp. 1723–1730.

[9] Ou, K., Rao, H., Cai, Z., et al.: "MMC-HVDC Simulation and testing based on real-time digital simulator and physical control system", IEEE J. Emerg. Sel. Top. Power Electron, vol. 2, no. 4, Dec. 2014, pp. 1109–1116.

[10] Ajaei, F.B., Iravani, R.: "Enhanced equivalent model of the modular multilevel converter", IEEE Trans. Power Del., vol. 30, no. 2, April 2015, pp. 666–673.

[11] Saad, H., Ould-Bachir, T., Mahseredjian, J., et al.: "Real-time simulation of mmcs using cpu and fpga", IEEE Trans. Power Electron., vol. 30, no. 1, Jan. 2015, pp. 259–267.

[12] Li, W., Belanger, J.: "An equivalent circuit method for modelling and simulation of modular multilevel converters in real-time HIL test bench", IEEE Trans. Power Del., vol. 31, no. 5, Oct. 2016, pp. 2401–2409.

[13] Lin, N., Dinavahi, V.: "Behavioral device-level modeling of modular multilevel converters in real time for Variable-speed drive applications", IEEE J. Emerg. Sel. Top. Power Electron., vol. 5, no. 3, Sept. 2017, pp. 1177–1191.

[14] Li, R., Xu, L., Guo, D.: "Accelerated switching function model of hybrid MMCs for HVDC system simulation", IET Power Electron., vol. 10, no. 15, Sept. 2017, pp. 2199–2207.

[15] Yang, H., Dong, Y., Li, W., et al.: "Average-value model of modular multilevel converters considering capacitor voltage ripple", IEEE Trans. Power Del., vol. 32, no. 2, April 2017, pp. 723–732.

[16] Ahmed, N., Ängquist, L., Mahmood, S., et al.: "Efficient modeling of an MMC-based multiterminal DC system employing hybrid HVDC breakers", IEEE Trans. Power Del., vol. 30, no. 4, Aug. 2015, pp. 1792–1801.

[17] Zhang, L., Qin, J., Shi, D., et al.: "Efficient modeling of hybrid MMCs for HVDC systems". 2017 IEEE Energy Conversion Congress and Exposition (ECCE), Cincinnati, OH, USA, 2017, pp. 1629–1633.
[18] Xiang, W., Lin, W., An, T., et al.: "Equivalent electromagnetic transient simulation model and fast recovery control of overhead VSC-HVDC based on SB-MMC", IEEE Trans. Power Del., vol. 32, no. 2, April 2017, pp. 778–788.
[19] Ashourloo, M., Mirzahosseini, R., Iravani, R.: "Enhanced model and real-time simulation architecture for modular multilevel converter", IEEE Trans. Power Del., vol. 33, no. 1, Feb. 2018, pp. 466–476.
[20] Tu, Q., Xu, Z.: "Impact of sampling frequency on harmonic distortion for Modular Multilevel Converter", IEEE Trans. Power Del., vol. 26, no. 1, Jan. 2011, pp. 298–306.
[21] Xu, J., Zhao, C., Xiong, Y., et al.: "Optimal design of MMC levels for electromagnetic transient studies of MMC-HVDC", IEEE Trans. Power Del., vol. 31, no. 4, Aug. 2016, pp. 1663–1672.
[22] Qin, J., Saeedifard, M., Rockhill, A., et al.: "Hybrid design of modular multilevel converters for HVDC systems based on various submodule circuits", IEEE Trans. Power Del., vol. 30, no. 1, Feb. 2015, pp. 385–394.
[23] Yu, X., Wei, Y., Jiang, Q.: "STATCOM operation scheme of the CDSM-MMC during a pole-to-pole DC fault", IEEE Trans. Power Del., vol. 31, no. 3, June 2016, pp. 1150–1159.
[24] Nguyen, T.H., Al Hosani, K., ElMoursi, M.S., et al.: "An overview of modular multilevel converters in HVDC transmission systems with STATCOM operation during pole-to-pole DC short circuits", IEEE Trans. Power Electron., vol. 34, no. 5, May 2019, pp. 4137–4160.
[25] Zhang, L., Qin, J., Wu, X., et al.: "A generalized precharging strategy for soft startup process of the modular multilevel converter-based HVDC systems", IEEE Trans. Ind. Appl., vol. 53, no. 6, Nov. 2017, pp. 5645–5657.
[26] Shi, X., Liu, B., Wang, Z., et al.: "Modeling, control design, and analysis of a startup scheme for modular multilevel converters", IEEE Trans. Ind. Electron., vol. 62, no. 11, Nov.2015, pp. 7009–7024.
[27] Tu, Q., Xu, Z., Xu, L.: "Reduced switching-frequency modulation and circulating current suppression for modular multilevel converters", IEEE Trans. Power Del., vol. 26, no. 3, July 2011, pp. 2009–2017.
[28] Qin, J., Saeedifard, M.: "Reduced switching-frequency voltage-balancing strategies for Modular Multilevel HVDC converters", IEEE Trans. Power Del., vol. 28, no. 4, Oct. 2013, pp. 2403–2410.
[29] Du, S., Liu, J., Liu, T.: "Modulation and closed-loop-based DC capacitor voltage control for MMC with fundamental switching frequency", IEEE Trans. Power Electron., vol. 30, no. 1, Jan. 2015, pp. 327–338.
[30] Deng, F., Chen, Z.: "Voltage-balancing method for Modular Multilevel converters switched at grid frequency", IEEE Trans. Ind. Electron., vol. 62, no. 5, May 2015, pp. 2835–2847.
[31] Chen, G., Peng, H., Zeng, R., et al.: "A fundamental frequency sorting algorithm for capacitor voltage balance of modular multilevel converter with low-frequency carrier phase shift modulation", IEEE J. Emerg. Sel. Top. Power Electron., vol. 6, no. 3, March 2018, pp. 1595–1604.

Part II

Modeling of MMC-MTDC Systems

Jiangchao Qin
Yuntao Zou, Graduate Student

Arizona State University

For information about this project, contact:

Jiangchao Qin
Arizona State University
School of Electrical, Computer, and Energy Engineering
PO Box 875706
Temp, AZ 85287-5706
Fax: 480-727-2052
Email: jqin@asu.edu

Power Systems Engineering Research Center

The Power Systems Engineering Research Center (PSERC) is a multi-university Center conducting research on challenges facing the electric power industry and educating the next generation of power engineers. More information about PSERC can be found at the Center's website: http://www.pserc.org.

For additional information, contact:

Power Systems Engineering Research Center
Arizona State University
527 Engineering Research Center
Tempe, Arizona 85287-5706
Phone: 480-965-1643
Fax: 480-727-2052

Notice Concerning Copyright Material

Table of Contents

List of Figures

List of Tables

1. Introduction

1.1 Background

Nowadays, with the integrations of renewable energy and the increased demands of bulk power transmission, the MMC-MTDC system with droop control and intricate dc network has been becoming spectacularly complicated [1-6]. Multiple controllers exist in the MTDC systems, e.g., *dq* controllers for the power control in the multiple MMC stations. Furthermore, due to varying power flows of the integrated renewable energy generators and loads, the droop controller is widely applied in MMC-MTDC system to address the automatic power balancing in the MTDC system, which leads to intricate couplings between control variables. Considering the interlaced dynamic feedback loops in system-level, the MMC-MTDC system has developed into a high dimensional nonlinear system, which significantly increases the difficulty for modeling and simulation in large scale power system.

1.2 Overview of the MMC-MTDC Modeling

With the growing applications in the MTDC system, many previous works have discussed the modeling of MMC-MTDC systems. However, modeling of the MMC-MTDC systems in previous work is insufficient and inadequate.

The topologies of the study systems emphasized in existing work are usually simple and special. For example, some references adopt the ideal common-bus as the topology of MTDC system [5, 7, 8]. This topology can be simplified through the equivalence that the converters can be combined as one equivalent converter. The impedance of common bus is neglected so that the analysis or control designing does not need to consider the influence of dc networks. But the accuracy of models and the study results based on these models cannot be convinced since this simplification is not wildly suitable for all common-bus systems. Also, the common-bus system cannot represent practical MTDC systems.

In references [4, 9, 10], the topologies of the study systems are still the common-bus but the impedance between connections is considered. Compared with the topology of ideal common-bus, these topologies are equivalent to the radial network. References [1, 6, 10, 11] directly use the multiple terminal radial dc networks. On the other side, references [2, 13, 14, 15] use more complicated topologies rather than radial networks, e.g., three-terminal or four-terminal annular networks. These networks are more general and accurate for the analysis of dynamic behavior and control design for MTDC systems.

Therefore, it is necessary to develop a systematic modeling method for the dc network. Meanwhile, this method cannot be affected by the topology of dc network and the model of transmission lines or cables, which should be a generalized solution.

1.3 Report Organization

This report is structured as follows. Chapter 2 develops the models of the MMC, dq controller, and dc network. In Chapter 3, a general model of MMC-MTDC system is developed. Simulation verification is presented in Chapter 4. Chapter 5 concludes the report.

2. Modeling of The MMC, *dq* Controller, and DC Network

A generalized model of the MMC-MTDC system is developed in this section. The modeling method is applicable for different MMCs, controllers, dc overhead transmission line, and arbitrary topology of dc network.

At first, modeling of each element will be introduced, including MMC, *dq* controller, droop controller, and dc network. The arm switching function model of the MMC and the T equivalent circuit of dc overhead transmission line are utilized. Meanwhile, a method for the dc network modeling with arbitrary topology is expressed based on the edge-node incidence matrix. It is not constrained by the adopted model of transmission lines. Since it considers the dc load bus and the interconnecting bus, this method is also suitable for other applications, e.g., microgrid modeling.

Considering multiple MMCs, their associated controllers, and the whole dc network in system, a derivation is expressed to get the small-signal model of the whole MTDC system. During the derivation, a particular arrangement providing a uniform form of matrix is considered to organize and construct the interconnected parallel sub-systems. Thus, by following this arrangement, the size of the submatrices will be conveniently adjusted when the number of MMC stations or the number of the dc network terminals is changed.

A 4-terminal and a 14-terminal MMC-based ±500 kV MTDC systems are employed as the study systems. The MMC sub-module (SM) is the half-bridge circuit. Since concentrating on the system transient operation without ac or dc faults, the unsymmetrical condition is ignored and the high short-circuit-ratio of the MMC integrated ac system is assumed. On the other side, to reduce the complexity of formula's expression, a remark for the formula notation is listed as well.

- *Remark*: if there is a sequence of variable X with subscript y and superscript z shown as $X_{y1}^{z}, X_{y2}^{z}, \cdots, X_{yi}^{z}$ and i is some integer, a notation for vector and diagonal matrix with the same subscript and superscript comprised by them will be respectively expressed as

$$X_{[\vec{y}]}^{z} = \left[X_{y1}^{z}, X_{y2}^{z}, \cdots, X_{yi}^{z} \right]^{T}.$$
$$X_{\Lambda[y]}^{z} = diag\left(\left[X_{y1}^{z}, X_{y2}^{z}, \cdots, X_{yi}^{z} \right]^{T} \right).$$

2.1 Modeling of MMC

To guarantee the accuracy of modeling of MMC-MTDC system, the arm switching function [16] for the modeling of MMC is employed. The schematic diagram of MMC stations containing dc and ac side is shown in Fig. 2.1, where L_s and C_g are the smoothing reactor and the grounding capacitor in dc side, respectively. The other notations of Fig. 2.1 will be introduced later in the associated formulas. To distinguish the MMC dc-side voltage and the dc-bus voltage connected with MMC station, different notations are applied as v_{dc} for the MMC dc-side voltage and v_{dc_bus} for the dc-bus voltage of dc network, respectively.

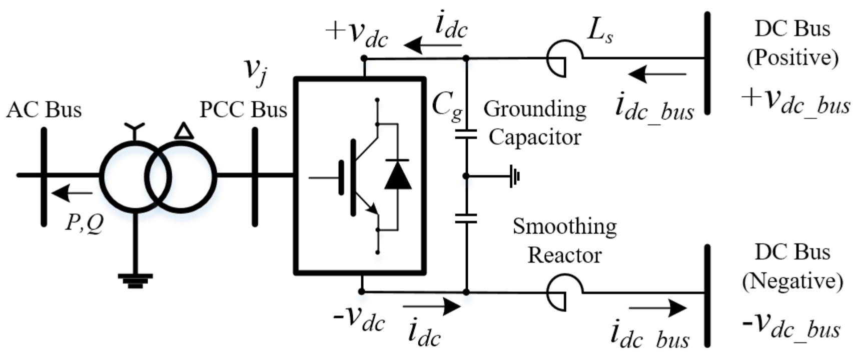

Figure 2.1 The schematic diagram of an MMC station.

The equivalent circuit of the MMC arm switching function model is shown in Fig. 2.2 for three-phase, where $j = a, b, c$. N is the number of the sub-modules in each arm and C_{SM} is the capacitance of each sub-module. L_{arm} and R_{arm} are the arm inductance and resistance, respectively. L_0 and R_0 are the inductance and resistance of point of common coupling (PCC), respectively. The circuit equations of upper and lower arms are given by formula (2.1).

$$\begin{aligned} v_{dc} - S_{jp}v_{jp} - R_{arm}i_{jp} - L_{arm}\frac{di_{jp}}{dt} &= v_j^{ac}, \\ -v_{dc} + S_{jn}v_{jn} + R_{arm}i_{jn} + L_{arm}\frac{di_{jn}}{dt} &= v_j^{ac}, \end{aligned} \tag{2.1}$$

where S_{jp} and S_{jn} are the switching functions of MMC upper and lower arms, respectively. v_{jp}, v_{jn}, i_{jp}, and i_{jn} are the arm equivalent capacitor voltage and arm current of MMC upper and lower arm, respectively. v_j^{ac} is the MMC ac-side voltage.

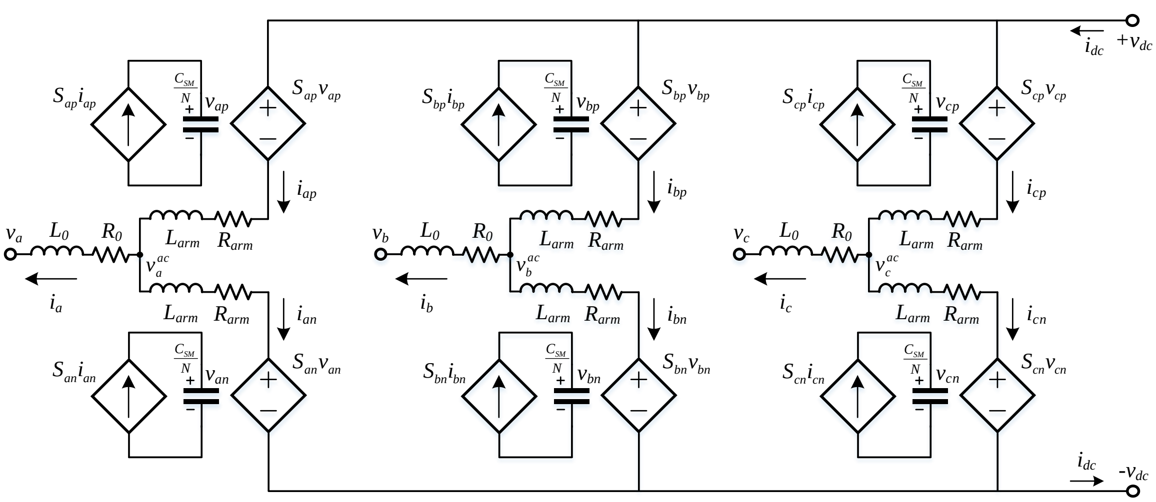

Figure 2.2 The equivalent circuit of the arm switching function model.

Moreover, the circuit equations of the each arm equivalent capacitor indicating the charging and discharging dynamic of all SMs are given by (2.2).

$$\frac{C_{SM}}{N}\frac{dv_{jp}}{dt} = S_{jp} i_{jp}, \quad \frac{C_{SM}}{N}\frac{dv_{jn}}{dt} = S_{jn} i_{jn}. \tag{2.2}$$

The circuit equation of the MMC ac-side for the PCC dynamic is given by (2.3).

$$v_j^{ac} = v_j + R_0 i_j + L_0 \frac{di_j}{dt}, \tag{2.3}$$

where v_j is the three-phase voltage of PCC bus, which is regarded as the constant.

Even though multiple harmonic components are contained in each arm voltage and current, the higher order harmonic components are neglected since the dc, fundamental-frequency and second-order harmonic component dominate the MMC dynamic behavior [17]. Therefore, in this report, the MMC modeling will concentrate on the dynamics of the dc, fundamental-frequency, and second-order harmonic component. The currents and voltages of each arm will be comprised by the components defined in (2.4), where v^{dc}, $v_j^{\omega_0}$, $v_j^{2\omega_0}$ and i_{dc}, i_j, $i_j^{2\omega_0}$ are dc, fundamental-frequency and second-order harmonic voltages and currents, respectively.

$$\begin{aligned} v_{jp} &= v^{dc} + v_j^{\omega_0} + v_j^{2\omega_0}, \quad i_{jp} = \frac{1}{3} i_{dc} + \frac{1}{2} i_j + i_j^{2\omega_0}, \\ v_{jn} &= v^{dc} - v_j^{\omega_0} + v_j^{2\omega_0}, \quad i_{jn} = \frac{1}{3} i_{dc} - \frac{1}{2} i_j + i_j^{2\omega_0}. \end{aligned} \tag{2.4}$$

Ignoring the impact of the nearest level modulation (NLM), i.e., distortion of the reference wave, the switching functions S_{jp} and S_{jn} of MMC with the voltage references generated by controller are given by (2.5).

$$S_{jp} = \frac{1}{2} + \frac{v_j^{ref}}{\tilde{V}_{dc}}, \quad S_{jn} = 1 - S_{jp} = \frac{1}{2} - \frac{v_j^{ref}}{\tilde{V}_{dc}}, \tag{2.5}$$

where $\tilde{V}_{dc}$ is the nominal MMC dc-side voltage and v_j^{ref} is the three-phase voltage reference generated by MMC controller.

Involving (2.4) and (2.5) into (2.1), (2.2) and (2.3), the 10-order MMC model in the *dq* reference frame with fundamental and double fundamental frequency is shown as (2.6). The notation of three-phase coordination *j* is replaced by *d* and *q* in the *dq* reference frame.

$$\begin{aligned}
\frac{di_{dc}}{dt} &= -c_1 i_{dc} + c_2 v_{dc} - \frac{1}{2} c_2 v^{dc} + 3c_3 \left(v_d^{\omega_0} v_d^{ref} + v_q^{\omega_0} v_q^{ref} \right), \\
\frac{di_d}{dt} &= -c_4 i_d + \omega_0 i_q - 2c_5 v_d - c_5 v_d^{\omega_0} + c_6 v^{dc} v_d^{ref} + \frac{1}{2} c_6 \left(v_d^{2\omega_0} v_d^{ref} + v_q^{2\omega_0} v_q^{ref} \right), \\
\frac{di_q}{dt} &= -c_4 i_q - \omega_0 i_d - 2c_5 v_q - c_5 v_q^{\omega_0} + c_6 v^{dc} v_q^{ref} + \frac{1}{2} c_6 \left(v_q^{2\omega_0} v_d^{ref} - v_d^{2\omega_0} v_q^{ref} \right), \\
\frac{di_d^{2\omega_0}}{dt} &= c_3 \left(v_d^{\omega_0} v_d^{ref} - v_q^{\omega_0} v_q^{ref} \right) - c_1 i_d^{2\omega_0} + 2\omega_0 i_q^{2\omega_0} - \frac{1}{6} c_2 v_d^{2\omega_0}, \\
\frac{di_q^{2\omega_0}}{dt} &= c_3 \left(v_q^{\omega_0} v_d^{ref} + v_d^{\omega_0} v_q^{ref} \right) - c_1 i_q^{2\omega_0} - 2\omega_0 i_d^{2\omega_0} - \frac{1}{6} c_2 v_q^{2\omega_0}, \\
\frac{dv^{dc}}{dt} &= \frac{2}{3} c_7 i_{dc} - c_8 \left(i_d v_d^{ref} + i_q v_q^{ref} \right), \\
\frac{dv_d^{\omega_0}}{dt} &= c_7 i_d + \omega_0 v_q^{\omega_0} - \frac{4}{3} i_{dc} v_d^{ref} - 2c_8 \left(i_d^{2\omega_0} v_d^{ref} + i_q^{2\omega_0} v_q^{ref} \right), \\
\frac{dv_q^{\omega_0}}{dt} &= c_7 i_q - \omega_0 v_d^{\omega_0} - \frac{4}{3} i_{dc} v_q^{ref} - 2c_8 \left(i_q^{2\omega_0} v_d^{ref} - i_d^{2\omega_0} v_q^{ref} \right), \\
\frac{dv_d^{2\omega_0}}{dt} &= 2c_7 i_d^{2\omega_0} + 2\omega_0 v_q^{2\omega_0} - c_8 \left(i_d v_d^{ref} - i_q v_q^{ref} \right). \\
\frac{dv_q^{2\omega_0}}{dt} &= 2c_7 i_q^{2\omega_0} - 2\omega_0 v_d^{2\omega_0} - c_8 \left(i_q v_d^{ref} + i_d v_q^{ref} \right),
\end{aligned} \tag{2.6}$$

The coefficients c in (2.6) are shown in

$$\begin{aligned}
& c_1 = \frac{R_{arm}}{L_{arm}}, \quad c_2 = \frac{3}{L_{arm}}, \quad c_3 = \frac{c_2}{12\tilde{V}_{dc}}, \quad c_4 = \frac{2R_0 + R_{arm}}{2L_0 + L_{arm}}, \\
& c_5 = \frac{1}{2L_0 + L_{arm}}, \quad c_6 = \frac{c_5}{\tilde{V}_{dc}}, \quad c_7 = \frac{N}{4C_{SM}}, \quad c_8 = \frac{c_7}{2\tilde{V}_{dc}}.
\end{aligned} \tag{2.7}$$

Rewriting (2.6) into the standard state-space description and it has

$$\frac{d\boldsymbol{x}_1}{dt} = \boldsymbol{A}_{10} \boldsymbol{x}_1 + g\left(\boldsymbol{x}_1\right) \boldsymbol{u}_1, \tag{2.8}$$

where

$$\begin{aligned}
\boldsymbol{x}_1^T &= \left[i_{dc}, i_d, i_q, i_d^{2\omega_0}, i_q^{2\omega_0}, v^{dc}, v_d^{\omega_0}, v_q^{\omega_0}, v_d^{2\omega_0}, v_q^{2\omega_0} \right], \\
\boldsymbol{u}_1^T &= \left[v_{dc}, v_d^{ref}, v_q^{ref} \right].
\end{aligned} \tag{2.9}$$

2.2 Modeling of *dq* Controller

The classical dq control scheme of MMC [18] is shown in Fig. 2.3. Since there are 4 proportional-integral (PI) elements in *dq* controller, the particular state variables δP, δQ, δi_d, δi_q of all PI elements and their associated control parameters are notated in Fig. 2.3.

The active and reactive power calculation of MMC ac-side in the *dq* reference frame is given by (2.10).

$$P=\frac{3}{2}\left(v_d i_d+v_q i_q\right),\ \ Q=\frac{3}{2}\left(v_q i_d-v_d i_q\right). \tag{2.10}$$

Therefore, based on the controller diagram shown in Fig. 2.3, the model of dq controller is derived as (2.11).

$$\begin{aligned}
&\frac{d\delta i_d}{dt}=k_i^P\left[\bar{k}_p^P\left(P_{ref}-\frac{3}{2}v_d i_d-\frac{3}{2}v_q i_q\right)+\delta P-i_d\right],\\
&\frac{d\delta i_q}{dt}=-k_i^Q\left[\bar{k}_p^Q\left(Q_{ref}-\frac{3}{2}v_q i_d+\frac{3}{2}v_d i_q\right)+\delta Q-i_q\right],\\
&\frac{d\delta P}{dt}=\bar{k}_i^P\left(P_{ref}-\frac{3}{2}v_d i_d-\frac{3}{2}v_q i_q\right),\\
&\frac{d\delta Q}{dt}=\bar{k}_i^Q\left(Q_{ref}-\frac{3}{2}v_q i_d+\frac{3}{2}v_d i_q\right),\\
&v_d^{ref}=k_p^P\left[\bar{k}_p^P\left(P_{ref}-\frac{3}{2}v_d i_d-\frac{3}{2}v_q i_q\right)+\delta P-i_d\right]+\delta i_d+v_d-\omega_0\left(\frac{1}{2}L_{arm}+L_0\right)i_q,\\
&v_q^{ref}=k_p^Q\left[\bar{k}_p^Q\left(Q_{ref}-\frac{3}{2}v_q i_d+\frac{3}{2}v_d i_q\right)+\delta Q-i_q\right]+\delta i_q+v_q+\omega_0\left(\frac{1}{2}L_{arm}+L_0\right)i_d.
\end{aligned} \tag{2.11}$$

Rewriting (2.11) into the standard state-space description and it has

$$\begin{aligned}
&\frac{d\boldsymbol{x}_2}{dt}=\boldsymbol{A}_2\boldsymbol{x}_2+\boldsymbol{B}_2\boldsymbol{u}_2,\\
&\boldsymbol{y}_2=\boldsymbol{C}_2\boldsymbol{x}_2+\boldsymbol{D}_2\boldsymbol{u}_2,
\end{aligned} \tag{2.12}$$

where

$$\boldsymbol{x}_2^T=\left[\delta i_d,\delta i_q,\delta P,\delta Q\right],\ \ \boldsymbol{u}_2^T=\left[P_{ref},Q_{ref},i_d,i_q\right],\ \ \boldsymbol{y}_2^T=\left[v_d^{ref},v_q^{ref}\right]. \tag{2.13}$$

On the other side, the droop control for the MMC active power reference is given by

$$P_{ref}=-k\left(v_{dc\_ref}-v_{dc}\right)+P_0. \tag{2.14}$$

where k, v_{dc_ref} and P_0 are the parameters of droop control.

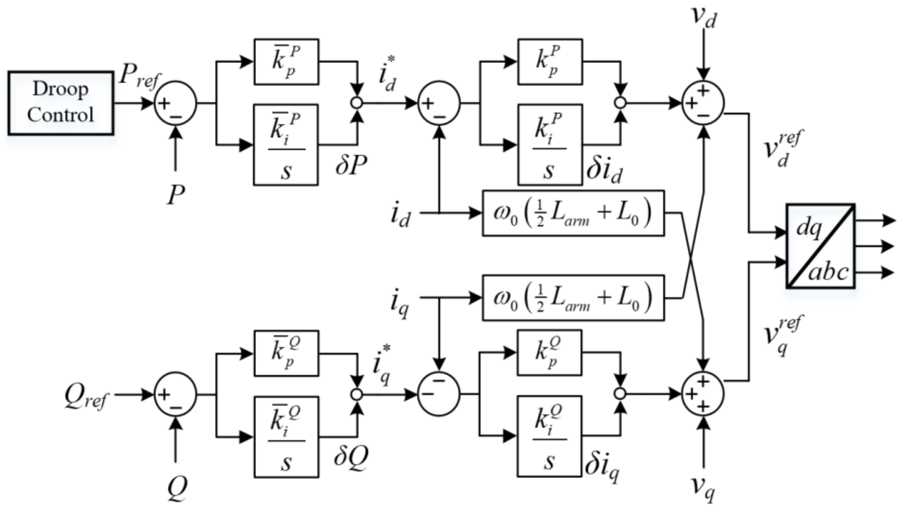

Figure 2.3 The *dq* control of the MMC.

2.3 Modeling of DC Network

The schematic diagram of a general MTDC system with n_{MMC} MMCs, n_{line} dc overhead transmission lines, and n_{node} network nodes is shown in Fig. 2.4, where the model of transmission line is the T equivalent circuit. R_{Tm}, L_{Tm} and C_{Tm} are the resistance, inductance, and capacitance of the T circuit, respectively. m is the index of the dc transmission lines, v_{Tm} is the voltage of the middle point of the T circuit. $i_{\zeta m}$ and $i_{\gamma m}$ are the terminal currents, respectively. $v_{\zeta m}$ and $v_{\gamma m}$ are the terminal voltages, respectively. Two terminal sets are defined as ζ and γ shown in the subscript. If the current flows out of the transmission line, this terminal will belong to the set γ. Otherwise, the terminal will belong to the set ζ with opposite current direction.

Two study systems, i.e., 4-terminal and 14-terminal MMC-MTDC systems are expressed in Figs. 2.5 and 2.6, respectively. The 4-terminal MMC-MTDC system comes from reference [14]. The 14-terminal MMC-MTDC system is the modification of the IEEE 14-bus ac system by changing ac lines to dc lines and connecting one MMC station to each bus [19]. The MMC stations integrated to the Buses 2 and 3 in the 4-terminal MTDC system, and Buses 1, 2, 3, 6, and 8 in the 14-terminal MTDC system operate with the droop controllers. The rest MMC stations in the both MTDC systems operate in the fixed power control mode. Since the topology of the dc network is discrepant, the modeling method based on the oriented edge-node incidence matrix [20] of the graph theory is introduced.

At first, the definition of the oriented edge-node incidence matrix will be elaborated. For the dc network, the size of the edge-node matrix notated as $\boldsymbol{J}$ is $n_{line} \times n_{node}$. Matrix $\boldsymbol{J}$ only contains the elements -1, 1, and 0. These elements are utilized to represent the direction of the dc-line current. If the current of m^{th} dc transmission line connected with nodes ζm and γm flows from ζm to γm, the corresponding elements of $\boldsymbol{J}_{(m,\zeta m)}$ and $\boldsymbol{J}_{(m,\gamma m)}$ will be 1 and -1, respectively. If there is no transmission line connected with two nodes, the corresponding elements will be 0.

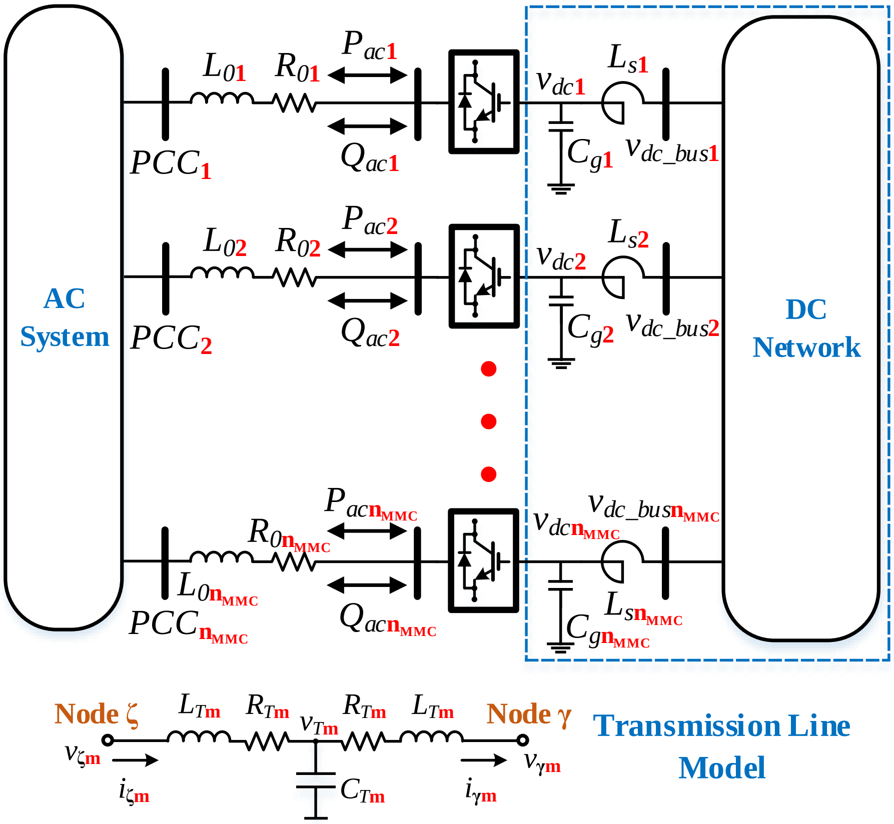

Figure 2.4 The schematic diagram of a general MTDC system.

To conveniently derive the dc network model, two auxiliary matrices $\boldsymbol{J}_1$ and $\boldsymbol{J}_2$ are defined. $\boldsymbol{J}_1$ contains all positive elements of $\boldsymbol{J}$. $-\boldsymbol{J}_2$ contains all negative elements of $\boldsymbol{J}$. And it has $\boldsymbol{J} = \boldsymbol{J}_1 - \boldsymbol{J}_2$.

For instance, the matrices $\boldsymbol{J}$, $\boldsymbol{J}_1$, and $\boldsymbol{J}_2$ of the 4-terminal MTDC system are given by (2.15).

$$\boldsymbol{J} = \begin{bmatrix} -1 & 1 & 0 & 0 \\ -1 & 0 & 1 & 0 \\ 0 & 1 & 0 & -1 \\ 0 & 0 & 1 & -1 \end{bmatrix}, \quad \boldsymbol{J}_1 = \begin{bmatrix} 0 & 1 & 0 & 0 \\ 0 & 0 & 1 & 0 \\ 0 & 1 & 0 & 0 \\ 0 & 0 & 1 & 0 \end{bmatrix}, \quad \boldsymbol{J}_2 = \begin{bmatrix} 1 & 0 & 0 & 0 \\ 1 & 0 & 0 & 0 \\ 0 & 1 & 0 & 1 \\ 0 & 0 & 0 & 1 \end{bmatrix}. \tag{2.15}$$

Therefore, regarding the model of the dc overhead transmission line as a two-port small network and the inner structure of which is ignored, the terminal variables for further constructing the simultaneous system are express as (2.16).

$$\boldsymbol{v}_{[\vec{\zeta}]} = \boldsymbol{J}_1 \boldsymbol{v}_{[\overrightarrow{dc\_bus}]}, \quad \boldsymbol{v}_{[\vec{\gamma}]} = \boldsymbol{J}_2 \boldsymbol{v}_{[\overrightarrow{dc\_bus}]}, \quad \boldsymbol{i}_{[\overrightarrow{dc\_bus}]} = -\boldsymbol{J}_1^T \boldsymbol{i}_{[\vec{\zeta}]} + \boldsymbol{J}_2^T \boldsymbol{i}_{[\vec{\gamma}]}. \tag{2.16}$$

where $\boldsymbol{v}_{[\vec{\zeta}]}$, $\boldsymbol{v}_{[\vec{\gamma}]}$ and $\boldsymbol{i}_{[\vec{\zeta}]}$, $\boldsymbol{i}_{[\vec{\gamma}]}$ are the terminal voltages and currents of all dc transmission line in the dc network by the notation shown in *Remark* as the vector form, respectively. $\boldsymbol{i}_{[\overline{dc\_bus}]}$ are the injecting currents of dc buses with the particular directions. $\boldsymbol{v}_{[\overline{dc\_bus}]}$ are the voltage of dc buses.

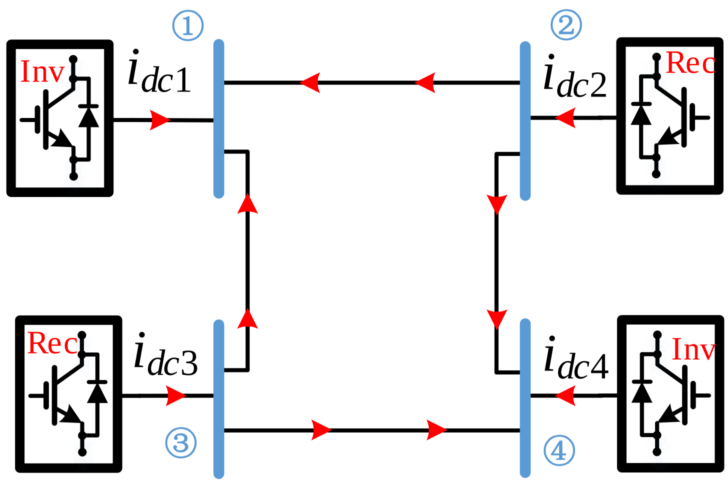

Figure 2.5 The 4-terminal MMC-MTDC study system.

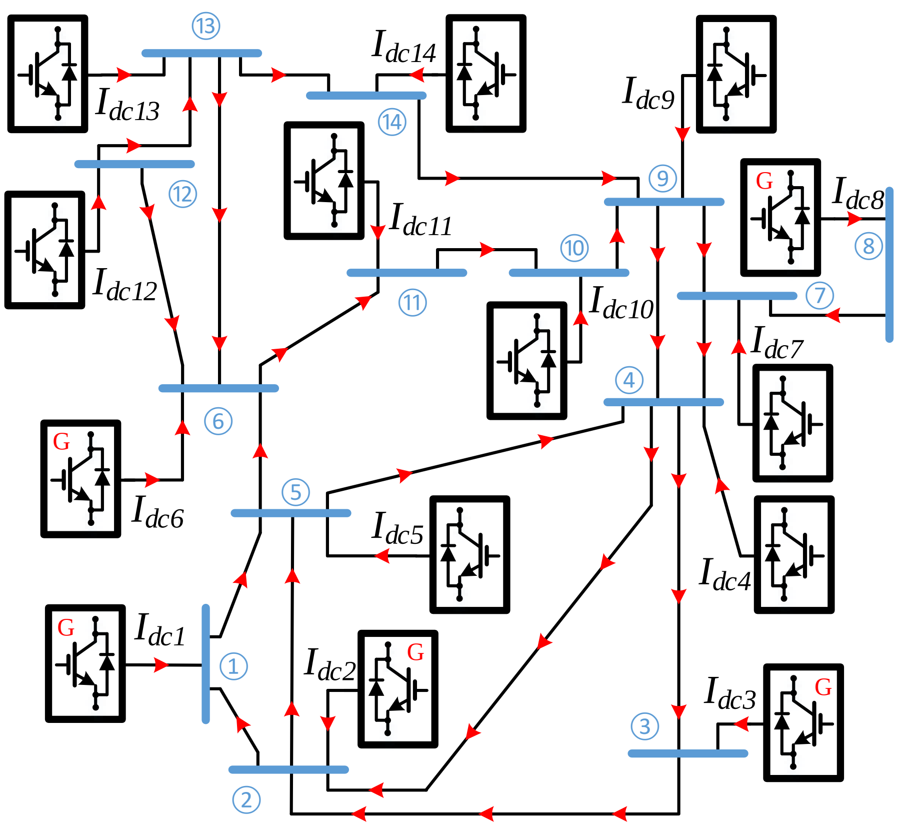

Figure 2.6 The 14-terminal MMC-MTDC study system.

Considering the smoothing reactor L_g and the grounding capacitor C_g in each MMC station, the circuit equations of the dc network containing all dc transmission lines described by the T equivalent circuit, by using the notation shown in Remark, are given by (2.17).

$$
\begin{aligned}
&\boldsymbol{L}_{\Lambda[s]}\frac{d}{dt}\boldsymbol{i}_{[\overrightarrow{dc\_bus}]}=\boldsymbol{v}_{[\overrightarrow{dc\_bus}]}-\boldsymbol{v}_{[\overrightarrow{dc}]},\\
&\boldsymbol{R}_{\Lambda[T]}\boldsymbol{i}_{[\vec{\zeta}]}+\boldsymbol{L}_{\Lambda[T]}\frac{d}{dt}\boldsymbol{i}_{[\vec{\zeta}]}=\boldsymbol{v}_{[\vec{\zeta}]}-\boldsymbol{v}_{[\vec{T}]},\\
&\boldsymbol{R}_{\Lambda[T]}\boldsymbol{i}_{[\vec{\gamma}]}+\boldsymbol{L}_{\Lambda[T]}\frac{d}{dt}\boldsymbol{i}_{[\vec{\gamma}]}=\boldsymbol{v}_{[\vec{T}]}-\boldsymbol{v}_{[\vec{\gamma}]},\\
&\boldsymbol{C}_{\Lambda[T]}\frac{d}{dt}\boldsymbol{v}_{[\vec{T}]}=\boldsymbol{i}_{[\vec{\zeta}]}-\boldsymbol{i}_{[\vec{\gamma}]},\\
&\boldsymbol{C}_{\Lambda[g]}\frac{d}{dt}\boldsymbol{v}_{[\overrightarrow{dc}]}=\boldsymbol{i}_{[\overrightarrow{dc\_bus}]}-\boldsymbol{i}_{[\overrightarrow{dc}]}.
\end{aligned}
\tag{2.17}
$$

If some nodes are interconnecting buses, the matrices $\boldsymbol{C}_{\Lambda[g]}$, $\boldsymbol{L}_{\Lambda[s]}$, and vector $\boldsymbol{i}_{[\overrightarrow{dc}]}$ will have 0 element at associated positions. Meanwhile, if some nodes are integrated with dc loads, then the associated value of vector $\boldsymbol{i}_{[\overrightarrow{dc}]}$ will be set as the load current. Now, eliminating $\boldsymbol{i}_{[\overrightarrow{dc\_bus}]}$ and $\boldsymbol{v}_{[\overrightarrow{dc\_bus}]}$, the model of the dc network is expressed in (2.18).

$$
\begin{aligned}
&\frac{d}{dt}\boldsymbol{i}_{[\vec{\zeta}]}=-\boldsymbol{b}_{10}^{-1}\left[\boldsymbol{R}_{\Lambda[T]}\boldsymbol{i}_{[\vec{\zeta}]}+\boldsymbol{b}_{11}\boldsymbol{i}_{[\vec{\gamma}]}-\boldsymbol{b}_{12}\boldsymbol{v}_{[\vec{T}]}-\boldsymbol{b}_{13}\boldsymbol{v}_{[\overrightarrow{dc}]}\right],\\
&\frac{d}{dt}\boldsymbol{i}_{[\vec{\gamma}]}=-\boldsymbol{b}_{20}^{-1}\left[\boldsymbol{b}_{21}\boldsymbol{i}_{[\vec{\zeta}]}+\boldsymbol{R}_{\Lambda[T]}\boldsymbol{i}_{[\vec{\gamma}]}-\boldsymbol{b}_{22}\boldsymbol{v}_{[\vec{T}]}-\boldsymbol{b}_{23}\boldsymbol{v}_{[\overrightarrow{dc}]}\right],\\
&\frac{d}{dt}\boldsymbol{v}_{[\vec{T}]}=\boldsymbol{C}_{\Lambda[T]}^{-1}\left[\boldsymbol{i}_{[\vec{\zeta}]}-\boldsymbol{i}_{[\vec{\gamma}]}\right],\\
&\frac{d}{dt}\boldsymbol{v}_{[\overrightarrow{dc}]}=\boldsymbol{C}_{\Lambda[g]}^{-1}\left[\boldsymbol{J}_1^T\boldsymbol{i}_{[\vec{\zeta}]}-\boldsymbol{J}_2^T\boldsymbol{i}_{[\vec{\gamma}]}+\boldsymbol{i}_{[\overrightarrow{dc}]}\right],
\end{aligned}
\tag{2.18}
$$

where the coefficients $\boldsymbol{b}$ are shown in (2.19) and $\boldsymbol{I}$ is the identity matrix.

$$
\begin{aligned}
\boldsymbol{b}_{10} &= \boldsymbol{L}_{\Lambda[T]} + \boldsymbol{J}_1 \boldsymbol{L}_{\Lambda[s]} \boldsymbol{J}_1^T - \boldsymbol{J}_1 \boldsymbol{L}_{\Lambda[s]} \boldsymbol{J}_2^T \left(\boldsymbol{L}_{\Lambda[T]} + \boldsymbol{J}_2 \boldsymbol{L}_{\Lambda[s]} \boldsymbol{J}_2^T \right)^{-1} \boldsymbol{J}_2 \boldsymbol{L}_{\Lambda[s]} \boldsymbol{J}_1^T, \\
\boldsymbol{b}_{11} &= \boldsymbol{J}_1 \boldsymbol{L}_{\Lambda[s]} \boldsymbol{J}_2^T \left(\boldsymbol{L}_{\Lambda[T]} + \boldsymbol{J}_2 \boldsymbol{L}_{\Lambda[s]} \boldsymbol{J}_2^T \right)^{-1}, \\
\boldsymbol{b}_{12} &= \boldsymbol{J}_1 \boldsymbol{L}_{\Lambda[s]} \boldsymbol{J}_2^T \left(\boldsymbol{L}_{\Lambda[T]} + \boldsymbol{J}_2 \boldsymbol{L}_{\Lambda[s]} \boldsymbol{J}_2^T \right)^{-1} - \boldsymbol{I}, \\
\boldsymbol{b}_{13} &= \boldsymbol{J}_1 - \boldsymbol{J}_1 \boldsymbol{L}_{\Lambda[s]} \boldsymbol{J}_2^T \left(\boldsymbol{L}_{\Lambda[T]} + \boldsymbol{J}_2 \boldsymbol{L}_{\Lambda[s]} \boldsymbol{J}_2^T \right)^{-1} \boldsymbol{J}_2, \\
\boldsymbol{b}_{20} &= \boldsymbol{L}_{\Lambda[T]} + \boldsymbol{J}_2 \boldsymbol{L}_{\Lambda[s]} \boldsymbol{J}_2^T - \boldsymbol{J}_2 \boldsymbol{L}_{\Lambda[s]} \boldsymbol{J}_1^T \left(\boldsymbol{L}_{\Lambda[T]} + \boldsymbol{J}_1 \boldsymbol{L}_{\Lambda[s]} \boldsymbol{J}_1^T \right)^{-1} \boldsymbol{J}_1 \boldsymbol{L}_{\Lambda[s]} \boldsymbol{J}_2^T, \\
\boldsymbol{b}_{21} &= \boldsymbol{J}_2 \boldsymbol{L}_{\Lambda[s]} \boldsymbol{J}_1^T \left(\boldsymbol{L}_{\Lambda[T]} + \boldsymbol{J}_1 \boldsymbol{L}_{\Lambda[s]} \boldsymbol{J}_1^T \right)^{-1}, \\
\boldsymbol{b}_{22} &= \boldsymbol{J}_2 \boldsymbol{L}_{\Lambda[s]} \boldsymbol{J}_1^T \left(\boldsymbol{L}_{\Lambda[T]} + \boldsymbol{J}_1 \boldsymbol{L}_{\Lambda[s]} \boldsymbol{J}_1^T \right)^{-1} - \boldsymbol{I}, \\
\boldsymbol{b}_{23} &= \boldsymbol{J}_2 - \boldsymbol{J}_2 \boldsymbol{L}_{\Lambda[s]} \boldsymbol{J}_1^T \left(\boldsymbol{L}_{\Lambda[T]} + \boldsymbol{J}_1 \boldsymbol{L}_{\Lambda[s]} \boldsymbol{J}_1^T \right)^{-1} \boldsymbol{J}_1,
\end{aligned}
\tag{2.19}
$$

Rewriting (2.18) into the standard state-space model:

$$
\frac{d}{dt} \boldsymbol{x}_{[\vec{3}]} = \boldsymbol{A}_{[3]} \boldsymbol{x}_{[\vec{3}]} + \boldsymbol{B}_{[3]} \boldsymbol{u}_{[\vec{3}]}, \tag{2.20}
$$

where,

$$
\boldsymbol{x}_{[\vec{3}]}^T = \left[\boldsymbol{i}_{[\vec{\zeta}]}, \boldsymbol{i}_{[\vec{\gamma}]}, \boldsymbol{v}_{[\vec{T}]}, \boldsymbol{v}_{[\overrightarrow{dc}]} \right], \quad \boldsymbol{u}_{[\vec{3}]}^T = \boldsymbol{i}_{[\overrightarrow{dc}]}. \tag{2.21}
$$

3. Modeling of MMC-MTDC System

According to the *Remark*, all MMCs in the MMC-MTDC system can be rewritten as a subsystem shown in

$$\frac{d}{dt}\boldsymbol{x}_{[\vec{1}]} = \boldsymbol{A}_{[1]}\boldsymbol{x}_{[\vec{1}]} + \boldsymbol{B}_{[1]}\boldsymbol{u}_{[\vec{1}]}, \tag{3.1}$$

where,

$$\begin{aligned}
\boldsymbol{x}_{[\vec{1}]}^{T} &= \left[\boldsymbol{i}_{[\vec{dc}]}, \boldsymbol{i}_{[\vec{d}]}, \boldsymbol{i}_{[\vec{q}]}, \boldsymbol{i}_{[\vec{d}]}^{2\omega_0}, \boldsymbol{i}_{[\vec{q}]}^{2\omega_0}, \boldsymbol{v}_{[\vec{\cdot}]}^{dc}, \boldsymbol{v}_{[\vec{d}]}^{\omega_0}, \boldsymbol{v}_{[\vec{q}]}^{\omega_0}, \boldsymbol{v}_{[\vec{d}]}^{2\omega_0}, \boldsymbol{v}_{[\vec{q}]}^{2\omega_0}\right], \\
\boldsymbol{u}_{[\vec{2}]}^{T} &= \left[\boldsymbol{v}_{[\vec{dc}]}, \boldsymbol{v}_{[\vec{d}]}^{ref}, \boldsymbol{v}_{[\vec{q}]}^{ref}\right].
\end{aligned} \tag{3.2}$$

The structure of $\boldsymbol{A}_{[1]}$ and $\boldsymbol{x}_{[\vec{1}]}$ can be found in Fig. 3.1. Each row and column of $\boldsymbol{A}_{[1]}$ has 10 submatrices, respectively, since the number of submatrices at each row and column relies on the order of MMC model $\boldsymbol{x}_1$. Submatrix $\boldsymbol{A}_{1[m,n]}$ is comprised of the elements at the m^{th} row and n^{th} column of $\boldsymbol{A}_{1(1)} \cdots \boldsymbol{A}_{1(n_{MMC})}$ of all n_{MMC} MMCs. Thus, $\boldsymbol{A}_{1(i)[m,n]}$ is the element at the m^{th} row and n^{th} column of $\boldsymbol{A}_{1(i)}$ of the i^{th} MMC small-signal model. If the number of MMCs modified, the size of submatrices will be easily adjusted.

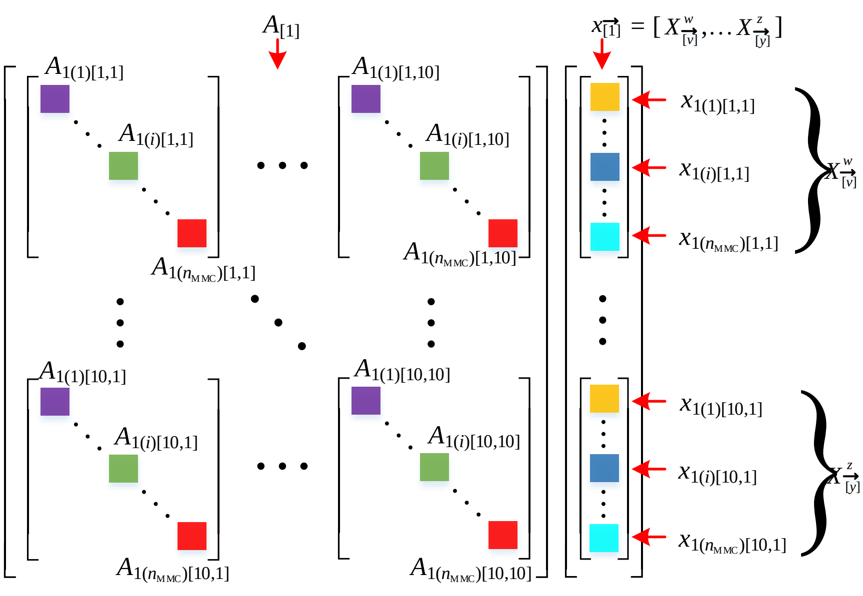

Figure 3.1 The structure of the matrices in subsystem.

The subsystems of all *dq* controllers can be combined and shown in

$$\begin{aligned}
\frac{d}{dt}\boldsymbol{x}_{[\vec{2}]} &= \boldsymbol{A}_{[2]}\boldsymbol{x}_{[\vec{2}]} + \boldsymbol{B}_{[2]}\boldsymbol{u}_{[\vec{2}]}, \\
\boldsymbol{y}_{[\vec{2}]} &= \boldsymbol{C}_{[2]}\boldsymbol{x}_{[\vec{2}]} + \boldsymbol{D}_{[2]}\boldsymbol{u}_{[\vec{2}]},
\end{aligned} \tag{3.3}$$

where,

$$\boldsymbol{x}_2^T=\left[\boldsymbol{\delta i}_{[\vec{d}]},\boldsymbol{\delta i}_{[\vec{q}]},\boldsymbol{\delta P}_{[\vec{\cdot}]},\boldsymbol{\delta Q}_{[\vec{\cdot}]}\right],\ \ \boldsymbol{u}_2^T=\left[\boldsymbol{P}_{[\overrightarrow{ref}]},\boldsymbol{Q}_{[\overrightarrow{ref}]},\boldsymbol{i}_{[\vec{d}]},\boldsymbol{i}_{[\vec{q}]}\right],\ \ \boldsymbol{y}_2^T=\left[\boldsymbol{v}_{[\vec{d}]}^{ref},\boldsymbol{v}_{[\vec{q}]}^{ref}\right]. \tag{3.4}$$

The model of active power reference is given by (3.5) including all droop controllers' outputs and the fixed power references.

$$\boldsymbol{P}_{[\overrightarrow{ref}]}=\boldsymbol{k}_{\Lambda}\boldsymbol{v}_{[\overrightarrow{dc}]}+\boldsymbol{P}_{[\vec{0}]}, \tag{3.5}$$

where $\boldsymbol{k}_{\Lambda}$ indicates the diagonal matrix which consists of the droop slope k of all MMCs operating with droop controllers. For the MMCs without droop control, the corresponding diagonal element in $\boldsymbol{k}_{\Lambda}$ will be zero. Meanwhile, all constants shown in droop control law (2.14) are combined to one constant shown in $\boldsymbol{P}_{[\vec{0}]}$. And the power references of the fixed power control mode are also given in $\boldsymbol{P}_{[\vec{0}]}$.

The subsystems shown in (2.8) have couplings in their state variables and inputs with each other. Therefore, an autonomous system will be derived for establishing the complete model of the MMC-MTDC system by combining these individually developed sub-systems and eliminating the couplings.

The relationship between $\boldsymbol{u}_{[\vec{3}]}$ and $\boldsymbol{x}_{[\vec{1}]}$ is shown as

$$\boldsymbol{u}_{[\vec{3}]}=\boldsymbol{i}_{[\overrightarrow{dc}]}=[\boldsymbol{I}\quad\underbrace{\boldsymbol{0}\quad\boldsymbol{0}\quad\cdots\quad\boldsymbol{0}}_{n_{node}\times 9n_{node}}]\boldsymbol{x}_{[\vec{1}]}=\boldsymbol{G}_3\boldsymbol{x}_{[\vec{1}]}, \tag{3.6}$$

where 0 and I are zero and identity matrix, respectively. In addition, $\boldsymbol{u}_{[\vec{2}]}$ can be rewritten as

$$\begin{aligned}\boldsymbol{u}_{[\vec{2}]}&=\begin{bmatrix}\boldsymbol{I}\\\boldsymbol{0}\\\boldsymbol{0}\\\boldsymbol{0}\end{bmatrix}\boldsymbol{P}_{[\overrightarrow{ref}]}+\begin{bmatrix}\boldsymbol{0}\\\boldsymbol{I}\\\boldsymbol{0}\\\boldsymbol{0}\end{bmatrix}\boldsymbol{Q}_{[\overrightarrow{ref}]}+\begin{bmatrix}\boldsymbol{0}&\boldsymbol{0}\\\boldsymbol{0}&\boldsymbol{0}\\\boldsymbol{I}&\boldsymbol{0}\\\boldsymbol{0}&\boldsymbol{I}\end{bmatrix}\begin{bmatrix}\boldsymbol{i}_{[\vec{d}]}\\\boldsymbol{i}_{[\vec{q}]}\end{bmatrix}\\&=\boldsymbol{G}_{21}\boldsymbol{P}_{[\overrightarrow{ref}]}+\boldsymbol{G}_{22}\boldsymbol{Q}_{[\overrightarrow{ref}]}+\boldsymbol{G}_{23}\begin{bmatrix}\boldsymbol{i}_{[\vec{d}]}\\\boldsymbol{i}_{[\vec{q}]}\end{bmatrix}.\end{aligned} \tag{3.7}$$

On the other hand, it has

$$\begin{aligned}\begin{bmatrix}\boldsymbol{i}_{[\vec{d}]}\\\boldsymbol{i}_{[\vec{q}]}\end{bmatrix}&=\underbrace{\begin{bmatrix}\boldsymbol{0}&\boldsymbol{I}&\boldsymbol{0}&\cdots&\boldsymbol{0}\\\boldsymbol{0}&\boldsymbol{0}&\boldsymbol{I}&\cdots&\boldsymbol{0}\end{bmatrix}}_{2n_{node}\times 10n_{node}}\boldsymbol{x}_{[\vec{1}]}=\boldsymbol{G}_{s1}\boldsymbol{x}_{[\vec{1}]},\\\boldsymbol{v}_{[\overrightarrow{dc}]}&=\begin{bmatrix}\boldsymbol{0}&\boldsymbol{0}&\boldsymbol{0}&\boldsymbol{I}\end{bmatrix}\boldsymbol{x}_{[\vec{3}]}=\boldsymbol{G}_{s2}\boldsymbol{x}_{[\vec{3}]}.\end{aligned} \tag{3.8}$$

Involving (3.5) and (3.8) into (3.7), $\boldsymbol{u}_{[\vec{2}]}$ will be given by

$$\boldsymbol{u}_{[\vec{2}]} = \boldsymbol{G}_{21}\boldsymbol{k}_{\Lambda}\boldsymbol{G}_{s2}\boldsymbol{x}_{[\vec{3}]} + \boldsymbol{G}_{21}\boldsymbol{P}_{[\vec{0}]} + \boldsymbol{G}_{22}\boldsymbol{Q}_{[\overrightarrow{ref}]} + \boldsymbol{G}_{23}\boldsymbol{G}_{s1}\boldsymbol{x}_{[\vec{1}]}. \tag{3.9}$$

Moreover, substituting(3.3), (3.8), and (3.9) into $\boldsymbol{u}_{[\vec{1}]}$ and it has

$$\begin{aligned}
\boldsymbol{u}_{[\vec{1}]} &= \begin{bmatrix} \boldsymbol{I} \\ \mathbf{0} \\ \mathbf{0} \end{bmatrix} \boldsymbol{v}_{[\overrightarrow{dc}]} + \begin{bmatrix} \mathbf{0} & \mathbf{0} \\ \boldsymbol{I} & \mathbf{0} \\ \mathbf{0} & \boldsymbol{I} \end{bmatrix} \begin{bmatrix} \boldsymbol{v}_{[\vec{d}]}^{ref} \\ \boldsymbol{v}_{[\vec{q}]}^{ref} \end{bmatrix} \\
&= \boldsymbol{G}_{11}\boldsymbol{G}_{s2}\boldsymbol{x}_{[\vec{3}]} + \boldsymbol{G}_{12}\boldsymbol{y}_{[\vec{2}]} \\
&= \boldsymbol{G}_{12}\boldsymbol{D}_{[2]}\boldsymbol{G}_{23}\boldsymbol{G}_{s1}\boldsymbol{x}_{[\vec{1}]} + \boldsymbol{G}_{12}\boldsymbol{C}_{[2]}\boldsymbol{x}_{[\vec{2}]} + \left(\boldsymbol{G}_{11}\boldsymbol{G}_{s2} + \boldsymbol{G}_{12}\boldsymbol{D}_{[2]}\boldsymbol{G}_{21}\boldsymbol{k}_{\Lambda}\boldsymbol{G}_{s2}\right)\boldsymbol{x}_{[\vec{3}]} \\
&\quad + \boldsymbol{G}_{12}\boldsymbol{D}_{[2]}\boldsymbol{G}_{21}\boldsymbol{P}_{[\vec{0}]} + \boldsymbol{G}_{12}\boldsymbol{D}_{[2]}\boldsymbol{G}_{22}\boldsymbol{Q}_{[\overrightarrow{ref}]}.
\end{aligned} \tag{3.10}$$

Finally, involving (3.6), (3.9), (3.10) into (2.20), (3.1), (3.10), the small-signal model of the whole MMC-based MTDC system as an autonomous system is given by

$$\frac{d}{dt}\begin{bmatrix} \boldsymbol{x}_{[\vec{1}]} \\ \boldsymbol{x}_{[\vec{2}]} \\ \boldsymbol{x}_{[\vec{3}]} \end{bmatrix} = \boldsymbol{A}_s \begin{bmatrix} \boldsymbol{x}_{[\vec{1}]} \\ \boldsymbol{x}_{[\vec{2}]} \\ \boldsymbol{x}_{[\vec{3}]} \end{bmatrix} + \boldsymbol{B}_s \begin{bmatrix} \boldsymbol{P}_{[\vec{0}]} \\ \boldsymbol{Q}_{[\overrightarrow{ref}]} \end{bmatrix}, \tag{3.11}$$

where,

$$\begin{aligned}
\boldsymbol{A}_s &= \begin{bmatrix} \boldsymbol{A}_{[1]} + \boldsymbol{B}_{[1]}\boldsymbol{G}_{12}\boldsymbol{D}_{[2]}\boldsymbol{G}_{23}\boldsymbol{G}_{s1} & \boldsymbol{B}_{[1]}\boldsymbol{G}_{12}\boldsymbol{C}_{[2]} & \boldsymbol{B}_{[1]}\left(\boldsymbol{G}_{11}\boldsymbol{G}_{s2} + \boldsymbol{G}_{12}\boldsymbol{D}_{[2]}\boldsymbol{G}_{21}\boldsymbol{k}_{\Lambda}\boldsymbol{G}_{s2}\right) \\ \boldsymbol{B}_{[2]}\boldsymbol{G}_{23}\boldsymbol{G}_{s1} & \boldsymbol{A}_{[2]} & \boldsymbol{B}_{[2]}\boldsymbol{G}_{21}\boldsymbol{k}_{\Lambda}\boldsymbol{G}_{s2} \\ \boldsymbol{B}_{[3]}\boldsymbol{G}_{3} & \mathbf{0} & \boldsymbol{A}_{[3]} \end{bmatrix} \\
\boldsymbol{B}_s &= \begin{bmatrix} \boldsymbol{B}_{[1]}\boldsymbol{G}_{12}\boldsymbol{D}_{[2]}\boldsymbol{G}_{21} & \boldsymbol{B}_{[1]}\boldsymbol{G}_{12}\boldsymbol{D}_{[2]}\boldsymbol{G}_{22} \\ \boldsymbol{B}_{[2]}\boldsymbol{G}_{21} & \boldsymbol{B}_{[2]}\boldsymbol{G}_{22} \\ \mathbf{0} & \mathbf{0} \end{bmatrix}
\end{aligned} \tag{3.12}$$

According to (3.11), the simulation can be achieved by iteratively calculating the state-space model with Runge-Kutta method.

4. Simulation Verification

The developed model of MMC and the associated MMC-MTDC system based on (3.11) will be verified. Two study systems, i.e., a 4-terminal and 14-terminal MMC-MTDC systems shown in Figs. 2.5 and 2.6 are employed. Based on the perturbation of MMC state variable and the active power reference jumping, the dynamic responses show the validation of all developed model compared with the EMT simulation in PSCAD/EMTDC. The system parameters of both study systems are listed in Tab. Table 4.1

Table 4.1 Electric Parameters of the Two Study Systems

MMC	**Value**	**DC Grid**	**Value**
SM Capacitance C_{SM} [mF]	20 (Droop Control)	Resistance [Ω/km]	0.01273
	25 (Fixed Power)	Inductance [mH/km]	0.9337
Arm Inductance L_{arm} [mH]	0.16 (Droop Control)	Capacitance [μF/km]	0.01274
	0.1 (Fixed Power)	Smoothing Reactor L_s [mH]	200
Arm Resistance R_{arm} [Ω]	2.175 (Droop Control)	Grounding Capacitor C_g [μF]	1
	1.815 (Fixed Power)	PCC Resistance R_0 [Ω]	1
Voltage Level	435 (Droop Control)	PCC Inductance L_0 [mH]	0
	363 (Fixed Power)	DC Voltage [kV]	±500

4.1 Dynamic Responses of MMC

Two cases of MMC dynamic responses in the 4-terminal and 14-terminal MTDC system are conducted, respectively. In the first case, the state variable i_{dc} of the MMC connected to Bus 1 of the 4-terminal MTDC system is perturbed when t = 8 s. Before t = 8 s, all state variables stay at the origin except v^{dc}. The magnitude of perturbation is 3 kA coming from a current source. The parameters of droop controllers are k2 = 25 and k3 = 30. Then, the perturbed dynamic responses of the MMC voltage and current components are exhibited in Figs. 4.1 and 4.2, respectively.

In the second case, a step change on the active power command P_{ref} of the Bus-4 MMC station in the 14-terminal MTDC system occurs at t = 7 s. The step change adjusts P_{ref} from 120 MW to 290 MW. The parameters of droop controllers are k_1 = 10, k_2 = 15, k_3 = 18, k_6 = 20, and k_8 = 24. Then, the dynamic responses of the MMC voltage and current components are exhibited in Figs. 4.3 and 4.4. In addition, the dynamic response of phase *a* upper arm of Bus-4 MMC station is shown in Fig. 4.5.

Furthermore, the EMT simulation in PSCAD/EMTDC and the calculation of nonlinear differential equations in MATLAB are compared to verify the accuracy and the validation of the developed model of MMC and the MMC-based MTDC system in all exhibited figures. According to the comparison, the errors between the simulations and calculations are extremely small and negligible, which validates the accuracy and correctness of the developed model.

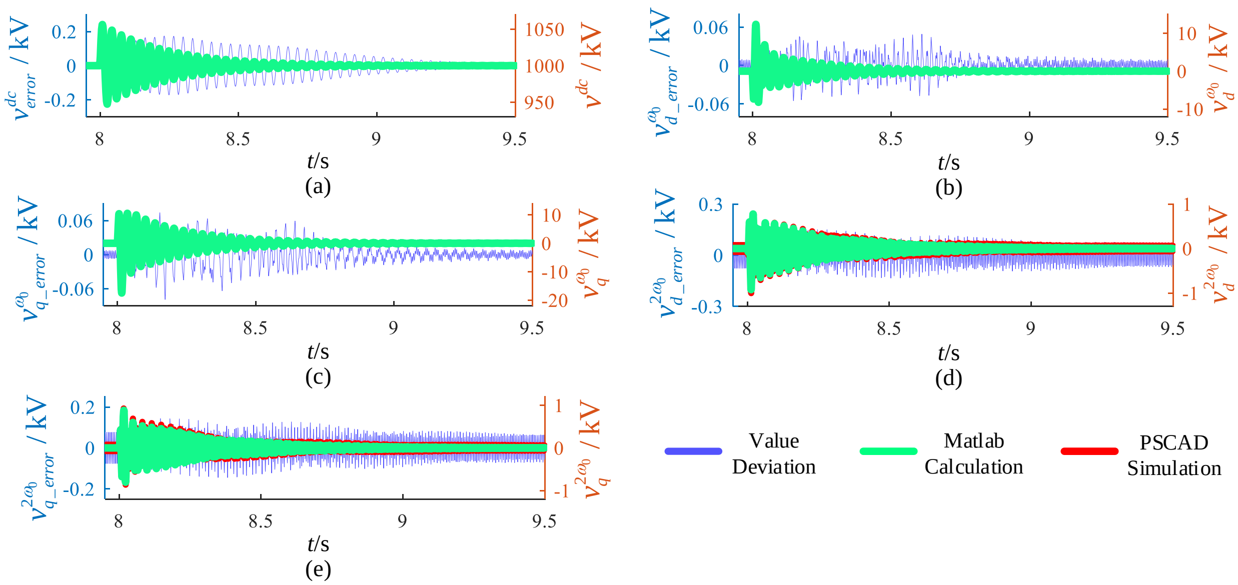

Figure 4.1 The voltage dynamic responses of the MMC connected to Bus-1 in 4-terminal MMC-MTDC system and numerical comparison between PSCAD/EMTDC simulation and MATLAB solution. (a) v_{dc}, (b) $v_d^{\omega_0}$, (c) $v_q^{\omega_0}$, (d) $v_d^{2\omega_0}$, and (e) $v_q^{2\omega_0}$.

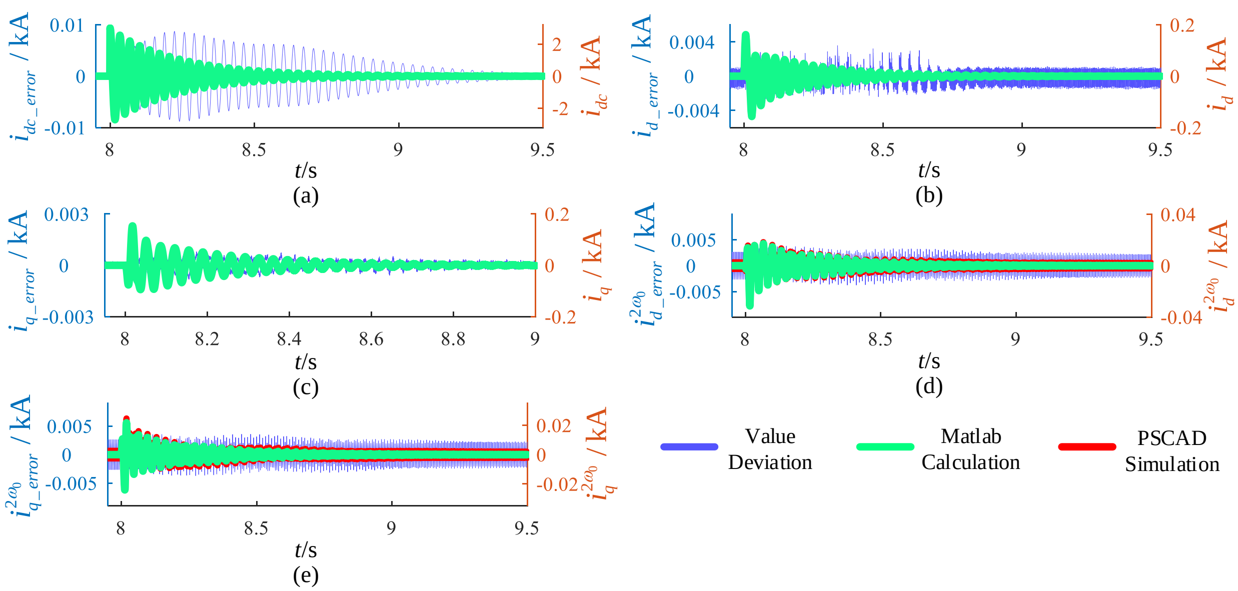

Figure 4.2 The current dynamic responses of the MMC connected to Bus-1 in 4-terminal MMC-MTDC system and numerical comparison between PSCAD/EMTDC simulation and MATLAB solution. (a) i_{dc}, (b) i_d, (c) i_q, (d) $i_d^{2\omega_0}$, and (e) $i_q^{2\omega_0}$.

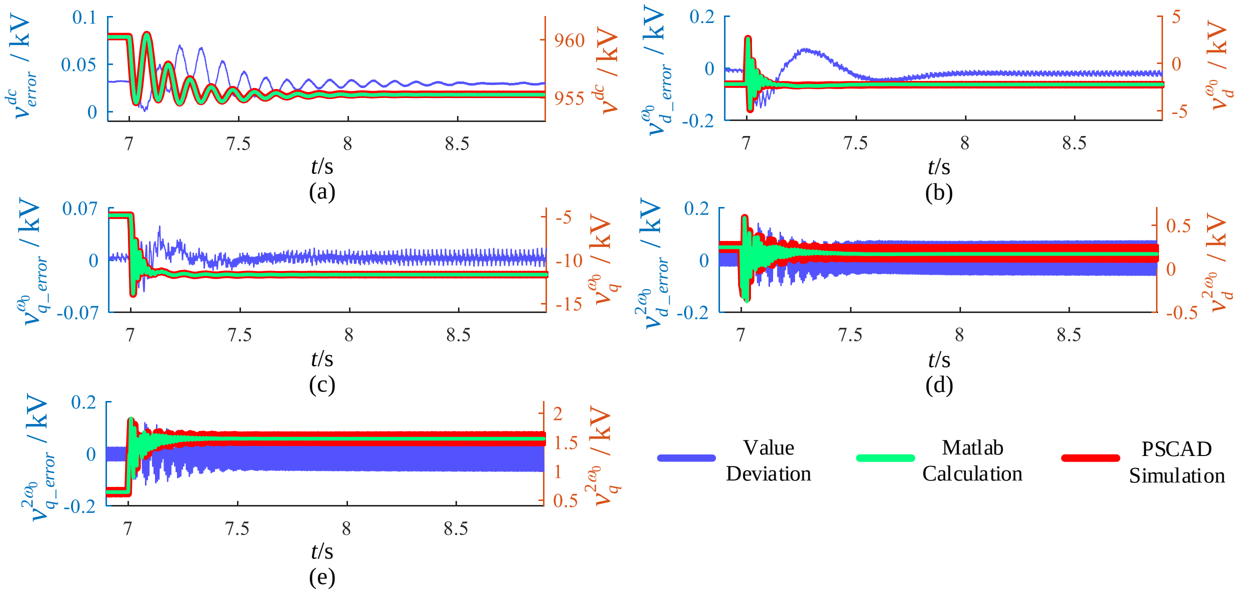

Figure 4.3 The voltage dynamic responses of the MMC connected to Bus-4 in 14-terminal MMC-MTDC system and numerical comparison between PSCAD/EMTDC simulation and MATLAB solution. (a) v_{dc}, (b) $v_d^{\omega_0}$, (c) $v_q^{\omega_0}$, (d) $v_d^{2\omega_0}$, and (e) $v_q^{2\omega_0}$.

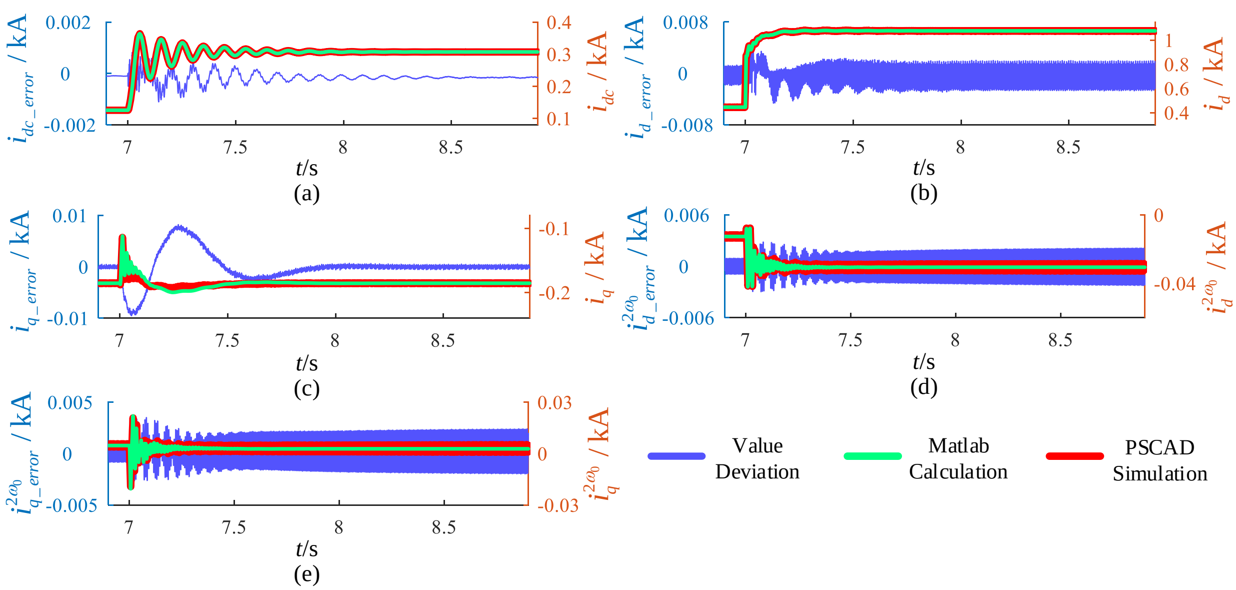

Figure 4.4 The current dynamic responses of the MMC connected to Bus-4 in 14-terminal MMC-MTDC system and numerical comparison between PSCAD/EMTDC simulation and MATLAB solution. (a) i_{dc}, (b) i_d, (c) i_q, (d) $i_d^{2\omega_0}$, and (e) $i_q^{2\omega_0}$.

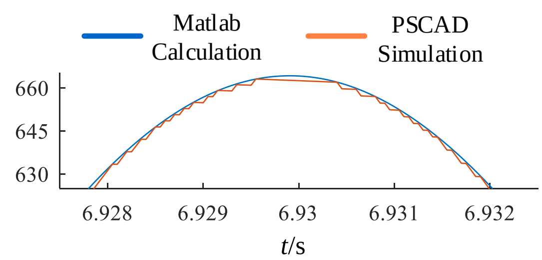

Figure 4.5 The voltage dynamic response of the MMC connected to Bus-4 in 14-terminal MMC-MTDC system at steady-state conditions and numerical comparison between PSCAD/EMTDC simulation and MATLAB solution.

4.2 Dynamic Responses of MTDC System

Two cases of MMC-MTDC system dynamics in the 4-terminal and 14-terminal MTDC systems are conducted. In the first case, a step change on the active power command P_{ref} of the Bus-1 MMC station in the 4-terminal MTDC system occurs at t =7 s. The step change adjusts P_{ref} from 120 MW to 190 MW. The parameters of droop controllers are k_2 = 25 and k_3 = 10. Then, the dynamic responses of the measured MMC voltages and active powers on dc-side are exhibited in Figs. 4.6 and 4.7, respectively.

In the second case, a step change on the active power reference P_{ref} of the Bus-4 MMC station in the 14-terminal MTDC system occurs at t =7 s. The step change adjusts P_{ref} from 120 MW to 290 MW. The parameters of droop controllers are k_1 = 10, k_2 = 15, k_3 = 18, k_6 = 20, and k_8 = 24. Then, the dynamic responses of the measured MMC voltages and active powers on dc-side are exhibited in Figs. 4.8 and 4.9, respectively.

The EMT simulation in PSCAD/EMTDC and the calculation of nonlinear differential equations in MATLAB are compared to verify the accuracy and the validation of the developed model of MMC and the MMC-based MTDC system in these figures. According to the numerical comparison, the errors between the simulations and calculations are extremely small and negligible, which validates the accuracy and correctness of the developed model.

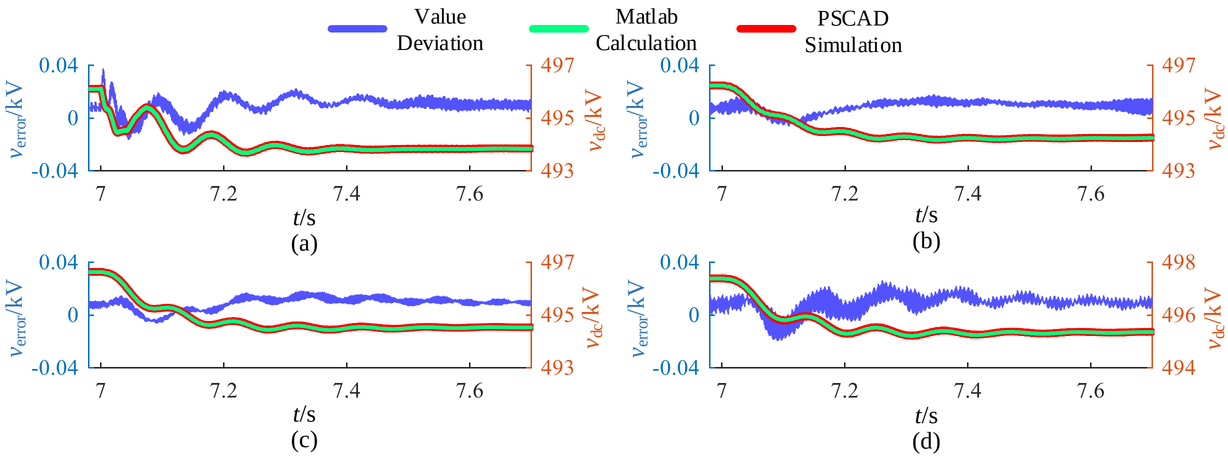

Figure 4.6 The dc voltage dynamic responses of the associated buses in 4-terminal MMC-MTDC system and numerical comparison between PSCAD/EMTDC simulation and MATLAB solution. (a) Bus-1, (b) Bus-2, (c) Bus-3, and (d) Bus-4.

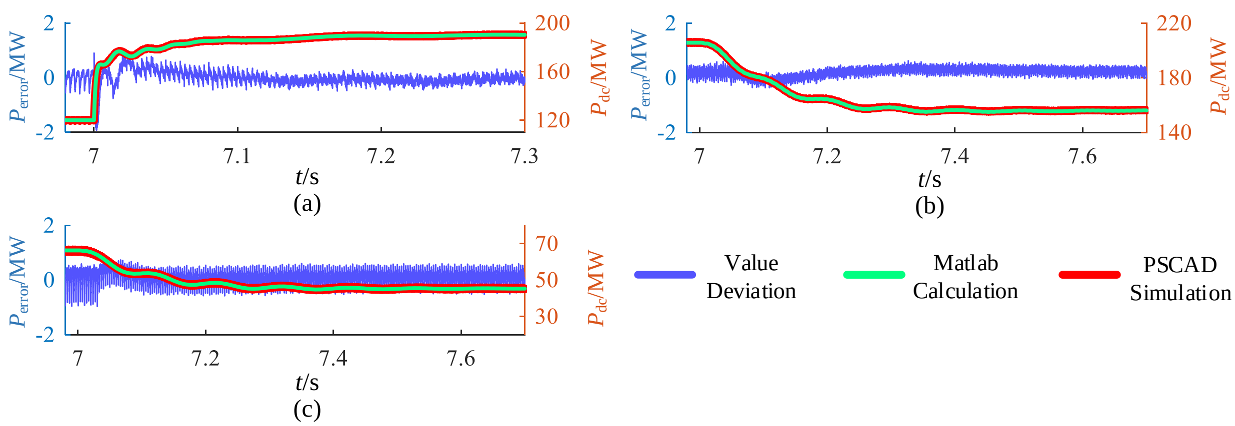

Figure 4.7 The dc active power dynamic responses of the associated buses in 4-terminal MMC-MTDC system and numerical comparison between PSCAD/EMTDC simulation and MATLAB solution. (a) Bus-1, (b) Bus-2, and (c) Bus-3.

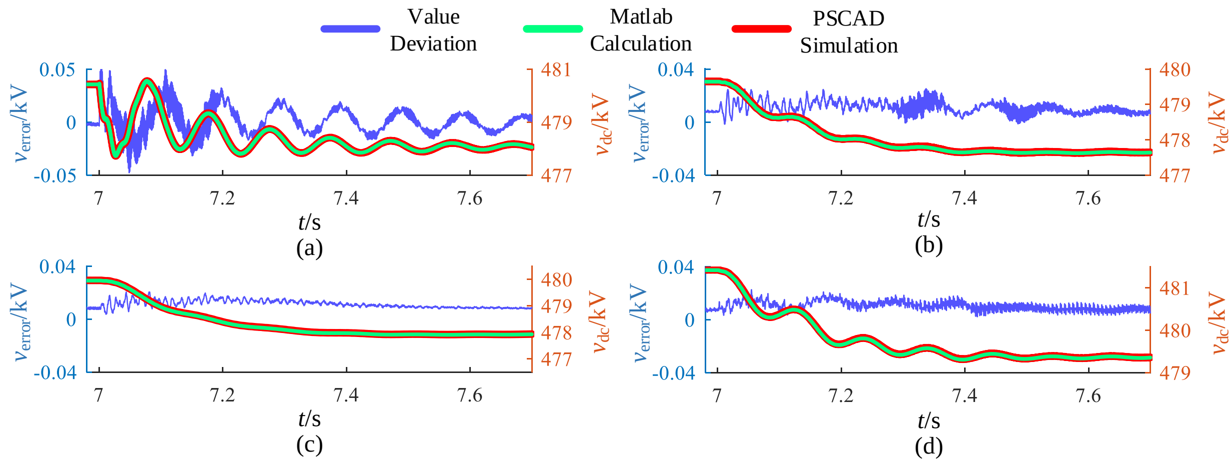

Figure 4.8 The dc voltage dynamic responses of the associated buses in 14-terminal MMC-MTDC system and numerical comparison between PSCAD/EMTDC simulation and MATLAB solution. (a) Bus-4, (b) Bus-1, (c) Bus-6, and (d) Bus-8.

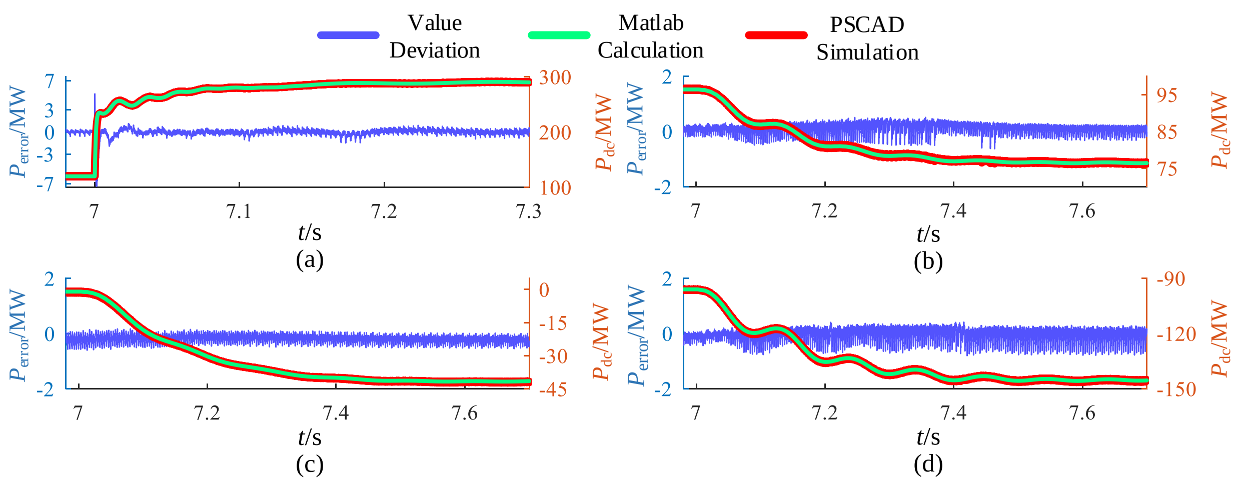

Figure 4.9 The dc active power dynamic responses of the associated buses in 14-terminal MMC-MTDC system and numerical comparison between PSCAD/EMTDC simulation and MATLAB solution. (a) Bus-4, (b) Bus-1, (c) Bus-6, and (d) Bus-8.

5. Conclusions

A generalized model of the MMC-MTDC system is developed. As a systematic modeling method, this model is applicable to the MMC-MTDC system with arbitrary number of MMCs with dq controllers due to a uniform matrix arrangement, arbitrary topology of dc network due to the application of edge-node incidence matrix, and arbitrary dc transmission model due to the description of terminal variables.

References

[1] AMa, Junchao, et al. "Transmission loss optimization-based optimal power flow strategy by hierarchical control for DC microgrids." *IEEE Transactions on Power Electronics* 32.3 (2016): 1952-1963.

[2] Hao, Quanrui, et al. "Reduced-order small-signal models of modular multilevel converter and MMC-based HVDC grid." *IEEE Transactions on Industrial Electronics* 66.3 (2018): 2257-2268.

[3] Jamshidifar, Aliakbar, and Dragan Jovcic. "Small-signal dynamic DQ model of modular multilevel converter for system studies." *IEEE Transactions on Power Delivery* 31.1 (2015): 191-199.

[4] Gao, Fei, et al. "Comparative stability analysis of droop control approaches in voltage-source-converter-based DC microgrids." *IEEE Transactions on Power Electronics* 32.3 (2016): 2395-2415.

[5] Pan, Yanfei, et al. "Stability region of droop-controlled distributed generation in autonomous microgrids." *IEEE Transactions on Smart Grid* 10.2 (2018): 2288-2300.

[6] Wang, Rui, et al. "The small-signal stability analysis of the droop-controlled converter in electromagnetic timescale." *IEEE Transactions on Sustainable Energy* 10.3 (2019): 1459-1469.

[7] Guo, Xiaoqiang, et al. "Dynamic phasors-based modeling and stability analysis of droop-controlled inverters for microgrid applications." *IEEE Transactions on Smart Grid* 5.6 (2014): 2980-2987.

[8] Wu, Xiangyu, et al. "Small signal security region of droop coefficients in autonomous microgrids." *2014 IEEE PES General Meeting| Conference & Exposition*. IEEE, 2014.

[9] Tahim, Andre Pires Nobrega, et al. "Modeling and stability analysis of islanded DC microgrids under droop control." *IEEE Transactions on Power Electronics* 30.8 (2014): 4597-4607.

[10] Shuai, Zhikang, et al. "Parameter stability region analysis of islanded microgrid based on bifurcation theory." IEEE Transactions on Smart Grid 10.6 (2019): 6580-6591.

[11] Beerten, Jef, Salvatore D'Arco, and Jon Are Suul. "Identification and small-signal analysis of interaction modes in VSC MTDC systems." *IEEE Transactions on Power Delivery* 31.2 (2015): 888-897.

[12] Pogaku, Nagaraju, Milan Prodanovic, and Timothy C. Green. "Modeling, analysis and testing of autonomous operation of an inverter-based microgrid." *IEEE Transactions on Power Electronics* 22.2 (2007): 613-625.

[13] Freytes, Julian, et al. "Dynamic analysis of MMC-based MTDC grids: use of MMC energy to improve voltage behavior." *IEEE transactions on Power Delivery* 34.1 (2018): 137-148.

[14] Li, Yunfeng, et al. "Modeling and damping control of modular multilevel converter based DC grid." *IEEE Transactions on Power Systems* 33.1 (2017): 723-735.

[15] Li, Zhiyi, and Mohammad Shahidehpour. "Small-signal modeling and stability analysis of hybrid AC/DC microgrids." *IEEE Transactions on Smart Grid* 10.2 (2017): 2080-2095.

[16] Saad, Hani, et al. "Modular multilevel converter models for electromagnetic transients." *IEEE Transactions on Power Delivery* 29.3 (2013): 1481-1489.

[17] Ilves, Kalle, et al. "Steady-state analysis of interaction between harmonic components of arm and line quantities of modular multilevel converters." *IEEE transactions on power electronics* 27.1 (2011): 57-68.

[18] Blaabjerg, Frede, et al. "Overview of control and grid synchronization for distributed power generation systems." *IEEE Transactions on Industrial Electronics* 53.5 (2006): 1398-1409.
[19] Ma, Junchao, et al. "Transmission loss optimization-based optimal power flow strategy by hierarchical control for DC microgrids." *IEEE Transactions on Power Electronics* 32.3 (2016): 1952-1963.
[20] Strang, Gilbert. "*Linear algebra and its applications*." Thmson, Brooks/Cole, Belmont, CA, 2006.

Part III

MATLAB/Simulink-Based Electromagnetic Transient-Transient Stability Hybrid Simulation

Jiangchao Qin
Denise Athaide, Graduate Student
Yuntao Zou, Graduate Student

Arizona State University

For information about this project, contact:

Jiangchao Qin
Arizona State University
School of Electrical, Computer, and Energy Engineering
PO Box 875706
Temp, AZ 85287-5706
Fax: 480-727-2052
Email: jqin@asu.edu

Power Systems Engineering Research Center

The Power Systems Engineering Research Center (PSERC) is a multi-university Center conducting research on challenges facing the electric power industry and educating the next generation of power engineers. More information about PSERC can be found at the Center's website: http://www.pserc.org.

For additional information, contact:

Power Systems Engineering Research Center
Arizona State University
527 Engineering Research Center
Tempe, Arizona 85287-5706
Phone: 480-965-1643
Fax: 480-727-2052

Notice Concerning Copyright Material

Table of Contents

List of Figures

List of Tables

1. Introduction

1.1 Background

Power electronic converters are required for DC/AC conversion, step-up or step-down of voltages and power conditioning. As more and more power converters are being integrated with the grid for HVDC, FACTS, renewable energy integrations, and electric drives, the structure and behavior of power systems is changing, with a high fraction of the generation as well as loads being interfaced through power converters.

Such power electronic equipment is best modeled using electromagnetic transient (EMT) simulation to represent the converters in full details, including the precise, fast switching operations and non-linear nature. However, in these EMT programs, the simulation time step size is usually very small and the presence of frequencies other than the fundamental frequency, such as harmonics and switching frequencies, necessitate the use of instantaneous, three phase quantities. Therefore, they require large computation times. On the other hand, transient stability (TS) simulation programs generally use comparatively large integration time steps. It can be assumed that the fundamental power frequency is maintained throughout the system under most conditions and phasors of the electrical quantities are therefore sufficient to model these systems. They have a much smaller computation time, but are not adequate to represent the dynamic response under transient conditions [1], [2].

In hybrid simulation, only certain parts of the network, which require detailed studies, are simulated in the EMT domain and the rest of the system is simulated in the phasor domain. The system is split into two subsystem models that interact with each other through an interface. This enables detailed, accurate modeling, along with fast, efficient simulation [1]–[4].

1.2 Overview of the Simulation Techniques

In power system studies, depending on the type of study to be conducted, a suitable simulation tool/scheme must be selected.

1.2.1 Electromagnetic Transient (EMT) Simulation

Electromagnetic transients represent the responses of the power system to perturbations or fast dynamic events such as switching, lightning, loading, etc. The analysis of these phenomena requires detailed modeling, which is realized by EMT simulation tools. The system is represented by a set of differential equations and the step size is usually very small, in the range of microseconds. The presence of frequencies other than the fundamental frequency, such as harmonics and switching frequencies, necessitate the use of instantaneous, three phase quantities. Some examples of EMT tools include PSCAD-EMTDC, EMTP-RV, eMEGAsim of Opal-RT, etc.

EMT simulators, however, prove to be unsuitable for the simulation of large networks of account of the relatively small time steps used. This would be time consuming and highly computationally intensive, requiring large processing power. Due to their low simulation speed but high accuracy, EMT-domain simulation tools are used to simulate only small sections of networks that require detailed simulation [2], [4].

1.2.2 Transient Stability (TS) Simulation

Electromechanical Transient simulation and transient stability studies focus on analyzing the ability of the power system to remain in synchronism and maintain voltage and frequency, following a small or large disturbance and analyze the dynamic behavior of the system. As transient stability simulation captures slow dynamics, these studies are carried out during the planning, operation, control and analysis of power systems.

In transient stability analysis, the power system under consideration is represented by nonlinear algebraic equations. In power networks, this usually involves solving a large number of equations. It can be assumed that the fundamental power frequency of 50Hz or 60Hz is maintained throughout the system under most conditions. Phasors of the electrical quantities are therefore sufficient to model these systems. Transient stability simulators generally use comparatively large integration time steps, in the range of milliseconds, to run efficiently.

Some examples of TS tools include OpenDSS, PSS/e, PSLF, PowerWorld, ePHA-SORsim of Opal-RT, ETAP, etc. On account of their speed, Phasor-domain simulation tools are used to simulate large-scale networks. On the other hand, the large time steps used in TS programs prevent them from representing non-linear elements such as power electronic converters, FACTS devices and HVDC equipment, insulation coordination as well as fast dynamics in detail in the power system [2], [4].

1.2.3 Hybrid Simulation

In hybrid simulation, only certain parts of the network, which require detailed studies, are simulated in the EMT domain and the rest of the system in the phasor domain. The system is split into two subsystem models, at the interface bus, with different simulation engines and solution methods. The EMT tool solves the time-domain differential equations with a very small time step and the phasor tool solves the power flow equations with a larger time step, at the fundamental frequency [2]. The two simulation models interact with each other through an interface. Hybrid simulation is very beneficial in analyzing large systems with penetration of converter interfaced generation and loads, as these systems require both accurate as well as fast simulation. It thus enables the study of large systems, while providing detailed dynamic information about them, which is impossible to achieve with either EMT or TS simulation tools alone. Hybrid simulation however poses a number of challenges, which are explored in detail in this work. A comparison of simulation methods between EMT and TS is shown in Tab. Table 1.1.

Table 1.1 Comparison between EMT and TS simulation methods

Point of Comparison	Comparison of Simulation Methods	
	Electromagnet Transient (EMT) Simulation	**Transient Stability (TS) or Phasor Simulation**
Modeling Requirements	Instantaneous waveforms, three-sequence, three-phase analysis, all frequencies.	Phasors, positive sequence single-phase analysis, fundamental frequency
Time Step	Few microseconds	Few milliseconds
Accuracy	High, captures fast transients	Lower, captures slow dynamics
Speed	Slow	Fast
Efficiency	Lower	Higher
Computational Power	Computational exhaustive	Lower computational power required
System Size	Small	Large

A number of progressive hybrid simulation techniques have been proposed in literature up to date. The concept of Hybrid Simulation was first introduced in references [5], [6] and [7], for the purpose of High Voltage Direct Current (HVDC) converter studies in 1981. References [8], [9] and [10] focus on progressively incorporating EMT models of nonlinear elements such as flexible AC transmission (FACTS) and HVDC systems into traditional TS simulation programs. They integrate a static VAR compensator (SVC), modeled at the device level, concentrating on interaction protocol and other interface requirements to be taken into consideration. Reference [11] classifies and addresses the main requirements and challenges faced in interfacing EMT and TS simulators for hybrid simulation. It also proposes an integrated EMT-TS simulation using frequency adaptive modeling and simulation, including frequency shifting and companion models. Reference [3] puts forward a relaxation approach applied to time interpolation and phasor extraction. It also summarizes the main equivalent models or boundary conditions used in hybrid simulation literature. In reference [1], an open-source hybrid simulation tool, OpenHybridSim, is developed. It uses InterPSS for TS simulation and can be integrated with various EMT simulators, with a socket communication based interface. Reference [12] employs this tool for fault-induced delayed voltage recovery (FIDVR) studies, using PSCAD/EMTDC and InterPSS. A combined interaction protocol with automatic switching as well as multi-port three-phase Thevenin equivalent was also introduced in the tool.

References [2] introduce an open-source hybrid simulation tool, using the OpenDSS TS simulator and a Matlab-scripted EMT simulator interfaced with a component object model (COM) server. It is designed to perform solar PV impact studies in distribution systems. Reference [13] demonstrates the tools ability to perform islanding detection studies in such distribution networks. Reference [14] extends this tool to use Python-scripted EMT simulation instead of Matlab scripts. Reference [15] proposes a distributed hybrid simulation method, with a combined interaction protocol and a two-level Schur complement interfacing technique. In reference [16], a dynamic phasor-based interface model (DPIM) has been developed, to study the interactions between HVDC systems and the AC grid. In reference [17], an EMT modular multilevel converter (MMC) based HVDC system in in PSCAD/EMTDC is combined with the AC grid programmed in C language as a user-defined model in PSCAD. An implicitly-coupled solution method is presented in reference [18], where the EMT and TS equations are combined and solved simultaneously. Reference [19] focuses on the application of hybrid simulation to VSC-HVDC systems and techniques to improve accuracy. The above mentioned hybrid simulation implementations use EMT and TS off-line Software. OPAL-RT's real-time simulation tools primarily include ePHASORsim, HYPERSIM, eMEGAsim and eFPGAsim, suitable for simulation time-steps ranging from milliseconds to nanoseconds and large to small model sizes respectively [20]. The RT-LAB suits simulation environment has the potential to run two types of simulations, namely the TS simulator ePHASORsim and the EMT simulator eMEGAsim, in one working model, thus enabling hybrid simulation [21, 22]. Reference [23] explores parallelization techniques for real-time simulation and the suitability of hybrid simulation, using the OPAL-RT real time digital simulator, for islanding detection and explores parallelization techniques for real-time simulation and the suitability of hybrid simulation, using the OPAL-RT real time digital simulator, for islanding detection. Reference [24] explains this capability and the interfacing method in detail.

1.3 Report Organization

This project puts forth a Hybrid EMT-TS simulation method in MATLAB/Simulink for modeling and simulating power electronic based power systems, e.g., PV/Wind integrated systems, AC-HVDC interconnected systems, etc. The proposed method enables the study of large systems, while providing detailed dynamic information, which is impossible to achieve with either EMT or TS simulation tools alone.

This report is structured as follows. Chapter 2 investigates TS and EMT modeling and simulation in MATLAB/Simulink, respectively. In Charter 3, an interface between TS and EMT simulation is developed. Chapter 4 presents the study results and Chapter 5 concludes the report.

2. Modeling and Simulation of the Study System

The purpose of selecting MATLAB/Simulink over individual software for EMT and TS simulation is to deliver a more general simulation environment, to test the hybrid simulation algorithm and procedure, particularly the interface between the EMT and TS simulations. It also ensures improved and less complex interfacing, communication and compatibility between the EMT and TS simulation models. The flow chart for running the proposed hybrid simulation method is shown in Fig. Figure 2.1.

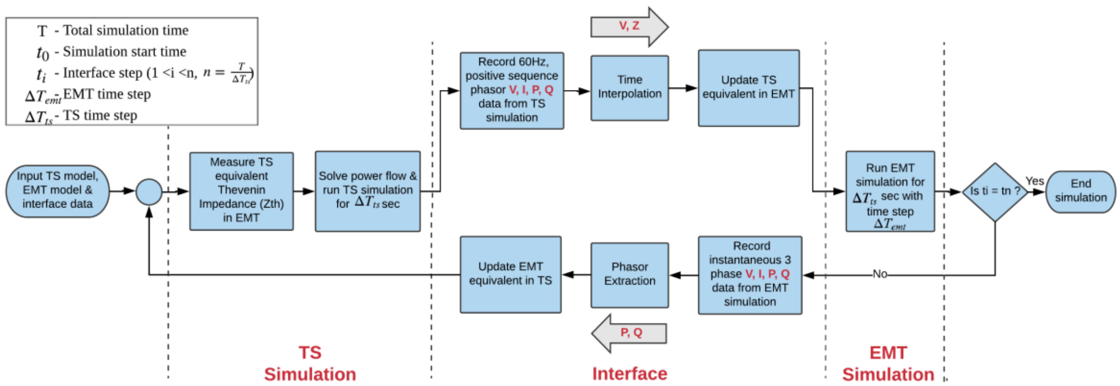

Figure 2.1 The proposed equivalent circuit of an arm.

2.1 Transient Stability Modeling and Simulation

The network being considered in this work is the Western System Coordinating Council (WSCC) IEEE 9-bus test system, also known as P.M Anderson 9-bus [25]. It represents a simple approximation of the WSCC to an equivalent system with nine buses, three generators and three loads [26]. In this study, the WSCC 9-bus system has been modified to replace the synchronous generator at bus 3 by a solar photovoltaic (PV) plant.

The real merits of hybrid simulation are prominent in much larger systems. However, in order to develop the hybrid simulation framework in MATLAB/Simulink and enable feasible validation, a 9-bus system has been employed in this work. Simulink has been used to run the power flow solution and dynamic simulation of the network in the Phasor domain. The implementation of this modified 9-bus system in the TS domain in Simulink is depicted in Fig. Figure 2.2 [27], [28]. The associated single-line diagram of the WSCC IEEE 9-Bus system is shown in Fig. Figure 2.3 .There are nine Load Flow Bus blocks in the model, defining the bus locations, parameters to solve the load flow and base voltages at their respective buses. The Load Flow tool of the Powergui is used to compute the voltage, real power flow and reactive power flow at each bus using the Newton-Raphson method and initialize the network. In this case, positive-sequence load flow is applied to the three-phase system [27]. A step size of 10 ms has been used in the TS simulation.

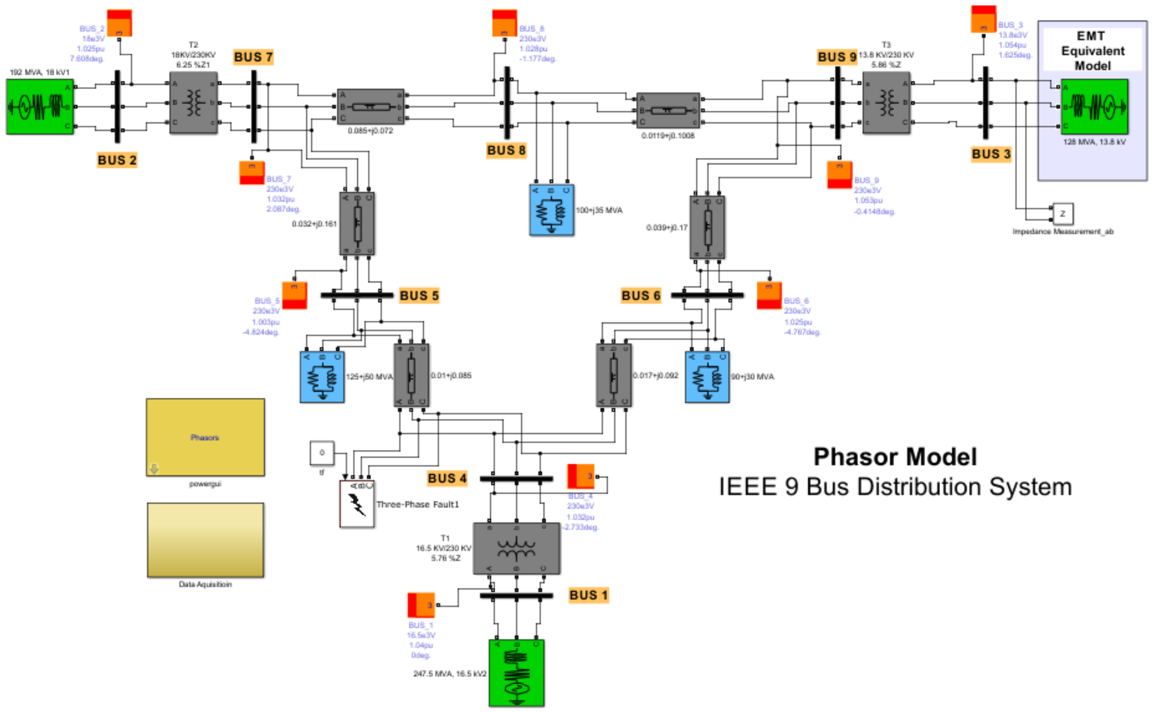

Figure 2.2 Transient stability simulation block diagram in MATLAB/Simulink.

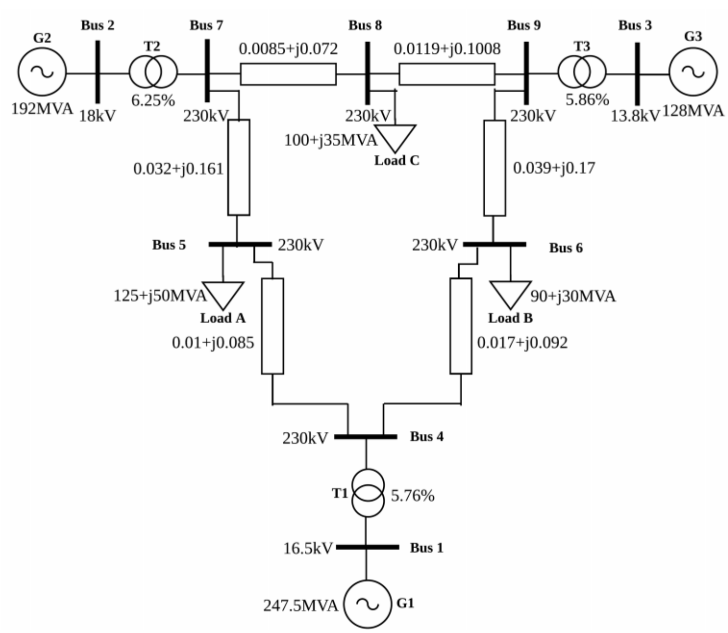

Figure 2.3 Single-line diagram of the WSCC IEEE 9-Bus system.

2.2 Electromagnetic Transient Modeling and Simulation

The grid-tied 85 MW Solar Photovoltaic (PV) Plant at Bus 3 of the 9-bus network is modeled in Simulink for the EMT simulation. Figure Figure 2.4 depicts the three-phase circuit diagram of this system. It consists of a PV array, a three-phase pulse width modulated (PWM) voltage source inverter, a current controller, an AC inductive filter and the Thevenin equivalent model of the TS simulation. A step size of 5 μs have been used. The Solar PV array is modeled using the five-parameter model. A 300kW Jakson solar PV module “JP300W24V” has been selected for this case study. The PV cell V-I characteristics and datasheet parameters are used to determine the parameters for that cell’s model at the Standard Test Conditions (STC).

The voltage source inverter is modeled with a detailed switching model. The switching of the inverter is controlled by PWM gate pulses, generated by a Type 2 current controller. Sinusoidal Pulse Width Modulation (SPWM) has been used, with a 20 kHz carrier frequency. In this case, the output AC current is controlled. In order to simplify the control scheme, the dq frame of reference is used. Large solar power plants, such as the one modeled at Bus 3, typically utilize a number of MW-scale inverters. There could be individual string inverters assigned to separate strings of solar panels or one central inverter assigned to the entire array of panels. An inductive (L) filter is designed to filter out the high switching frequency component in the AC current and limit the total harmonic distortion in the AC current to 5%. A Thevenin equivalent circuit represents the TS model in the EMT domain.

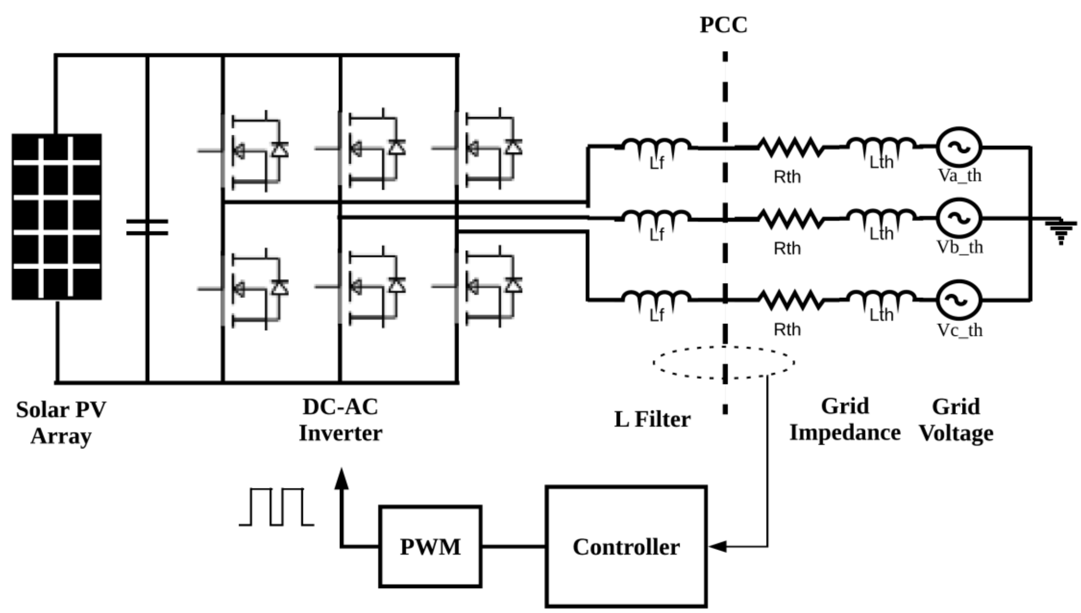

Figure 2.4 Electromagnetic transient simulation block diagram in MATLAB/Simulink.

3. The Interface Between TS and EMT Simulation

A critical component of hybrid simulation is the interaction between the EMT and TS simulators, which requires a well-designed interface algorithm. The structure of the interface designed in this research has been depicted in Fig. Figure 3.1.

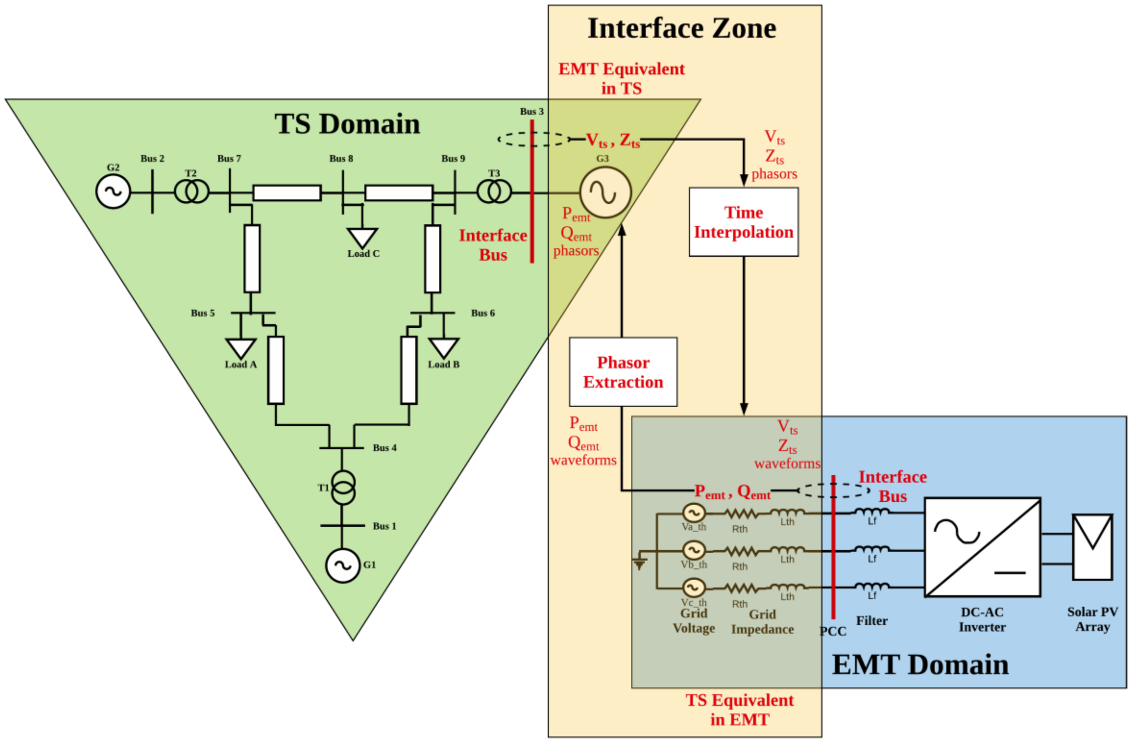

Figure 3.1 EMT-TS hybrid simulation interface in MATLAB/Simulink.

3.1 Electromagnetic Transient Modeling and Simulation

In the first step of the hybrid simulation, the network is partitioned into the detailed EMT system and the external TS system at the interface bus, based on which part of the system requires a detailed study [2], [4]. Expanding the detailed system increases the accuracy, but also increases the complexity and decreases the efficiency.

Usually, in grid-connected renewable energy systems, the distributed generation system is the portion requiring EMT simulation, therefore the point of common coupling (PCC), where the distributed generator connects to the grid, is chosen as the interface bus. In the study system, bus 3 is selected as the interface bus, as it separates the network and PV system, which has been modeled in detail.

3.2 Equivalent Models and Selection of Exchanged Data

Since the EMT and TS simulation models are solved independently, each must contain an equivalent representation of the other in its own model, which is updated dynamically at each interface step during the hybrid simulation [1], [16]. The phasor system is represented in the EMT simulation model as a Thevenin voltage source in series with a Thevenin impedance [2], [3], [18]. The equivalent Bus 3 voltage magnitude and phase angle is obtained from the phasor simulation results and fed into three AC Voltage Source blocks in Simulink. The Impedance Measurement block measures the equivalent network impedance, as seen from Bus 3 in the phasor simulation model, as a function of frequency [5]. It is only altered during the simulation if there are network configuration changes.

In this case, the EMT system is represented in the phasor simulation model as a Three-Phase Voltage Source, specifically a PQ type generator injecting active power and reactive power [2], [3], [5]. The specified real and reactive power generation is obtained from the results of the EMT simulation.

3.3 Data Extraction

The TS equivalent model requires the instantaneous voltage at the interface bus whereas the EMT equivalent model requires the phasors of the injected real and reactive powers. Therefore, before data is exchanged between the simulation models, it must be transformed into the appropriate form.

In order to convert the instantaneous three-phase waveforms of the quantities from the EMT simulation into phasor quantities at the fundamental frequency, Phasor Extraction techniques are implemented [3], [4], [19]. In this work, at every TS time step, the RMS values of the real and reactive powers for that given time period are calculated using the dq currents and voltages and sent to the TS simulation. In order to implement Fourier Transform, on the other hand, the TS time step should be of the length of the fundamental time period window or more, which imposes a restriction on the minimum interface time step.

To obtain instantaneous waveforms for the EMT simulation from phasor values of the TS simulation parameters, Time Interpolation is implemented [2], [3]. Here, time interpolation using an AC voltage source controlled by peak amplitude, phase and frequency has been used in Simulink, to perform the phasor-to-waveform conversion. The magnitude and phase angle for each phase is updated at every interaction time step.

3.4 Interaction Protocol

The interaction protocol of the hybrid simulation determines the order of data exchange at the EMT-TS interface [2]. The protocols for data transfer between the EMT and TS models may be either serial, parallel or a combination of both. The serial protocol ensures better accuracy, whereas the parallel protocol improves efficiency [1]. The process in this work, when a serial protocol is used, is illustrated in Fig. Figure 3.2. The four main interaction protocol steps are stated below:

1) At t_0, transform the active and reactive power instantaneous waveforms, from the previous interface step EMT simulation result, to phasors. Transfer these phasors from the EMT domain to the TS simulation model.

2) Solve the power flow and execute the TS simulation with a time step of ΔT_{ts} until t_1 is reached.

3) Transform the current and voltage phasors to instantaneous waveforms. Transfer these quantities from the TS domain to the EMT simulation model.

4) Execute the EMT simulation from t_0 to t_1 with a time step of ΔT_{emt}.

This process is repeated until the total simulation time T is reached.

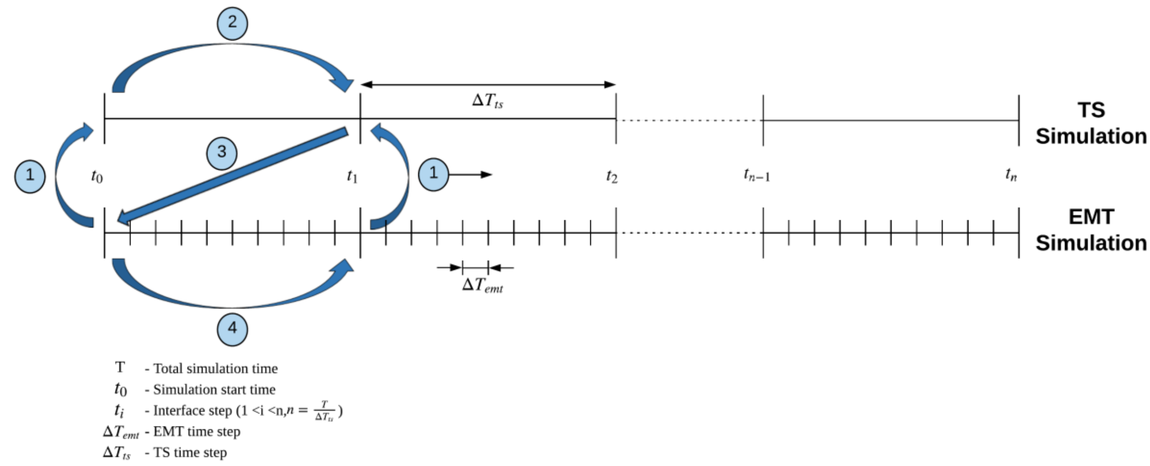

Figure 3.2 Serial interaction protocol.

3.5 Communication and Plotting

Interaction and data transfer between the two simulation models is facilitated by the MATLAB Workspace. The EMT and TS simulations are each modeled in the EMT and phasor domains, respectively, in separate Simulink files and the interface algorithm is implemented through MATLAB code. The exchanged parameter values are dynamically updated and accessible to the interacting models, in the Workspace, at every interaction time step throughout the simulation.

In order to plot continuous waveforms of the quantities, such as current, voltage and power, at the completion of the hybrid simulation, it is essential to stitch the quantities measured during each interaction step. This is executed in MATLAB by creating vectors of the required signals at the end of each interaction time step and feeding them to a larger, encompassing vector, which is plotted at the end of the entire simulation. This process is illustrated in Fig. Figure 3.3.

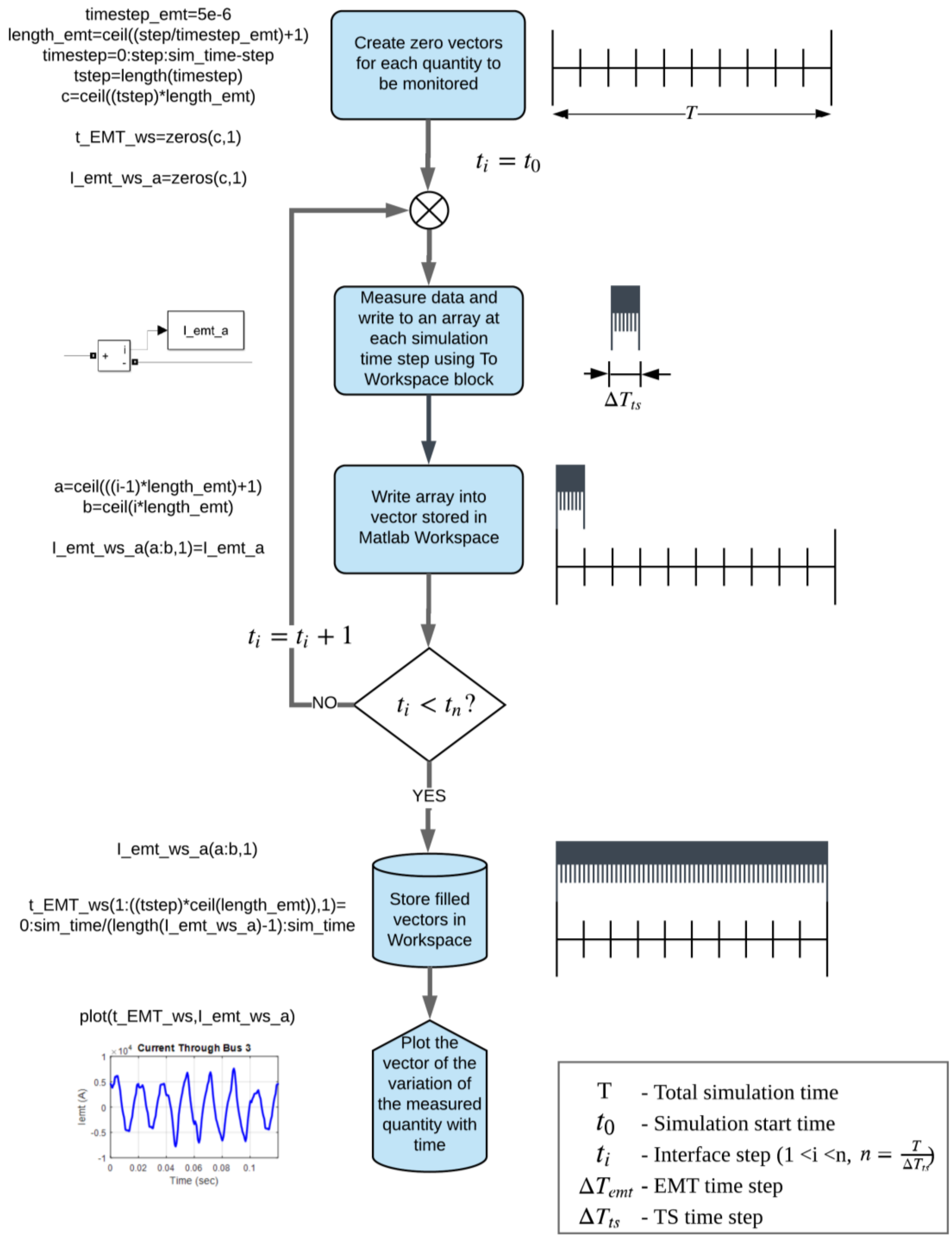

Figure 3.3 Procedure for plotting.

4. Testing and Validation

In this section, the hybrid simulation method described in the previous chapters is tested and validated. The system under consideration is the WSCC IEEE 9 bus network, modified to replace the synchronous generator at bus 3 by a solar PV plant. Steady-state analysis and transient analysis case studies have been performed. The transients include a Single-Phase Line-To-Grounding (SLG) Fault and Variation in Solar PV Power Output, which represent transients in the TS and EMT domains respectively. The results have been compared with the benchmark full EMT simulation model of the network.

4.1 Steady-State Analysis

Figures Figure 4.1 and Figure 4.2 show the instantaneous phase-a voltage and current at the PCC during steady-state. The errors in the magnitude and phase of these quantities are negligible. Table Table 4.1 compares the RMS values of the boundary currents and voltages during steady-state. It can be seen that the maximum error between the PCC quantities in the EMT and TS subsystems is only around 0.53%, closely matching boundary currents and voltages, which signifies that the model is running fairly accurately. Figure Figure 4.3 indicates the runtime of the full EMT and hybrid simulation models for 0.3-second operation. It is evident that the hybrid simulation method drastically reduces the simulation runtime, by almost 82%, yet maintaining a suitable level of accuracy.

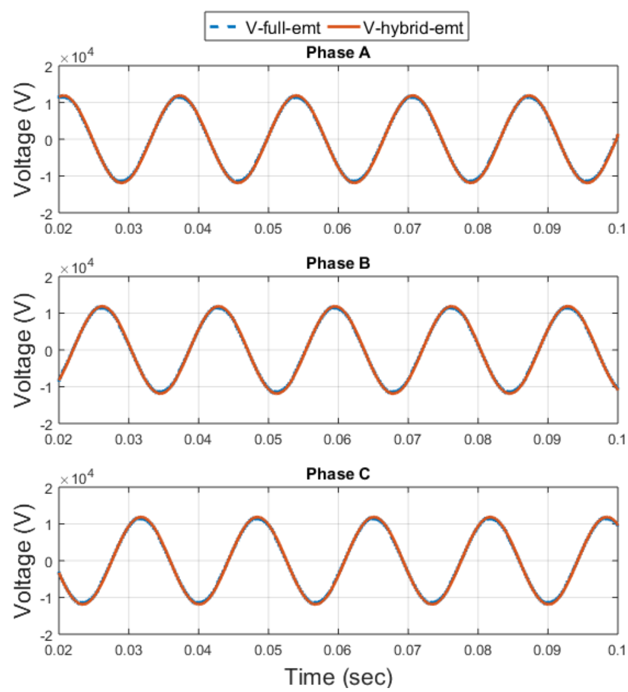

Figure 4.1 The instantaneous voltage wave at Bus 3 of full EMT and hybrid simulation.

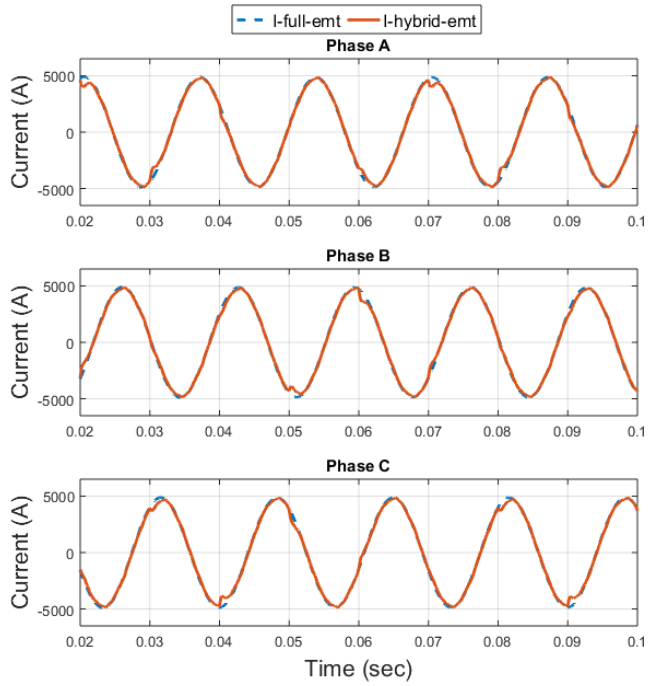

Figure 4.2 The instantaneous current wave at Bus 3 of full EMT and hybrid simulation.

Table 4.1 Error Evaluation Between Steady-State Bus 3 RMS Currents and Voltages in Hybrid Simulation EMT and TS Subsystems

Parameters	Phase	Value		Error (%)
		Hybrid EMT	Hybrid TS	
Current (A)	A	3408.25	3390.08	0.5332
	B	3404.01	3390.08	0.4902
	C	3401.18	3390.08	0.3264
Voltage (V)	A	8392.86	8392.79	0.0008
	B	8400.71	8400.36	0.0042
	C	8400.75	8400.99	0.0029

4.2 Transient Analysis

4.2.1 Single-Phase Line-To-Ground Fault

This case represents a transient in the Phasor domain. At the instant of 0.1 s, a single phase line-to-ground (SLG) fault between phase a and ground is applied at bus 4 and cleared after 0.1 s (6 cycles), with the original network configuration restored. Figures Figure 4.4 and Figure 4.5 show that the instantaneous voltages and currents at the PCC during the fault. The active power is provided in Fig. Figure 4.6.

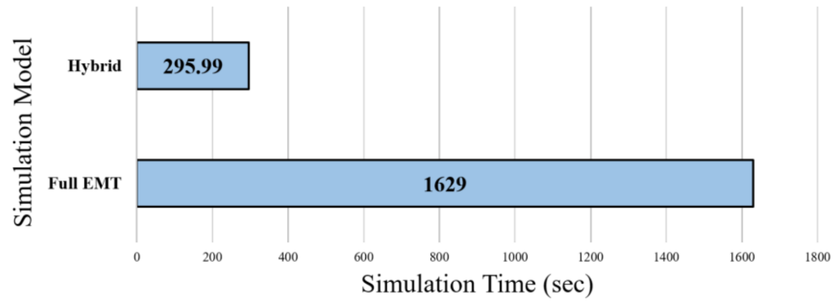

Figure 4.3 The comparison of simulation speed.

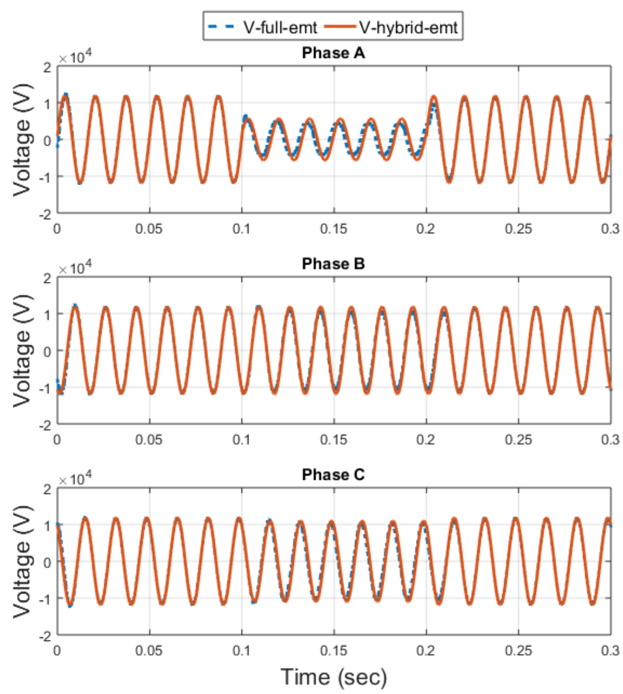

Figure 4.4 The instantaneous voltage at Bus 3 (interface bus) during a SLG fault at Bus 4.

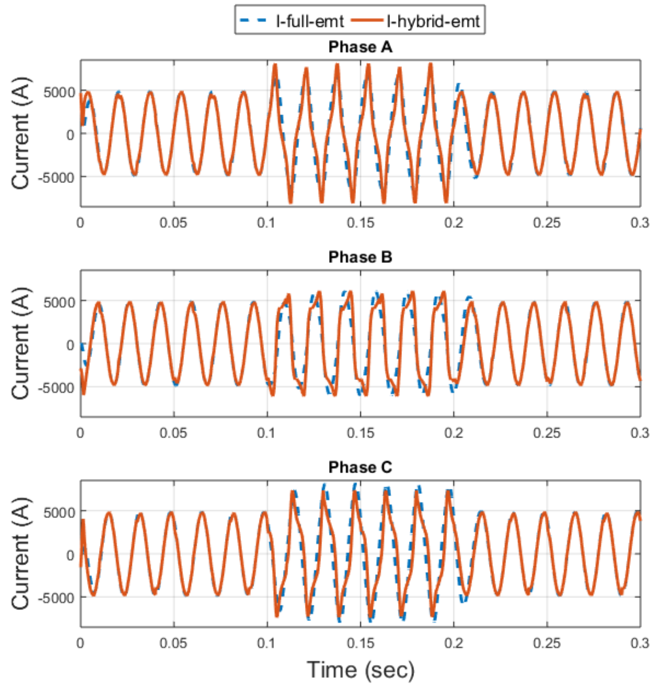

Figure 4.5 The instantaneous current at Bus 3 (interface bus) during a SLG fault at Bus 4.

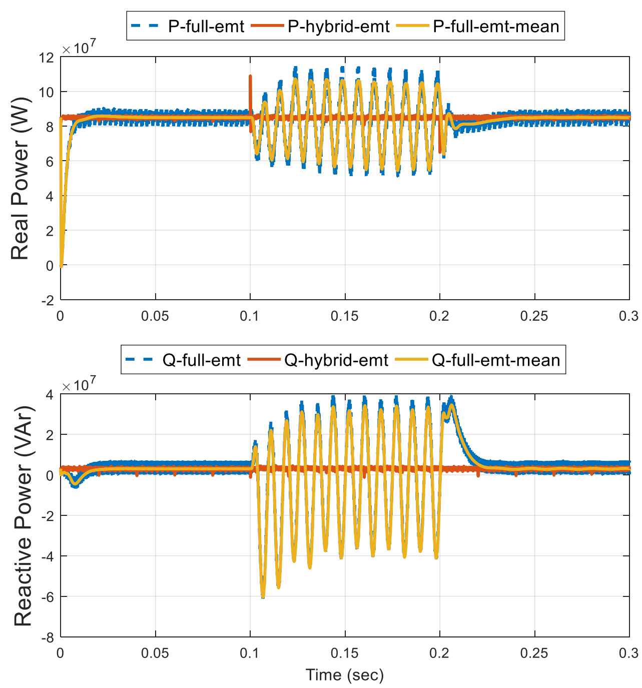

Figure 4.6 The active power at Bus 3 (interface bus) during a SLG fault at Bus 4.

There is a good match between the hybrid simulation and full EMT simulation results before and after the fault and a negligible error in phase shift and magnitude during the fault. The minor errors observed during the transient can be attributed to loss of some information and approximations at the interface. For instance, all the harmonics injected by the inverter in the EMT simulation are not represented in the TS simulation, as the latter only considers the fundamental frequency components of voltage and current.

Also, inadequacies in data extraction, equivalent models and data exchanged can contribute towards errors or deviation from the true results as obtained from the full EMT simulation.

4.2.2 Variation in Solar Irradiance

This case represents a transient in the EMT domain. The solar irradiance drops from1000 W/m2 (STC) to 800 W/m2 at 0.1 s. This causes a decrease in current and hence in real power output from the solar PV plant, from 85 MW to 68 MW, as seen in Fig. Figure 4.7.

Figures Figure 4.8 and Figure 4.9 show that the instantaneous voltages and currents at the PCC during the fluctuation in solar irradiance. There is a good agreement between the results from the hybrid simulation and those from the benchmark full EMT simulation.

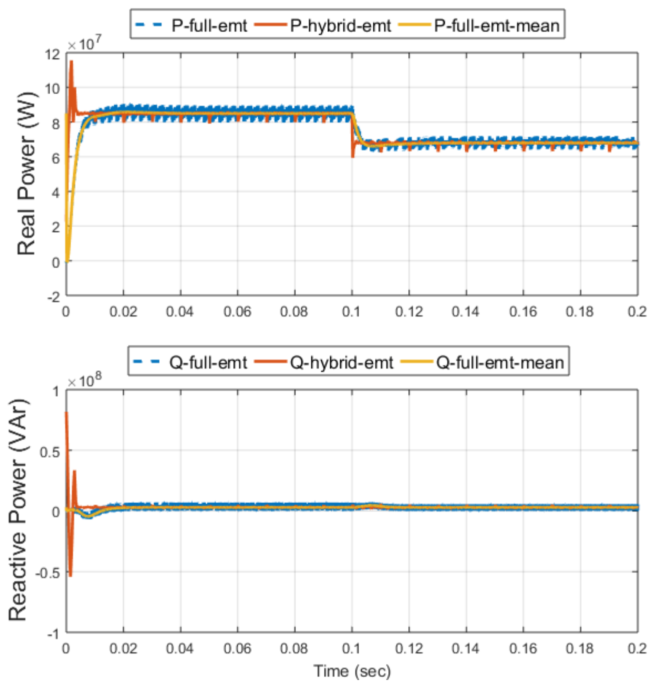

Figure 4.7 The active power at Bus 3 (interface bus) during a decrease in solar irradiance.

4.2.3 Interface Time Step Analysis

The interface time step has been varied from 10 ms to 50 ms, for the SLG fault transient case. In Fig. Figure 4.10, it can be seen that the runtime decreases as the time step increases. However, the accuracy of the results is affected. This can be noticed in Figs. Figure 4.11 and Figure 4.12, which depict the phasors of the phase-a voltage and current at the PCC during the SLG fault case, for a range of interface time steps. Meanwhile, the instantaneous voltage and current of phase a at PCC during SLG fault case are also informed in Figs. Figure 4.13 and Figure 4.14.

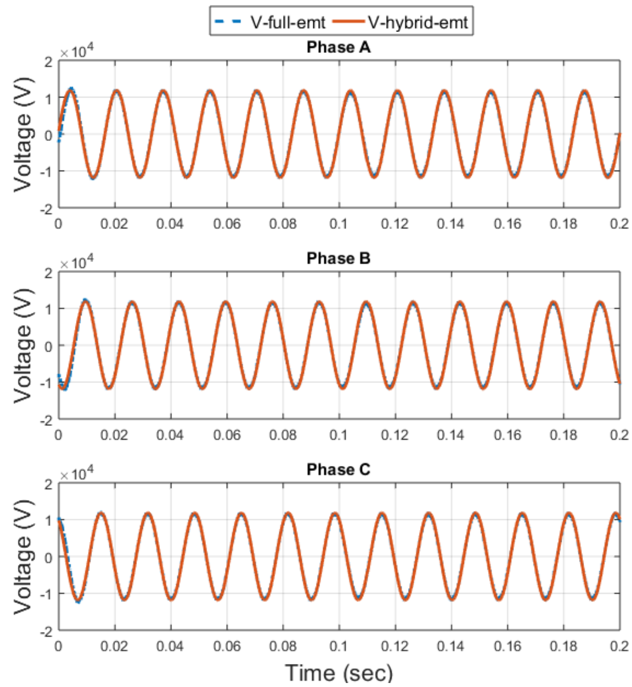

Figure 4.8 The instantaneous voltage at Bus 3 (interface bus) during a decrease in solar irradiance.

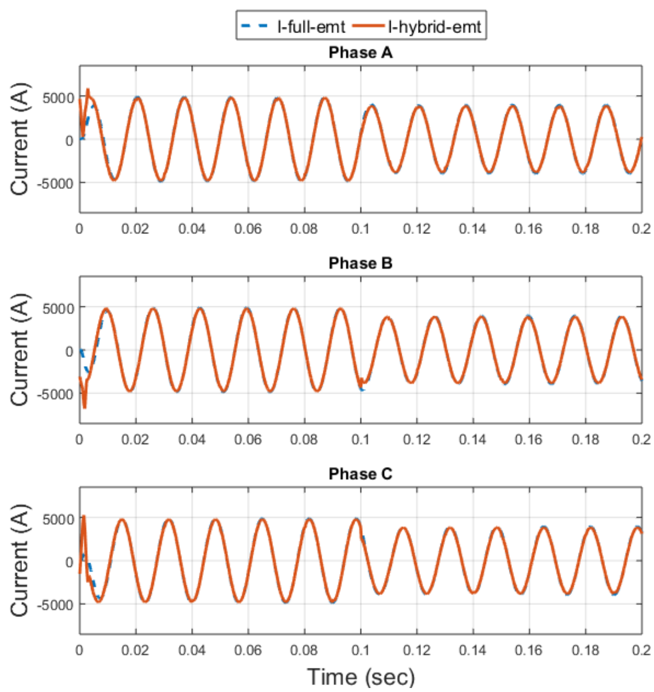

Figure 4.9 The instantaneous current at Bus 3 (interface bus) during a decrease in solar irradiance.

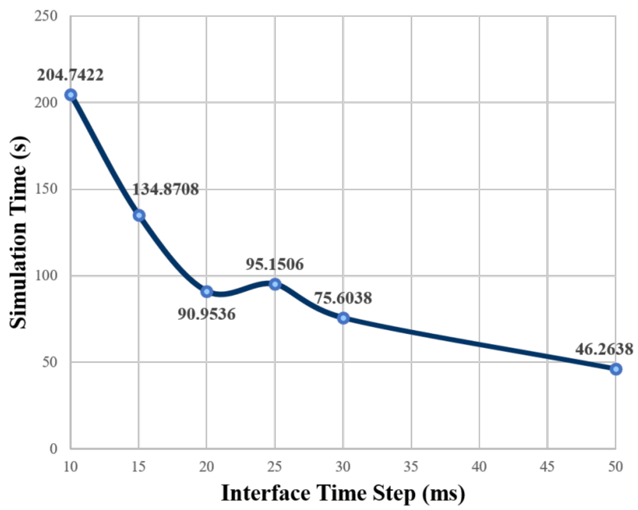

Figure 4.10 The effect of interface time step variation on simulation runtime.

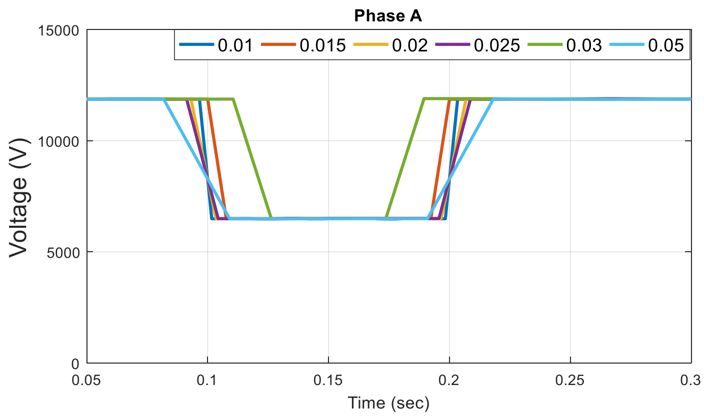

Figure 4.11 The phasor phase A voltage at Bus 3 (interface bus) during a SLG fault at Bus 4 for a range of interface time steps.

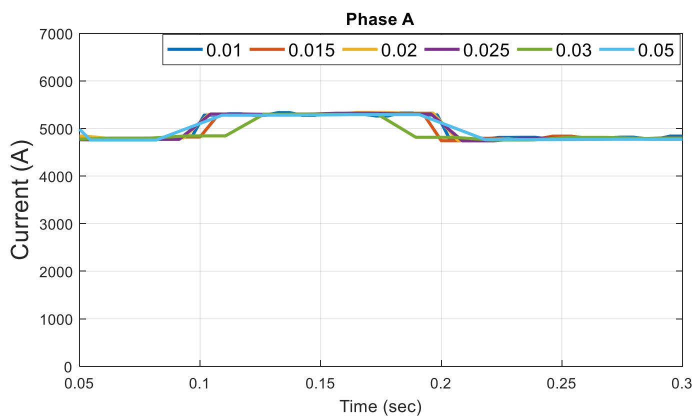

Figure 4.12 The phasor phase A current at Bus 3 (interface bus) during a SLG fault at Bus 4 for a range of interface time steps.

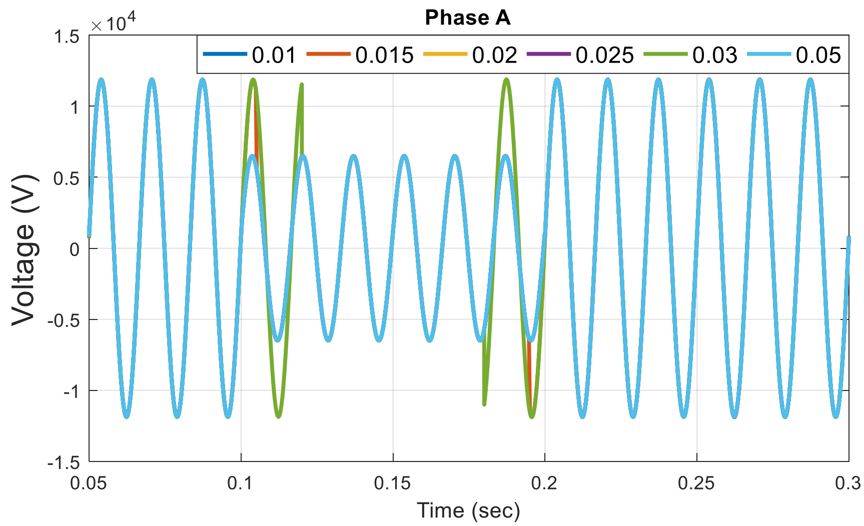

Figure 4.13 The phasor phase A current at Bus 3 (interface bus) during a SLG fault at Bus 4 for a range of interface time steps.

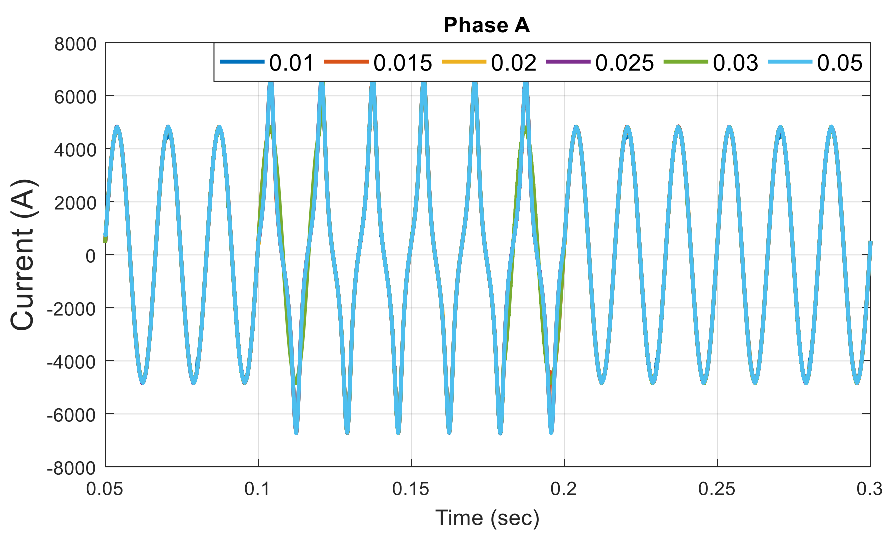

Figure 4.14 The instantaneous phase A current at Bus 3 (interface bus) during a SLG fault at Bus 4 for a range of interface time steps.

Furthermore, an error comparison is also informed in Tab. Table 4.2. This table summarizes the performance of the proposed hybrid simulation during steady-state and SLG fault. It is evident that the proposed hybrid simulation has a high precision on both voltage and current at interface Bus 3 during steady state. EMT and TS simulation section converge to the real value of system operation. In the other side, during SLG fault, the precision of voltage at interface Bus 3 keeps high percentage but the current of it loses lots of precision, since TS simulation in Phasor method only takes account of fundamental frequency of ac system.

Table 4.2 Error evaluation summarized steady-state and SLG fault at Bus 3 RMS currents and voltages in hybrid simulation EMT and TS subsystems

Case	Parameters	Phase	Value		Error (%)
			Hybrid EMT	Hybrid TS	
Steady State	Current (A)	A	3408.25	3390.08	0.5332
		B	3404.01	3390.08	0.4092
		C	3401.18	3390.08	0.3264
	Voltage (V)	A	8392.86	8392.79	0.0008
		B	8400.71	8400.36	0.0042
		C	8400.75	8400.99	0.0029
SLG Fault	Current (A)	A	4723.47	3766.05	20.2695
		B	3577.96	2350.07	50.2470
		C	3992.32	3144.90	21.2264
	Voltage (V)	A	4598.72	4598.73	0.0002
		B	10702.70	10702.68	0.0001
		C	14166.96	14167.07	0.0008

5. Conclusions

In this work, an electromagnetic transient and transient stability hybrid simulation method has been developed in MATLAB. This approach combines high accuracy of EMT simulation and fast speed of TS simulation with only one software platform and a simple interface algorithm between EMT and TS simulation. It provides a useful tool for the study of power networks with penetration of power electronic converter interfaced generation and loads. The proposed hybrid simulation scheme has been tested on the WSCC IEEE 9-bus system. The system behaviors during steady state and under faults and solar irradiance variation have been studied. Most importantly, the user experience is significantly improved due to the implementation in MATLAB with the flexibility, accessibility, user-friendliness and ease of access.

References

[1] Huang, Qiuhua, and Vijay Vittal. "OpenHybridSim: An open source tool for EMT and phasor domain hybrid simulation." 2016 IEEE Power and Energy Society General Meeting (PESGM). IEEE, 2016.

[2] Hariri, Ali, and Md Omar Faruque. "A hybrid simulation tool for the study of PV integration impacts on distribution networks." IEEE Transactions on Sustainable Energy 8.2 (2016): 648-657.

[3] Plumier, Frédéric, et al. "Co-simulation of electromagnetic transients and phasor models: A relaxation approach." IEEE Transactions on Power Delivery 31.5 (2016): 2360-2369.

[4] Jalili-Marandi, V., et al. "Interfacing techniques for transient stability and electromagnetic transient programs IEEE task force on interfacing techniques for simulation tools." IEEE Transactions on Power Delivery 24.4 (2009): 2385-2395.

[5] Heffernan, M. D., et al. "Computation of ac-dc System Disturbances. Part I. Interactive coordination of generator and convertor transient models." IEEE transactions on Power Apparatus and Systems 11 (1981): 4341-4348.

[6] K. S. Turner, et al. "Computation of ac-dc System Disturbances. Part II. Derivation of Power Frequency Variables from Convertor Transient Response," IEEE Transactions on Power Apparatus and Systems 11 (1981):4349-4355.

[7] K. S. Turner, et al. "Computation of ac-dc System Disturbances. Part III. Transient Stability Assessment," IEEE Transactions on Power Apparatus and Systems 11 (1981):4356-4363.

[8] Su, Hongtian, Kevin KW Chan, and Laurence A. Snider. "Interfacing an electromagnetic SVC model into the transient stability simulation." Proceedings. International Conference on Power System Technology. Vol. 3. IEEE, 2002.

[9] Su, Hongtian, et al. "A new approach for integration of two distinct types of numerical simulator." Proceedings of International Conference on Power System Transmission, New Orleans, USA. 2003.

[10] Su, H. T., K. W. Chan, and L. A. Snider. "Parallel interaction protocol for electromagnetic and electromechanical hybrid simulation." IEE Proceedings-Generation, Transmission and Distribution 152.3 (2005): 406-414.

[11] Jalili-Marandi, V., et al. "Interfacing techniques for transient stability and electromagnetic transient programs IEEE task force on interfacing techniques for simulation tools." IEEE Transactions on Power Delivery 24.4 (2009): 2385-2395.

[12] Huang, Qiuhua, and Vijay Vittal. "Application of electromagnetic transient-transient stability hybrid simulation to FIDVR study." IEEE Transactions on Power Systems 31.4 (2015): 2634-2646.

[13] Hariri, Ali, and M. Omar Faruque. "Performing islanding detection in distribution networks with interconnected photovoltaic systems using a hybrid simulation tool." 2016 IEEE Power and Energy Society General Meeting (PESGM). IEEE, 2016.

[14] Hariri, Ali, Alvi Newaz, and Md Omar Faruque. "Open-source python-OpenDSS interface for hybrid simulation of PV impact studies." IET Generation, Transmission & Distribution 11.12 (2017): 3125-3133.

[15] Shu, Dewu, et al. "A novel interfacing technique for distributed hybrid simulations combining EMT and transient stability models." IEEE Transactions on Power Delivery 33.1 (2017): 130-140.

[16] Shu, Dewu, et al. "Dynamic phasor based interface model for EMT and transient stability hybrid simulations." IEEE Transactions on Power Systems 33.4 (2017): 3930-3939.
[17] Meng, Xuekun, and Liwei Wang. "Interfacing an EMT-type modular multilevel converter HVDC model in transient stability simulation." IET Generation, Transmission & Distribution 11.12 (2017): 3002-3008.
[18] Abhyankar, Shrirang, and Alexander J. Flueck. "An implicitly-coupled solution approach for combined electromechanical and electromagnetic transients simulation." 2012 IEEE Power and Energy Society General Meeting. IEEE, 2012.
[19] van der Meer, Arjen A., et al. "Advanced hybrid transient stability and EMT simulation for VSC-HVDC systems." IEEE Transactions on Power Delivery 30.3 (2014): 1057-1066.
[20] OPAL-RT. Accessed October 2018. [Online]. Available: https://www.opalrt. com/
[21] S. Abourida, J. Blanger and V. Jalili-Marandi, Real-Time Power System Simulation: EMT vs. Phasor, White Paper [Online]. Available: https://www.opalrt.com/wp-content/themes/enfold-opal/pdf/L00161 0121.pdf.
[22] OPAL-RTs Solution for Hybrid EMT-TS Simulation. Accessed October 2018. [Online]. Available: http://sites.ieee.org/pes-itst/files/2017/06/2017- Panel-4.pdf.
[23] Panigrahy, Nigamananda, et al. "Real-time phasor-EMT hybrid simulation for modern power distribution grids." 2016 IEEE International Conference on Power Electronics, Drives and Energy Systems (PEDES). IEEE, 2016.
[24] Jalili-Marandi, Vahid, et al. "Real-time electromagnetic and transient stability simulations for active distribution networks." International Conference on Power System Transients (IPST). 2013.
[25] Francisco M. Gonzalez-Longatt, ”Test Case P.M. Anderson Power System,” Power Systems Test Cases.
[26] KIOS Centre for Intelligent Systems & Networks, ”IEEE 9-bus modified test system”, 2013.
[27] MathWorks Documentation. Accessed October 2018. [Online]. Available: https://www.mathworks.com/help/
[28] Jaikumar Pettikkattil, ”IEEE 9 Bus,” Mathworks Simulink File Exchange Center, Mar. 2014.